ANALYSIS OF DIELECTRIC SLAB-COVERED WAVEGUIDE ARRAYS ON LARGE CYLINDERS

Quirino Balzano, et al

Raytheon Company

Prepared for:

Air Force Cambridge Research Laboratories

August 1973

UNCLASSIFIED
Security Classification

DOCUMENT CONTROL DATA - R&D

(Security classification of title, body of abstract and indexing annotation must be entered when the overall report is classified)

1. ORIGINATING ACTIVITY *(Corporate author)*
Raytheon Company
Missile Systems Division
Bedford, Massachusetts 01730

2a. REPORT SECURITY CLASSIFICATION
UNCLASSIFIED

2b. GROUP
ADA-009599

3. REPORT TITLE
ANALYSIS OF DIELECTRIC SLAB-COVERED WAVEGUIDE ARRAYS ON LARGE CYLINDERS

4. DESCRIPTIVE NOTES *(Type of report and inclusive dates)*
Scientific Interim

5. AUTHOR(S) *(First name, middle initial, last name)*
Quirino Balzano
Lawrence R. Lewis
Kazimierz Siwiak

6. REPORT DATE	7a. TOTAL NO. OF PAGES	7b. NO. OF REFS
August 1973	108	31

8a. CONTRACT OR GRANT NO.	9a. ORIGINATOR'S REPORT NUMBER(S)
F19628-72-C-0202	BR-7663
b. PROJECT, TASK, WORK UNIT NOS. 4600-11-01	Scientific Report No. 1
c. DOD ELEMENT 62702F	9b. OTHER REPORT NO(S) *(Any other numbers that may be assigned this report)*
d. DOD SUBELEMENT 674600	AFCRL-TR-73-0587

10. DISTRIBUTION STATEMENT
A - Approved for public release; distribution unlimited.

11. SUPPLEMENTARY NOTES	12. SPONSORING MILITARY ACTIVITY
Tech, Other	Air Force Cambridge Research Laboratories (LZ) LG Hanscom Field Bedford, Massachusetts 01730

13. ABSTRACT

This report presents a method for predicting the coverage obtainable from a small array of waveguide apertures (20 - 30 dB aperture gain) over a large cylinder covered by dielectric (cylinder radius ≈ 100 λ).

An infinite array model is developed, which shows that there are only minor differences between the pattern of an element in a dielectric clad cylindrical array and that of an element in the corresponding planar array. This result suggests that the coverage of a finite dimension array over a cylinder of large radius can be evaluated with good approximation by the means of a planar array model. The coverage of arrays in an infinite ground plane covered by dielectric is predicted by developing a model which takes into account several waveguide modes in matching the fields at the array aperture interface. This model does not require the inversion of large matrices in determining the mutual coupling between array elements, thus permitting the analysis of relatively large arrays. This model shows that no coverage in the endfire direction is obtainable from these structures. To achieve endfire coverage the dielectric sheet covering the array must be of finite dimension.

The coverage from a finite planar array covered by a finite dielectric slab is predicted by assuming a simple but effective model of the radiation from the wedge terminating the dielectric sheet. This model shows that it is possible to obtain substantial coverage in the endfire direction by properly shaping the wedge at the expense of some pattern distortions. The overall array performance shows that it is possible to obtain hemispheric scan coverage with maximum gain oscillation of no more than 6.5 dB.

DD FORM 1 NOV 65 1473

UNCLASSIFIED
Security Classification

14. KEY WORDS	LINK A		LINK B		LINK C	
	ROLE	WT	ROLE	WT	ROLE	WT
Conformal Arrays Cylindrical Arrays Dielectric Cover Dielectric Wedge						

TABLE OF CONTENTS

TABLE OF CONTENTS (Cont.)

LIST OF ILLUSTRATIONS

1. INTRODUCTION AND SUMMARY

This Scientific Report summarizes the studies performed during 1972 for AFCRL under Contract No. F19628-72-C-0202. The objective of the study program is the investigation of techniques to obtain hemispheric scan coverage (no more than 6 dB antenna gain fall off or oscillation over the hemisphere) by using an array of waveguide apertures covered by a dielectric slab. The array is on a cylindrical ground plane of large radius ($R \approx 100\,\lambda$) and its aperture gain is between 20 and 30 dB above isotropic. The most significant result of the study is that hemispheric scan coverage is indeed achievable with dielectric covered arrays.

The analytical study of the radiation from an array of waveguide apertures covered by dielectric has been developed in three steps.

In a first phase of the study the properties of infinite cylindrical arrays covered dielectric have been investigated. The problem has been approached by separately enforcing the continuity of the EM fields at the air-dielectric and at the dielectric-cylinder interface.

The continuity of the EM fields at the air-dielectric interface is enforced by representing in both media the fields as a superposition of modes LSE and LSM with respect to the direction of the axis of the cylinder. The curvature of the air-dielectric interface causes coupling between LSE and LSM modes, which are decoupled in the planar case. The matching of the fields at the second interface is performed by resorting to the "eigenexcitation" method, presented in a previous report [1]. The fields external to the cylinder are represented by a set of space harmonics matching the symmetry of the array excitation and the field in the waveguide elements by a superposition of normal waveguide modes. The continuity of the fields is enforced by using Galerkin's method. This rigorous analysis of dielectric clad cylindrical arrays leads to rather involved expressions for the element driving point admittance and for the far fields. An approximate analysis is introduced to simplify the design of these structures. A number of numerical examples illustrates the good approximation given by the

simplified analysis in the case of large cylinders. Numerical results are presented for the case of an array on a cylinder with radius of approximately 100 λ. The array element patterns show the presence of resonance dips much more pronounced than the notches due to grating lobe phenomena.

The computations show that there are only minor differences in the element pattern and in driving point admittance between dielectric-clad cylindrical arrays of large radius and the corresponding planar arrays. These results indicate that the coverage performance of a finite dimension array (aperture gain 20 - 30 dB) over a large cylinder can be evaluated with excellent approximation by the means of a plane array model.

In the second phase of this study program efforts were directed at the investigation of the radiation properties of finite arrays of waveguide elements in an infinite ground plane covered by an infinite dielectric sheet. The main result of the second part of the studies consists of a method of analysis of finite arrays. The method is based on enforcing the continuity at the array apertures of the space waves, represented by a Fourier double integral, and of the fields in the waveguides, represented as a superposition of waveguide modes. This method, since it does not require the inversion of large matrices in determining of the mutual coupling coefficients between array elements is especially valuable in the analysis of large arrays of waveguide elements. Computations of the coverage of an array of 61 circular waveguide elements show that it is not possible to obtain hemispheric coverage from arrays in an infinite ground plane covered by dielectric. No radiation can take place in directions close to endfire because the energy leaving the array is trapped in a surface wave propagating along the dielectric sheet. In order to achieve endfire coverage the energy bound to the surface wave must be radiated in free space by terminating the dielectric sheet.

In the last phase of the program the radiation properties of surface wave excited dielectric wedges have been studied by generating a transmission line model. The patterns and the reflection coefficients of several tapered two-dimensional wedges were investigated. It has been found that for dielectric tapers over 1λ long there is practically no reflection of the surface wave at the wedge discontinuity. From the two dimensional wedge model a simple model of three-dimensional wedges has been generated to evaluate the radiation from finite arrays covered by finite slabs of dielectric

in an infinite ground plane. The analytical results show that, by properly tapering the dielectric wedge, it is possible to obtain hemispheric scan coverage from an array of 20 - 30 dB aperture gain. In the conical region of ≈65 deg semiaperture around the array normal the coverage is provided by the space wave radiated by the elements, while the endfire and near endfire coverage is provided by the radiation from the tapered wedge. The interference between the space wave and the wedge radiation produces high sidelobes in the array pattern at certain scan angles.

This report is organized in three sections summarizing the three phases of the study program. In Section 2 the analysis and the numerical results relative to infinite periodic cylindrical arrays covered by dielectric are presented. Section 3 is devoted to the analysis of finite planar arrays in an infinite ground plane covered by a dielectric sheet over an infinite ground plane. Section 4 deals with finite arrays covered by a finite dielectric sheet. The appendices of the report present with some detail the justification of the mathematical models used in evaluating the radiation from dielectric covered arrays.

2. ANALYSIS OF PERIODIC ARRAYS OF WAVEGUIDE APERTURES ON CONDUCTING CYLINDERS COVERED BY DIELECTRIC

2.1 General Remarks

Cylindrical arrays covered by dielectric are suited for airborne and missile borne application as the dielectric layer provides a natural radome for the antenna.

The radiation from slots on a cylinder covered by dielectric has been studied by several authors and a fairly extensive literature exists on this topic. Early works by Wait and Mientka [2] and Wait and Conda [3] are based on representing the fields external to a cylinder as a superposition of modes TE and TM to the direction of the cylinder axis and on enforcing the continuity of the tangential fields at the dielectric discontinuity.

More recently Sureau and Hessel [4] have performed a mutual coupling analysis for arrays of thin infinite axial slits on cylinders covered by dielectric. Their analysis resorts to expanding the fields external to the cylinder in modes LSE [5] with respect to the radial direction. Sureau and Hessel show the presence of resonance dips in the array element pattern. The axial slit model, although it gives some excellent physical insights, represents an idealized structure and does not provide the complete information required for a three-dimensional array design.

In this report a systematic analysis of cylindrical arrays of waveguide apertures covered by dielectric is presented with the aim of providing an effective design tool for these antennas. The approach taken consists in expanding the fields external to cylinder in modes LSE and LSM [6] with respect to the axial direction and enforcing the continuity of the tangential fields at the dielectric discontinuity. The field matching at the array aperture is performed by resorting to the "eigenexcitation" method [1]. For each array eigenexcitation the field continuity at the waveguide aperture is enforced by applying Galerkin's method [7].

2.2 Reflection at Cylindrical Dielectric Discontinuities

The reflection of cylindrical waves at cylindrical dielectric discontinuities has been studied by several authors [8-9] and has resulted in expressions for the fields which are rather involved and without clear physical interpretation. In this section the analysis of cylindrical discontinuities is performed to point out some phenomena at these discontinuities and to cast the results in a form readily usable for phased array analysis. Since only cylindrical dielectric discontinuities are dealt with in this section, there is no need to specify the array structure other than the radius of the cylindrical array and the external radius of the dielectric layer.

With reference to Figure 1, the dielectric region ($a \leq \rho \leq b$) and the free space region ($b \leq \rho$) can be thought of as two series radial transmission lines with a discontinuity in the dielectric loading at $\rho = b$.

The fields in the two radial transmission lines can be represented as a superposition of modes LSE and LSM with respect to the axial direction $\hat{z}$ [6]. In the free space region only outward propagating waves are present and the following expressions hold for the transverse (to $\hat{\rho}$) fields.

LSE Modes

$$H_z = \sum_{n=-\infty}^{+\infty} e^{-jn\phi} \int_{-\infty}^{+\infty} F(n,w)\, H_n^{(2)}\left(\rho \sqrt{k^2 - w^2}\right) e^{-jwz}\, dw \qquad (1)$$

$$E_\phi = \sum_{n=-\infty}^{+\infty} j e^{-jn\phi} \frac{k}{\eta} \int_{-\infty}^{+\infty} \frac{F(n,w)}{\sqrt{k^2 - w^2}} H_n'^{(2)}\left(\rho\sqrt{k^2 - w^2}\right) e^{-jwz}\, dw \qquad (2)$$

$$H_\phi = -\sum_{n=-\infty}^{+\infty} e^{-jn\phi} \frac{1}{r} \int_{-\infty}^{+\infty} \frac{nwF(n,w)}{k^2 - w^2} H_n^{(2)}\left(\rho\sqrt{k^2 - w^2}\right) e^{-jwz}\, dw \qquad (3)$$

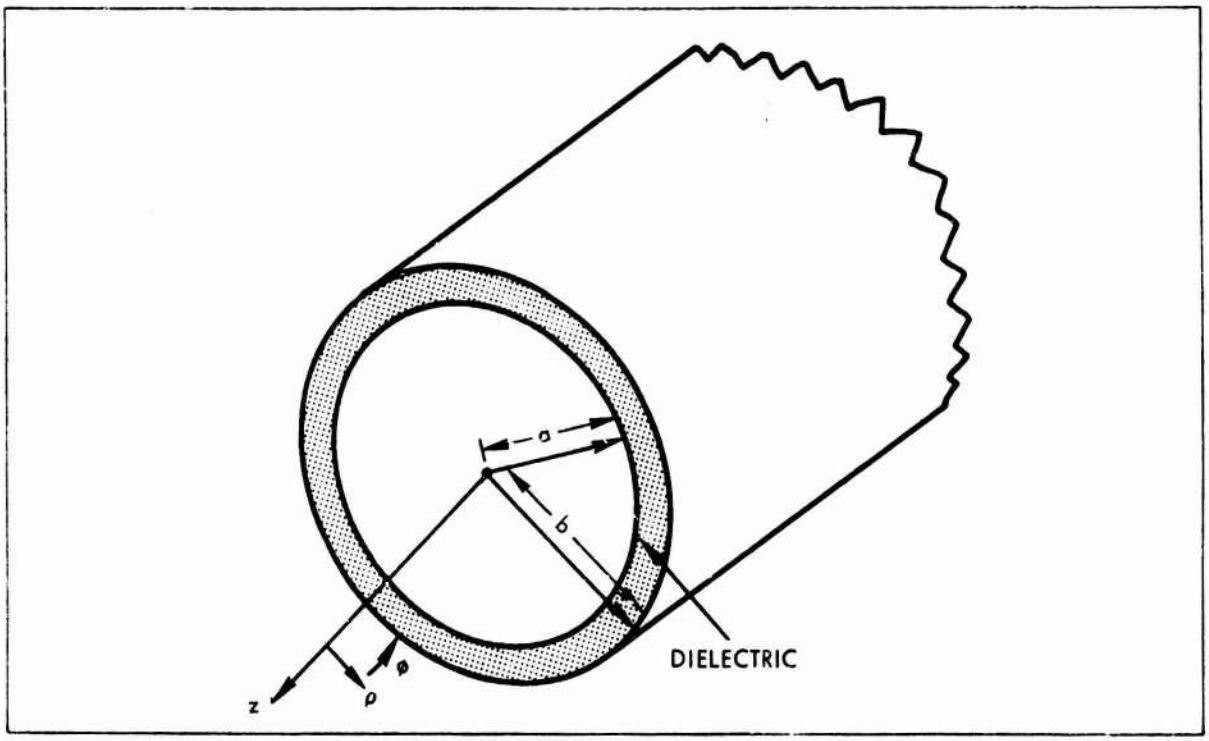

Figure 1 - Geometrical Reference

LSM Modes

$$E_z = \sum_{n=-\infty}^{+\infty} e^{-jn\phi} \int_{-\infty}^{+\infty} E(n, w)\, H_n^{(2)} (\rho\sqrt{k^2 - w^2})\, e^{-jwz}\, dw \qquad (4)$$

$$E_\phi = -\sum_{n=-\infty}^{+\infty} e^{-jn\phi}\, \frac{1}{\rho} \int_{-\infty}^{+\infty} \frac{nwE(n, w)}{k^2 - w^2}\, H_n^{(2)} (\rho\sqrt{k^2 - w^2})\, e^{-jwz}\, dw \qquad (5)$$

$$H_\phi = -\sum_{n=-\infty}^{+\infty} e^{-jn\phi}\, j\frac{k}{\zeta} \int_{-\infty}^{+\infty} \frac{E(n, w)}{\sqrt{k^2 - w^2}}\, H_n'^{(2)} (\rho\sqrt{k^2 - w^2})\, e^{-jwz}\, dw \qquad (6)$$

In Equations (1) - (6) $H_n^{(2)}$ is a Hankel function, $H_n'^{(2)}$ its derivative with respect to the argument, F(n, w) and E(n, w) are the modal currents and voltages respectively, w is the wave number in the axial direction, ζ [illegible]

η are the free space impedance and admittance respectively. For $w > k$ the outward propagating waves are represented by $H_n^{(2)}\left(-j\rho\sqrt{w^2 - k^2}\right)$. The selected modal representation is analogous to the expansion in TE and TM modes (with respect to the array normal) of the space harmonics in planar array theory [7]. This can be seen by introducing Equations (1) - (6) in the radial component field equations [13] and taking the limit for $\rho \to \infty$. In the dielectric region outward and inward propagating waves are present and the fields can be represented by:

LSE Modes

$$H_z = \sum_{n=-\infty}^{+\infty} e^{-jn\phi} \int_{-\infty}^{+\infty} I(\rho, n, w)\, e^{-jwz}\, dw \tag{7}$$

$$I(\rho, n, w) = C(n, w)\, H_n^{(2)}\left(\rho\sqrt{k_\epsilon^2 - w^2}\right) + D(n, w)\, H_n^{(1)}\left(\rho\sqrt{k_\epsilon^2 - w^2}\right) \tag{8}$$

$$E_\phi = \sum_{n=-\infty}^{+\infty} je^{-jn\phi}\, \frac{k_\epsilon}{\eta_\epsilon} \int_{-\infty}^{+\infty} \frac{1}{k_\epsilon^2 - w^2}\, \frac{d}{d\rho}\, I\,(\rho, n, w)\, e^{-jwz}\, dw$$

$$H_\phi = \sum_{n=-\infty}^{+\infty} e^{-jn\phi}\, \frac{1}{\rho} \int_{-\infty}^{+\infty} \frac{n\, w}{k_\epsilon^2 - w^2} I\,(\rho, n, w)\, e^{-jwz}\, dw \tag{9}$$

LSM Modes

$$E_z = \sum_{n=-\infty}^{+\infty} e^{-jn\phi} \int_{-\infty}^{+\infty} V(\rho, n, w)\, e^{-jwz}\, dw \tag{10}$$

$$V(\rho, n, w) = A(n, w)\, H_n^{(2)}\left(\rho\sqrt{k_\epsilon^2 - w^2}\right) + B(n, w)\, H_n^{(1)}\left(\rho\sqrt{k_\epsilon^2 - w^2}\right) \tag{11}$$

$$E_\phi = -\sum_{n=-\infty}^{+\infty} e^{-jn\phi}\,\frac{1}{\rho}\int_{-\infty}^{+\infty}\frac{n\,w}{k_\epsilon^2 - w^2}\,V(\rho, n, w)\,e^{-jwz}\,dw$$

$$H_\phi = -\sum_{n=-\infty}^{+\infty} je^{-jn\phi}\,\frac{k_\epsilon}{\zeta_\epsilon}\int_{-\infty}^{+\infty}\frac{1}{k_\epsilon^2 - w^2}\,\frac{d}{d\rho}\,V(\rho, n, w)\,e^{-jwz}\,dw \tag{12}$$

In Equations (7) - (12) A(n, w) and B(n, w) are the voltage amplitudes of the incident and reflected LSM modes, C(n, w) and D(n, w) are the current amplitudes for the incident and reflected LSE modes. The Hankel functions $H_n^{(2)}$ and $H_n^{(1)}$ represent an outward and an inward propagating wave, $H_n^{\prime(2)}$ and $H_n^{\prime(1)}$ are the derivatives of $H_n^{(2)}$ and $H_n^{(1)}$ with respect to the argument. k_ϵ, ζ_ϵ, η_ϵ represent the propagation constant, the characteristic impedance and the characteristic admittance in the dielectric region. For $w > k_\epsilon$ the outward and the inward propagating waves are represented by $H_n^{(2)}\left(-j\rho\sqrt{w^2 - k_\epsilon^2}\right)$ and $H_n^{(1)}\left(-j\rho\sqrt{w^2 - k_\epsilon^2}\right)$ respectively, to satisfy the radiation condition.

By enforcing the continuity of all the transverse field components (Appendix A) at r = b, the following expressions for the amplitudes of the transmitted and reflected fields are obtained:

$$F(n, w) = C(n, w)\,\frac{H_n^{(2)}\left(b\sqrt{k_\epsilon^2 - w^2}\right)}{H_n^{(2)}\left(b\sqrt{k^2 - w^2}\right)} + D(n, w)\,\frac{H_n^{(1)}\left(b\sqrt{k_\epsilon^2 - w^2}\right)}{H_n^{(2)}\left(b\sqrt{k^2 - w^2}\right)} \tag{13}$$

$$E(n, w) = A(n, w)\,\frac{H_n^{(2)}\left(b\sqrt{k_\epsilon^2 - w^2}\right)}{H_n^{(2)}\left(b\sqrt{k^2 - w^2}\right)} + B(n, w)\,\frac{H_n^{(1)}\left(b\sqrt{k_\epsilon^2 - w^2}\right)}{H_n^{(2)}\left(b\sqrt{k^2 - w^2}\right)} \tag{14}$$

$$B(n, w) = \Gamma^{E}(n, w)\, A(n, w) + \Gamma^{HE}(n, w)\, C(n, w) \tag{15}$$

$$D(n, w) = \Gamma^{EH}(n, w)\, A(n, w) + \Gamma^{H}(n, w)\, C(n, w) \tag{16}$$

The explicit expressions for $\Gamma^{E}(n,w)$, $\Gamma^{HE}(n,w)$, $\Gamma^{EH}(n,w)$, $\Gamma^{H}(n,w)$ are given in Appendix A.

It should be noticed from Equations (15) - (16) that there is cross coupling between LSE and LSM modes, which are decoupled for an infinite planar dielectric interface. The cross coupling terms $\Gamma^{EH}(n,w)$ and $\Gamma^{HE}(n,w)$ are due to the curvature of the dielectric discontinuity and tend to zero as $b \to \infty$. For $b \to \infty$, $\Gamma^{E}(n,w)$ and $\Gamma^{H}(n,w)$ tend to the plane case values as shown in Appendix A.

2.3 Infinite Cylindrical Arrays of Waveguide Apertures Covered by Dielectric

2.3.1 Aperture Field Matching

The model of the array consists of a regular grid of circular apertures of radius r_e, fed by a waveguide of the same cross section on an infinite cylindrical surface of radius "a". The array lattice is defined by two vectors $\underline{s}_1$ and $\underline{s}_2$ as shown in Figure 2 where the axial and circumferential spacings between elements are called 2h and d respectively. The array has N elements in each circumferential ring. The dielectric layer covering the array has an external radius b and a dielectric constant ϵ. The array waveguides are filled with dielectric with dielectric constant ϵ'. Only the two orthogonal TE_{11} modes are assumed to be propagating in the waveguide.

The element aperture transverse electric field distribution will be assumed to be represented with good accuracy by a superposition of Q waveguide modes (the two TE_{11}'s plus higher order modes). The vector mode functions for the TE_{11} polarized in the axial and circumferential direction will be denoted by $\underline{e}_1$ (s) and $\underline{e}_2$ ($\underline{s}$) respectively, $\underline{s}$ being a position vector. The higher order modes e_s ($\underline{s}$) are ordered by decreasing cutoff-frequency.

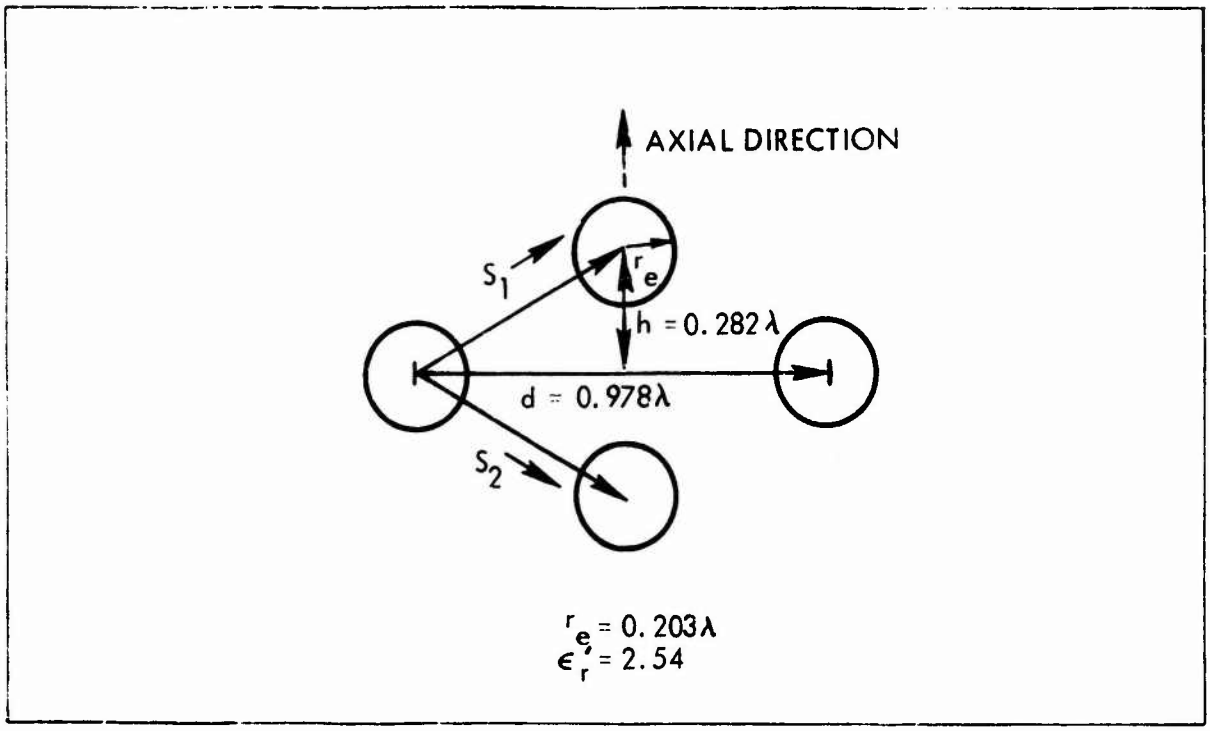

Figure 2 - Cylindrical Array Lattice

In matching the tangential fields at the array dielectric interface the eigenexcitation method will be used. The eigenexcitation approach to the analysis of cylindrical arrays has been presented in detail in previous reports [1-15].

Let the element ports of the axial mode be excited by the eigenexcitation $\underline{e}(\underline{u}_o)$ [1]; then the transverse electric field at the array elements is given by:

$$\underline{E}_t(\underline{s}) = \sum_{m=0}^{N-1} \sum_{r=-\infty}^{\infty} e^{-j\underline{u}_o(m\underline{s}_1 + r\underline{s}_2)} \left\{ \sum_{s=1}^{Q} [\delta_{1s} + \Gamma_s(\underline{u}_o)\underline{e}_s(\underline{s} - m\underline{s}_1 - r\underline{s}_2) \right\} \quad (17$$

where $\Gamma_1(\underline{u}_o)$ is the reflection coefficient of the actively excited axial TE_{11} mode, and the other $\Gamma_s(\underline{u}_o)$ represent the coupling coefficients of the modes passively excited. In Equation (17) δ_{1s} is Kronecker's delta and $\underline{s}$ is a position vector over the array surface defined by its components $(a\phi, z)$.

From the results of the previous section the electric field in the dielectric region can be represented by a superposition of LSE and LSM modes. Their expression is obtained by inserting Equations (15) and (16) in Equations (7) - (12).

By enforcing the continuity of the tangential electric field at the array-dielectric interface, the following expressions are established for the amplitude of the external fields (Appendix B).

$$A(i + pN, w) = \frac{1}{2\pi} \sum_{q=-\infty}^{+\infty} \Bigg\{ \bar{\mathcal{E}}_z(\underline{u}_o, w)\, R^{E}(i+pN, w) + j \frac{\eta_\epsilon k_{\rho\epsilon}}{k_\epsilon} \Bigg[\frac{1}{a} \frac{(i+pN)w}{k_\epsilon^2 - w^2} \bar{\mathcal{E}}_z(\underline{u}_o, w) + \bar{\mathcal{E}}_\phi(\underline{u}_o, w) \Bigg] R^{HE}(i+pN, w) \Bigg\} \delta(w - w_{opq}) \tag{18}$$

$$C(i + pN, w) = \frac{1}{2\pi} \sum_{q=-\infty}^{+\infty} \Bigg\{ \bar{\mathcal{E}}_z(\underline{u}_o, w) R^{EH}(i+pN, w) - j \frac{\eta_\epsilon k_{\rho\epsilon}}{k_\epsilon} \Bigg[\frac{1}{a} \frac{(i+pN)w}{k_\epsilon^2 - w^2} \bar{\mathcal{E}}_z(\underline{u}_o, w) + \bar{\mathcal{E}}_\phi(\underline{u}_o, w) \Bigg] R^{H}(i+pN, w) \Bigg\} \delta(w - w_{opq}) \tag{19}$$

In Equations (18) and (19) $\delta(w-w_{opq})$ is the Dirac delta function $k_{\rho\epsilon} = \sqrt{k_\epsilon^2 - w^2}$, $\bar{\mathcal{E}}_z(\underline{u}_o, w)$ and $\bar{\mathcal{E}}(\underline{u}_o, w)$ are components of the vector:

$$\bar{\mathcal{E}}(\underline{u}_o, w) = \frac{2\pi N}{h} \Bigg\{ \frac{1}{a} \sum_{s=1}^{Q} \Big[\delta 1s + \Gamma_s(\underline{u}_o) \Big] \mathcal{E}_s\left(\frac{i+pN}{a}, w\right) \Bigg\}$$

where $\underline{\mathcal{E}}_s\left(\frac{i+pN}{a}, w\right)$ are the Fourier transforms of the vector mode functions $\underline{e}_s(s)$. The definition of R^E (i+pN, w), R^{HE} (i+pN, w), and R^{EH} (i+pN, w) and R^H (i+pN, w) are given in Appendix B. Introducing Equations (18) and (19) in the LSE and LSM mode expressions one can directly verify that the external tangential electric field is expressed by a Floquet's double series having the periodicity of the array structure.

The continuity of the tangential magnetic field can be approximately enforced by applying a procedure analogous to the plane case [7-12]. The tangential magnetic field at the reference element aperture is given by:

$$\underline{H}_t^-(s) = \hat{\rho}_o \times \sum_{s=1}^{Q} Y_s \left[\delta_{1s} - \Gamma_s (\underline{u}_o) \right] \underline{e}_s(\underline{s}) \tag{20}$$

$\hat{\rho}_0$ being a unit vector in the direction of the external normal at the reference element. The external tangential magnetic field is given by the following Floquet's expansion (Appendix B)

$$\underline{H}_t^+(\underline{s}) = \frac{1}{2\pi} \sum_{p=-\infty}^{+\infty} \sum_{q=-\infty}^{+\infty} e^{-j\underline{u}_{opq}\underline{s}} \Big\{ \left[a(\underline{u}_{opq})\, \bar{\mathcal{E}}_\phi(\underline{u}_{opq}) + b(\underline{u}_{opq})\, \bar{\mathcal{E}}_z(\underline{u}_{opq}) \right] \hat{z} - \left[c(\underline{u}_{opq})\, \bar{\mathcal{E}}_\phi(\underline{u}_{opq}) + d(\underline{u}_{opq})\, \bar{\mathcal{E}}_z(\underline{u}_{opq}) \right] \hat{\phi} \Big\} \tag{20a}$$

If the equality of $\underline{H}_t^-(\underline{s})$ and $\underline{H}_t^+(\underline{s})$ is approximately enforced, the following set of linear equations is obtained for the $\Gamma_s(\underline{u}_o)$ (Appendix B):

$$Y_k \left[\delta_{1k} - \Gamma_k(\underline{u}_o) \right] = \sum_{s=1}^{Q} \left[\delta_{1s} + \Gamma_s(\underline{u}_o) \right] L_{ks}(\underline{u}_o) \quad (k, s = 1, \ldots Q) \tag{21}$$

where δ_{1k} and δ_{1s} are Kronecker deltas and L_{ks} ($\underline{u}_c$) are mutual admittances between modes for a given eigenexcitation. The rather involved expressions of L_{ks} ($\underline{u}_o$) are given in Appendix B. By solving the system of Equation (21), the tangential electric field distribution at the waveguide apertures is determined for each eigenexcitation so that the array element pattern can be evaluated. This will be discussed in the next section.

So far only the axial mode has been actively excited. If the circumferential TE_{11} is actively excited, a system of equations analogous to Equation (21) is obtained by applying the procedure described for the active excitation of the TE_{11} mode axially polarized. The new system of equations is obtained from Equation (21) by interchanging the index 1 with the index 2. The response to the general excitation is obtained by superposition.

2.3.2 Eigenpatterns-Array Element Pattern

The far field of the eigenexcitations can be found by employing the expansions (Equations (28) and (22)) of the tangential electric field on the array and by using Equations (13) and (14) for the transmitted fields at the air-dielectric interface.

With the notation of the preceding paragraph, at r = b the transmitted field amplitudes are given by:

$$F(i+pN, w) = \frac{C(i+pN, w)}{H^{(2)}_{i+pN}(bk_\rho)} \left| H^{(2)}_{i+pN}(bk_{\rho\epsilon}) + \Gamma^{H}_{(i+pN, w)} H^{(1)}_{i+pN}(bk_{\rho\epsilon}) \right| \qquad (22)$$

$$+ \frac{A(i+pN, \_\_)}{H^{(2)}_{i+pN}(bk_\rho)} \Gamma^{EH}(i+pN, w) H^{(1)}_{i+pN}(bk_{\rho\epsilon})$$

$$E(i + pN,\ w) = \frac{A(i + pN, w)}{H^{(2)}_{i+pN}(bk_\rho)} \left| H^{(2)}_{i+pN}(bk_{\rho\epsilon}) + \Gamma^{E}(i + pN,\ w)\, H^{(1)}_{i+pN}(bk_{\rho\epsilon}) \right|$$

$$+ \frac{C(i + pN,\ w)}{H^{(2)}_{i+pN}(bk_\rho)} \Gamma^{HE}_{(i+pN, w)}\, H^{(1)}_{i+pN}(bk_{\rho\epsilon}) \tag{23}$$

where $k_\rho = \sqrt{k^2 - w^2}$. The electric field at any point (ρ, ϕ, z) is expressed by a Floquet's double series:

$$E_z(\rho, \phi, z) = \sum_{p=\infty}^{+\infty}\sum_{p=\infty}^{+\infty} E(\underline{u}_{opq})\, H^{(2)}_{i+pN}\left(\rho\sqrt{k^2 - w^2_{opq}}\right) e^{-j(i+pN)\phi} e^{-jw_{opq}z} \tag{24}$$

$$E_\phi(\rho, \phi, z) = \sum_{p=-\infty}^{+\infty}\sum_{p=-\infty}^{+\infty} \left\{ \frac{1}{\rho} \frac{(i+pN)w_{opq}}{k^2 - w^2_{opq}} E(\underline{u}_{opq})\, H^{(2)}_{i+pN}\left(\rho\sqrt{k^2 - w^2_{opq}}\right) \right.$$

$$\left. + j\frac{k}{\eta} \frac{F(\underline{u}_{opq})}{\sqrt{k^2 - w^2_{opq}}} H'^{(2)}_{i+pN}\left(\rho\sqrt{k^2 - w^2_{opq}}\right) \right\} e^{-j(i+pN)\phi} e^{-jw_{opq}z} \tag{25}$$

The components of the far field of an eigenexcitation can be simply evaluated from Equations (24) and (25) applying straightforward asymptotic expansions of the Hankel functions.

The asymptotic expansions for the electric field are found to be given by:

$$\lim_{\rho \to \infty} E_z = \sum_{|w_{opq}| \le k} \sum_{p=-\infty}^{+\infty} E(u_{opq}) \sqrt{\frac{2j}{\pi \rho \sqrt{k^2 - w_{opq}^2}}}\, j^{(i+pN)}\, e^{-j(i+pN)\phi} \qquad (26)$$

$$e^{-j\left(\rho\sqrt{k^2 - w_{opq}^2} + z\, w_{opq}\right)}$$

$$\lim_{\rho \to \infty} E_\phi = \sum_{|w_{opq}| \le k} \sum_{p=-\infty}^{+\infty} \frac{k}{\eta} \frac{F(u_{opq})}{\sqrt{k^2 - w_{opq}^2}} \sqrt{\frac{2j}{\pi \rho \sqrt{k^2 - w_{opq}^2}}}\, j^{(i+pN)} \qquad (27)$$

$$e^{-j(i+pN)\phi}\, e^{-j\left(\rho\sqrt{k^2 - w_{opq}^2} + z w_{opq}\right)}$$

The components of the far field of the eigenexcitations can be expressed in spherical coordinates (r, θ, ϕ) in terms of an E_θ and E_ϕ component which are obtained from Equations (26) and (27) by a simple coordinate transformation [1]. With straightforward manipulations, the far field $\vec{g}(r, \theta, \phi, i)$ of the eigenexcitations is established as:

$$\vec{g}(r, \theta, \phi, i) = \sqrt{\frac{2j}{\pi r \sin\theta}} \sum_{|w_{opq}| \le k} \left[\hat{\theta} g_\theta(\theta, \phi, i) + \hat{\phi} g_\phi(\theta, \phi, i)\right] \qquad (28)$$

$$\frac{e^{ji\left(\frac{\pi}{2} - \phi\right)}\, e^{-jr\left(w_{opq}\cos\theta + \sqrt{k^2 - w_{opq}^2}\sin\theta\right)}}{\left(k^2 - w_{opq}^2\right)^{1/4}}$$

where g_θ and g_ϕ are defined as follows:

$$g_\theta(\theta, \phi, i) = k \sum_{p=-\infty}^{+\infty} \frac{E(\underline{u}_{opq})}{\sqrt{k^2 - w_{opq}^2}} e^{-jpN(\frac{\pi}{2} - \phi)}$$

$$g_\phi(\theta, \phi, i) = \frac{k}{\eta} \sum_{p=-\infty}^{+\infty} \frac{F(\underline{u}_{opq})}{\sqrt{k^2 - w_{opq}^2}} e^{-jpN(\frac{\pi}{2} - \phi)}$$

The array element pattern is obtained by summing the contribution of all eigenexcitations [1] and is expressed by:

$$\vec{F}(r, \theta, \phi) = \sqrt{\frac{2j}{\pi r \sin\theta}} \sum_{|w_{opq}| \leq k} \int_{-\frac{\pi}{2h}}^{\frac{\pi}{2h}} \sum_{i=-N}^{N} e^{-ji(\frac{\pi}{2} - \phi)} [\hat{\theta} g_\theta(\theta, \phi, i)$$

$$+ \hat{\phi} g_\phi(\theta, \phi, i)] \frac{e^{-jr(w_{opq}\cos\theta + \sqrt{k^2 - w_{opq}^2}\sin\theta)}}{(k^2 - w_{opq}^2)^{1/4}} dw_o \quad (29)$$

The integral in Equation (29) can be evaluated for $r \to \infty$ by an application of the stationary phase method obtaining:

$$\vec{F}(r, \theta, \phi) = \sqrt{j}\,\frac{e^{-jkr}}{r} \sum_{|w_{opq}| \leq k} \sum_{i=-N}^{+N} e^{-j(\phi - \frac{\pi}{2})} \left[\hat{\theta} g_{\theta}(\theta, \phi, i) + \hat{\phi} g_{\phi}(\theta, \phi, i)\right] \tag{30}$$

The array pattern for a general excitation is given by an expression analogous to Equation (30), where the eigenpatterns $g_{\theta}(\theta, \phi, i)$ and $g_{\phi}(\theta, \phi, i)$ are weighted by suitable factors depending on the particular array illumination.

2.4 Remarks

In the previous subsections a rigorous method for the analysis of cylindrical arrays covered by dielectric has been established. The results have shown that, due to the curvature of the air-dielectric interface, there is coupling between LSE and LSM radial modes. These coupling phenomena are reflected in rather involved expressions for the driving point admittance and the radiated fields of the eigenexcitations. It has also been shown that as the radius of curvature of the cylinder is increased the coupling between LSE and LSM modes decreases proportionally, so that for zero curvature (planar case) no coupling is present. Cylindrical arrays of large radius of curvature are particularly interesting, since they model a conformal array mounted on the skin of a large aircraft. As this is the most likely application of cylindrical arrays covered by dielectric, in the following paragraphs we will concentrate our attention on cylinders of large radius. For such cylinders (radius $\approx 100\lambda$), the coupling coefficients Γ^{HE} and Γ^{EH} are very small (order of 10^{-3}) with respect to Γ^{E} and Γ^{H} respectively for most of the cylindrical harmonics carrying real power ($n \ll b\sqrt{k_\epsilon^2 - w^2}$) and become appreciable only for harmonics with high circumferential periodicity ($n \approx b\sqrt{k_\epsilon^2 - w^2}$).

If the approximation of setting $\Gamma^{HE} = 0$, $\Gamma^{EH} = 0$ for all harmonics in cylinders of large radius is made, an error will be introduced in the evaluation of the radiated power and of the mutual coupling admittance. This error, however, will affect only the pattern predictions for high scan angles, where the harmonics with high circumferential periodicity are strongly excited. As for the mutual coupling, an error will be introduced in the driving point admittance of the elements relative to the eigenexcitations with $i \approx b\sqrt{k_\epsilon^2 - w^2}$. However, the setting of $\Gamma^{HE} = 0$ and $\Gamma^{EH} = 0$ will result in a substantial simplification of the analysis for cylinders of large radius. If $\Gamma^{HE} = 0$ and $\Gamma^{EH} = 0$, all the formulas of the preceding sections are greatly simplified, allowing much easier evaluation.

In the next subsection particular attention will be devoted to comparing the results between the "rigorous" and the "simplified" approach to the analysis of a large radius ($\approx 100\lambda$) cylinders. It will be shown that the "simplified" method produces acceptable results for most design purposes.

In the previous analysis the presence of a matching network in the array elements has not been taken explicitly into account, because with a proper selection of dielectric constant and thickness of the dielectric sheet covering it should be possible to achieve good broadside matching conditions. Should a matching network in the elements be required to meet specific design purposes, the previous analysis remains valid and only a minor change should be introduced in Equation (21). The matching of cylindrical array elements has been extensively discussed in previous reports [1-15], where the modification for Equation (21) can be found.

2.5 Selected Numerical Examples

In this subsection a number of illustrative examples will be presented to show the effects of a dielectric layer on a cylindrical array.

Several dielectric constants and thicknesses have been considered for the dielectric layer covering the array. As the antenna is intended to be mounted on the skin of an aircraft the dielectric layer should be weather resistant and have good mechanical characteristics. Materials, like the IRTRAN widely used in radome technology, are suitable for this application and have a dielectric constant $\epsilon_r \approx 4$. This value of ϵ_r has been chosen for the computations.

The thickness of the layer should be chosen on the basis of various considerations. In view of future developments a dielectric thickness is selected so as to give rise to surface wave-type phenomena only for scan angles bigger than 60 deg from the element normal. For $\epsilon_r = 4$, this requirement is satisfied by a dielectric thickness of ≈ 0.1 in. The dielectric can be used to provide better matching conditions for the radiating elements than in the case of no dielectric covering, so that matching networks are not required in the element waveguides. To maximize the array gain it is convenient to provide good matching for the eigenexcitations with $i = 0$. This would correspond to broadside match in planar arrays.

Since the dielectric characteristics have roughly been specified, the only free parameters left to achieve the desired match are the element size and the lattice spacing. Several trials have been performed and a satisfactory solution was found with a dielectric thickness of 0.088 in. and the array lattice of Figure 2. The element spacing is 1.1546 in. in the circumferential direction and 0.3333 in. is the spacing between circumferential rings of elements. The cylindrical array has a radius "a" of 113.93 in. corresponding to $\approx 97\lambda$ at 10 GHz, the center frequency for this antenna. There are 620 apertures in one circumferential ring. The array elements are open-ended uniform circular waveguides with 0.24 in. radius. The elements are filled with a dielectric material with $\epsilon_r = 2.54$. Only the two orthogonal TE_{11} modes are above cutoff over the band of this array (10 GHz ± 0.5 GHz), all higher order modes are well below cutoff.

The selected lattice and cylinder radius are very close to a case considered in previous reports [1-15], so the comparison between dielectric covered and uncovered cylindrical arrays will be performed at no cost of additional computations.

While performing the numerical analysis, attention was devoted to the question of relative convergence of the solution [14], peculiar to the application of Galerkin's method. No relative convergence condition is present in this case. It was found that, if nine waveguide modes (the fundamental TE_{11} plus the first eight below cutoff modes) are used in Equation (21), no appreciable variation of the $\Gamma_s(\underline{u}_o)$ is detected by employing additional modes. For each eigenexcitation $\underline{u}_o$ 400 space harmonics have been used in the computations.

Figure 3 shows in the circumferential plane the reflection coefficient of the TE_{11} circumferentially polarized (actively excited) and the excitation coefficients at the element apertures of the higher order modes. The coefficients are plotted versus $u_o = i/a$, the circumferential periodicity of the eigenexcitations. The coefficients have been computed using the "rigorous" method of analysis, whereby the coupling between LSE and LSM modes is taken into account. In Figure 3 the reflection coefficients for an infinite planar array, with the same lattice and dielectric cover, are also shown. As can be seen, no substantial difference exists between the two cases except for high values of $u_o = i/a$.

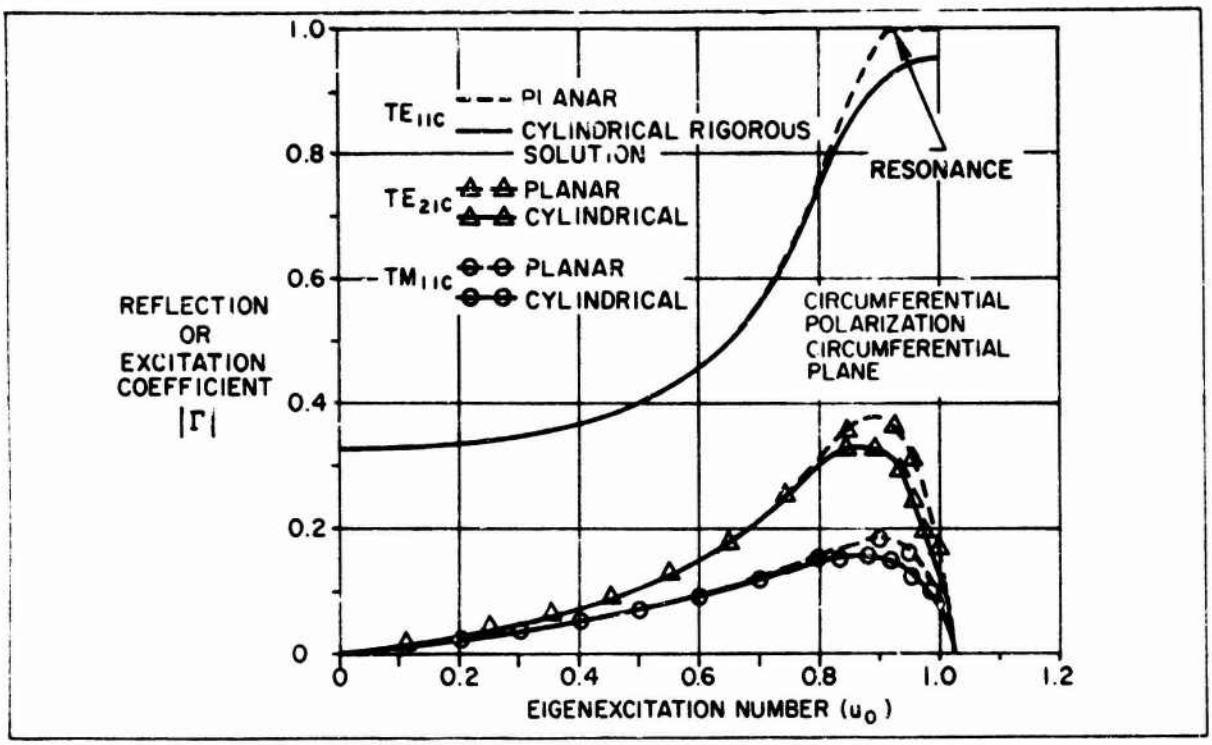

Figure 3 - Modal Excitation

Figure 4 compares the reflection and excitation coefficients obtained by applying the "rigorous" and the "simplified" analysis. The results show no great difference between the two cases except for values of i/a ranging between 0.8 and 1.02. The "simplified" analysis gives coefficients values, which are in between the "rigorous" solution and the planar case and close to the latter. It appears that the "simplified" analysis takes properly into account the curvature of the ground plane, while the curvature of the dielectric interface is "rectified". Figure 5 shows the reflection coefficient and the excitation coefficient (rigorous solution) of the waveguide modes at the element apertures, where the axial TE_{11} mode is actively excited. In the same figure are shown the coefficients obtained by applying the infinite planar array model. For this polarization the difference between the results is always very minor and becomes noticeable only for values of $i/a > 0.9$ and for the TE_{11} mode. In this case the simplified approach gives excellent results for i/a up to 0.95.

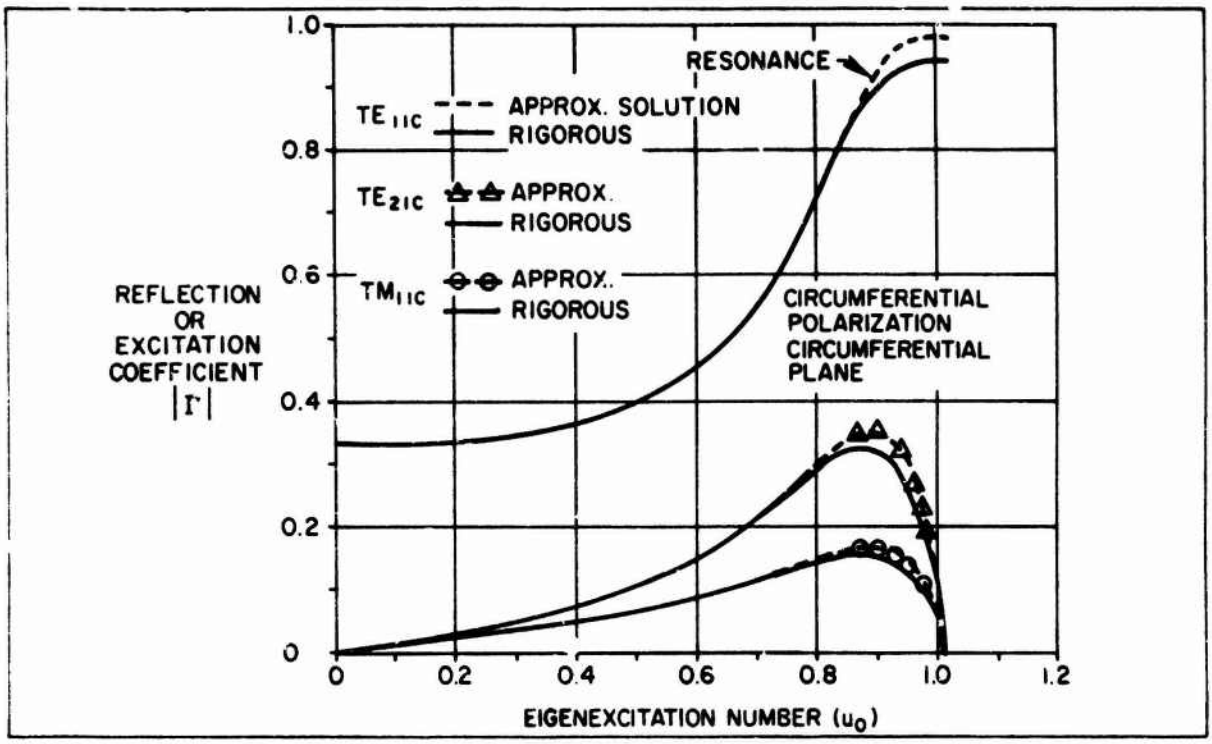

Figure 4 - Modal Excitation

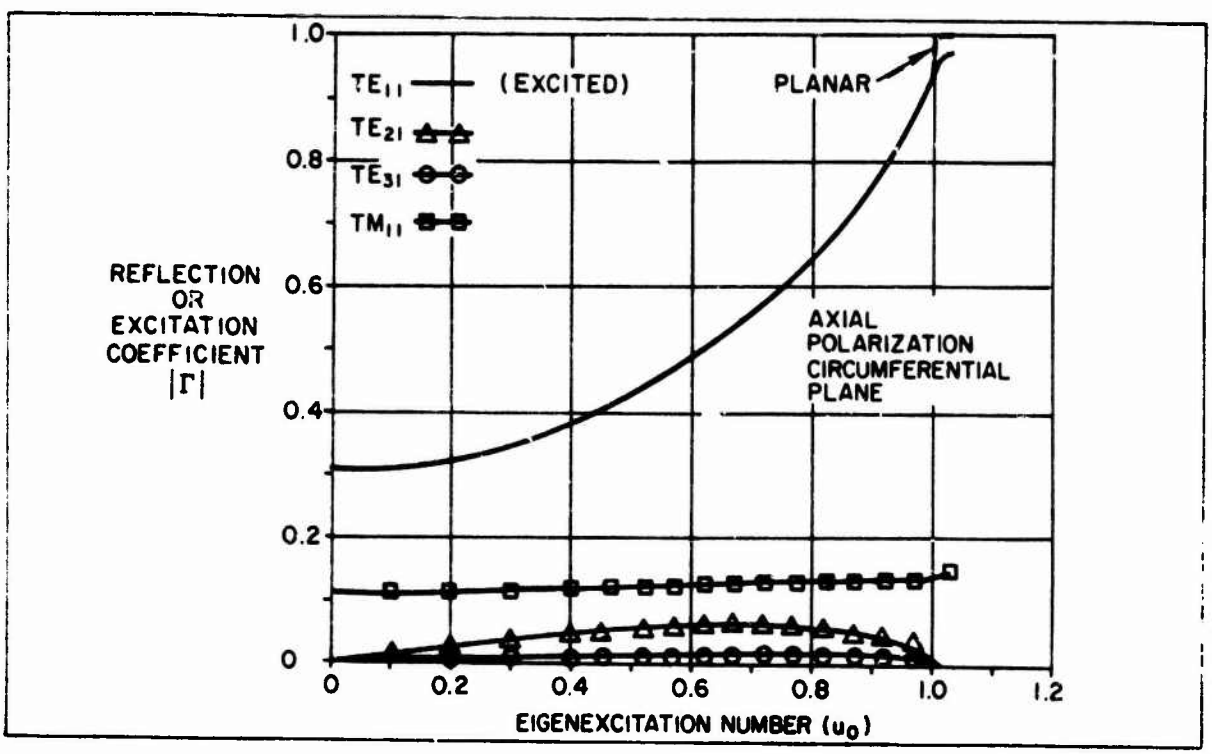

Figure 5 - Modal Excitation

Figure 6 plots the realized gain pattern, in the circumferential plane, of any array element with circumferential polarization actively excited (rigorous solution). On the same figure are shown the pattern of an element in an infinite planar array and the pattern computed following the "approximate" solution. In all three cases a deep notch appears in the patterns. While the cylindrical arrays present a finite notch depth, the infinite planar array has a dip of infinite depth. The nature of these notches has been already explained elsewhere [4] in terms of leaky wave effects and needs no further discussion. It is, however, worth noticing that the minimum of the notch in the cylindrical patterns is slightly closer to the element normal than the position of the null in the plane array pattern, showing a slightly slower leaky wave propagating on the cylindrical array surface. Moreover, it is worth noticing that the "approximate solution gives only the gross features of the element pattern, without reproducing the oscillations around the notch.

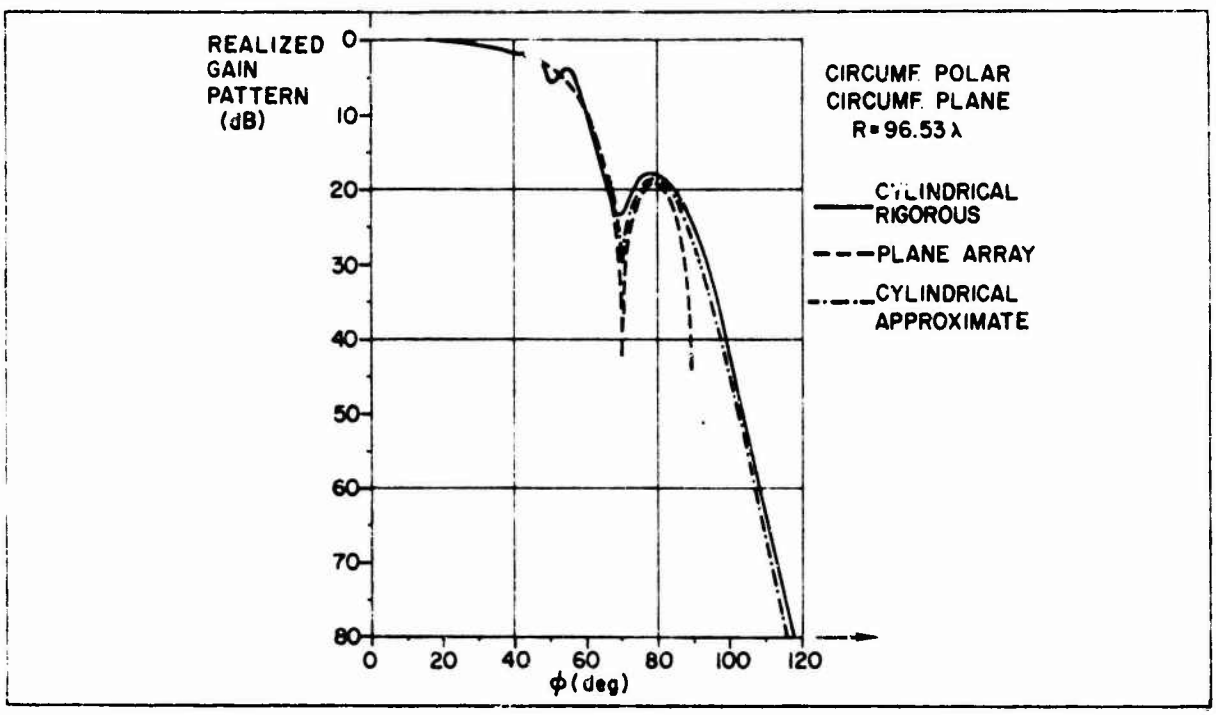

Figure 6 - Array Element Pattern

In Figure 7 the pattern evaluated from the "rigorous" solution is compared with the element pattern of an uncovered cylindrical array with comparable lattice and radius of curvature [1]. It can be seen that the notch caused by the dielectric layer is much deeper than the dip due to grating lobe effects and that the pattern disturbances around the notch are more pronounced in the case of the dielectric covered array. These results are in agreement with the experimental evidence [31] collected for plane arrays, where the notches in the element pattern due to bound waves are always more pronounced than the notches due to grating lobe effects.

In Figure 8 the array element pattern in the circumferential plane for axial polarization is presented. Comparing the "rigorous" and "simplified" cylindrical solution with the plane case, one can see that the differences are very minor up to about 85 deg from the element normal.

In the axial plane practically no difference is present between the cylindrical and the plane array element pattern. In Figures 9 and 10 the realized gain of an element is plotted for circumferential and axial polarization respectively.

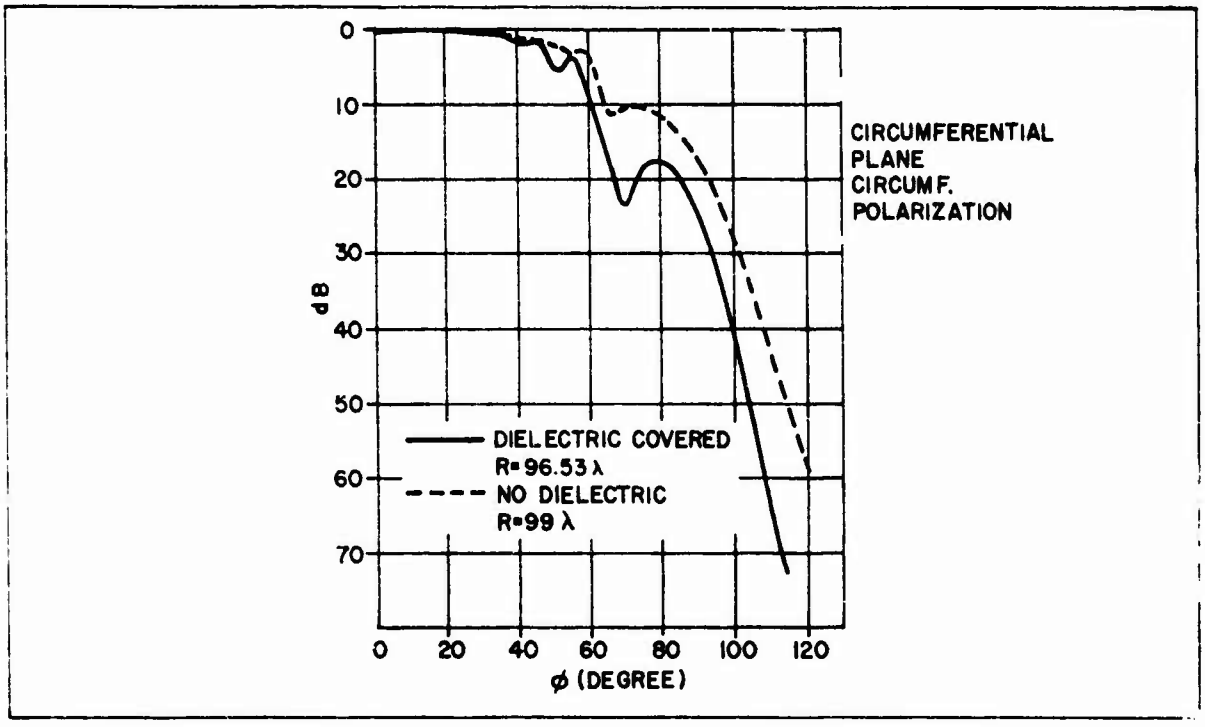

Figure 7 - Array Element Pattern

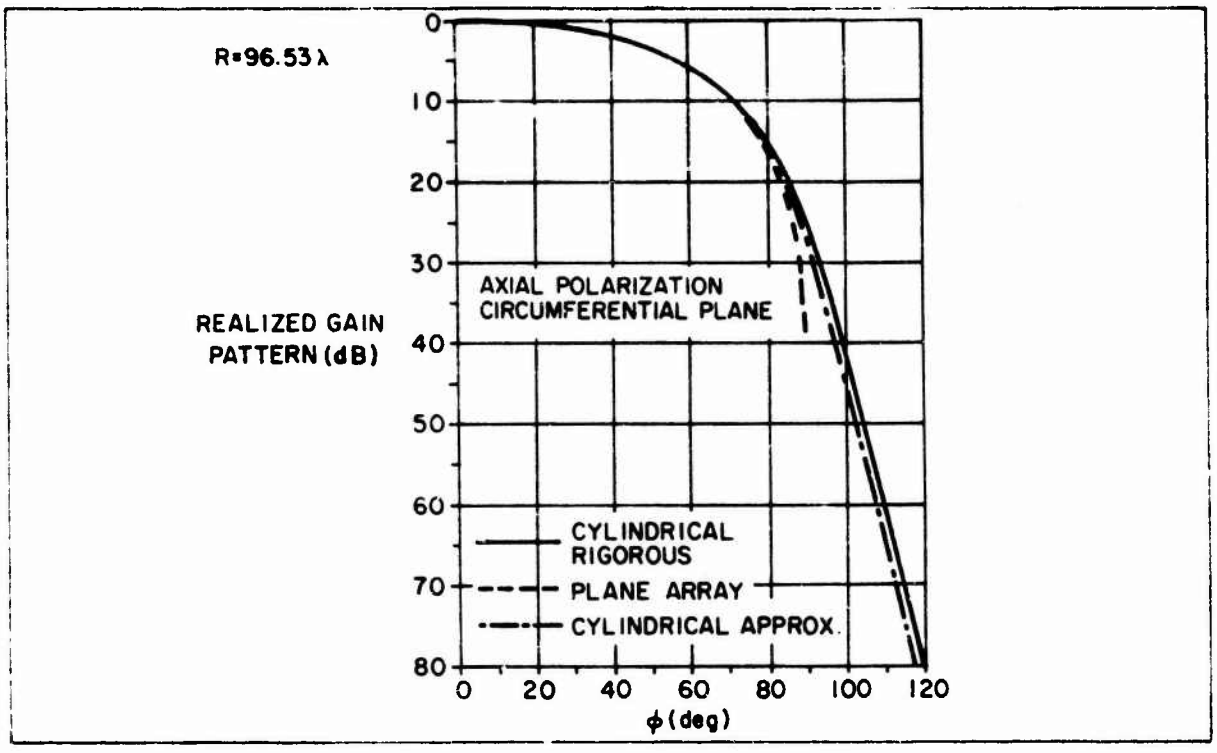

Figure 8 - Array Element Pattern

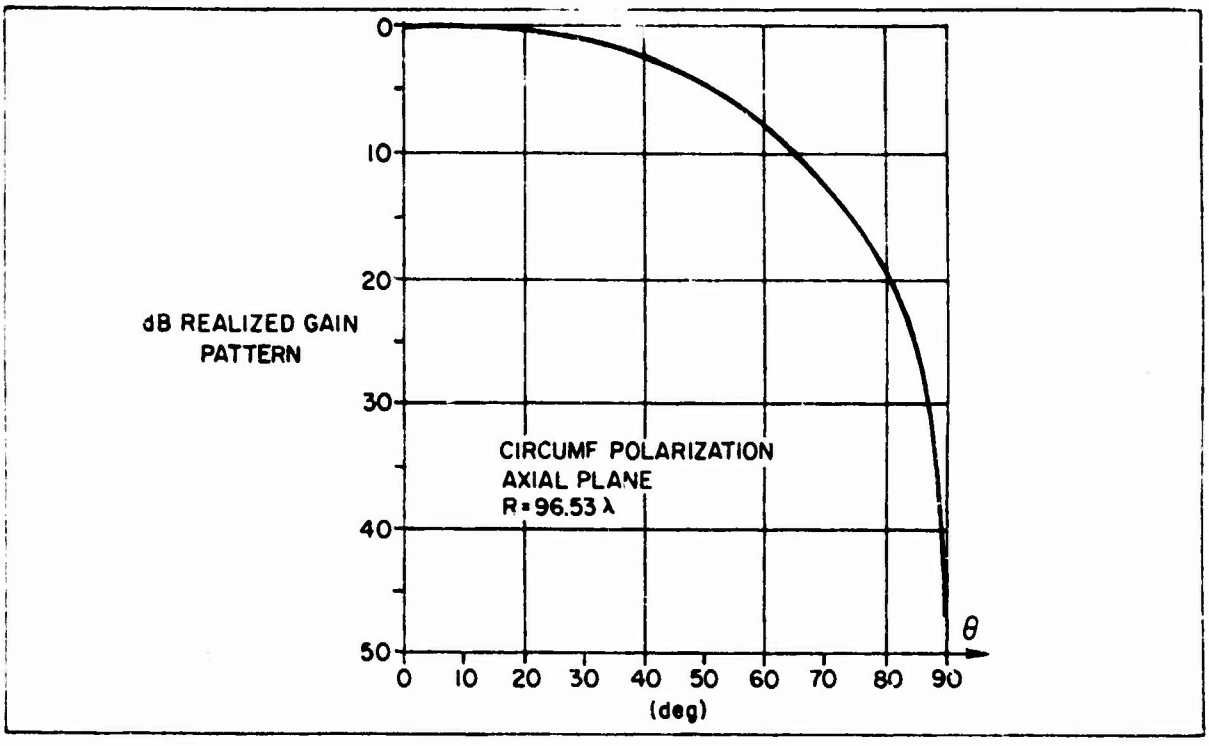

Figure 9 - Element Gain for Axial Polarization

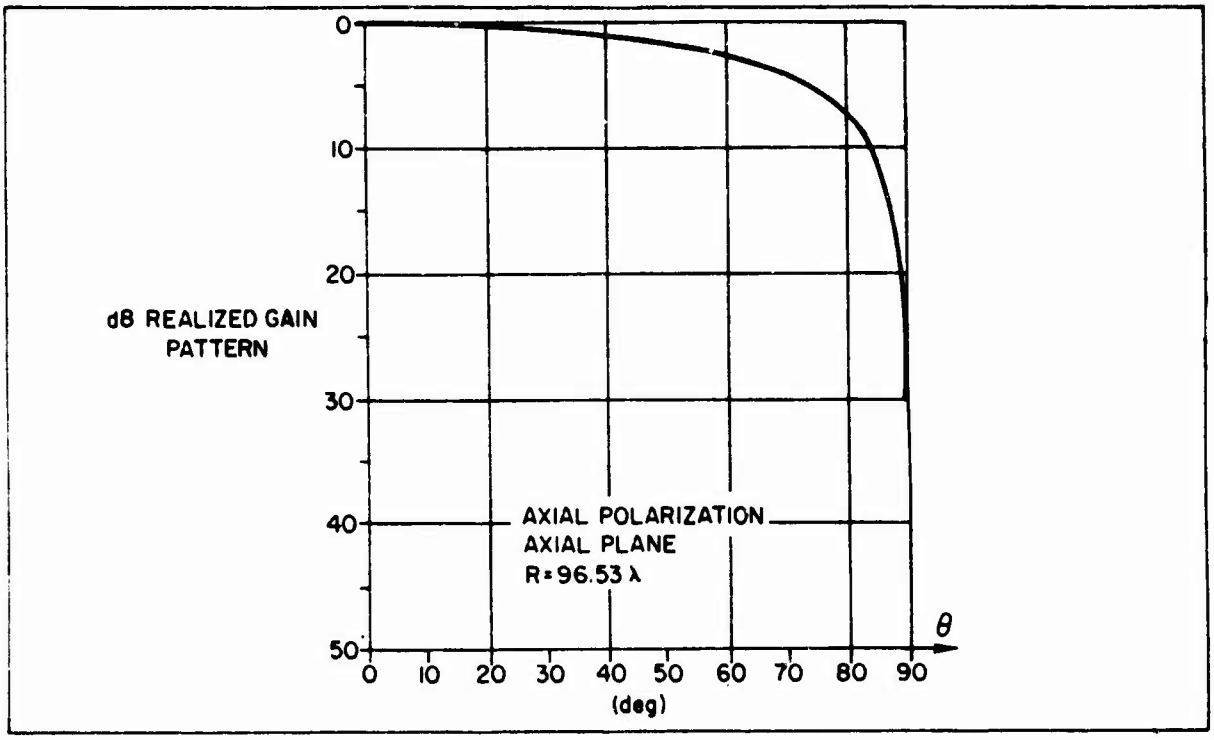

Figure 10 - Element Gain for Circumferential Polarization

Finally the isolated element pattern has been computed with the "one mode" approximation. Figure 11 and 12 show the isolated element pattern in the circumferential plane for axial and circumferential polarization. As expected, the patterns show a smooth variation versus angular direction.

2.6 An Asymptotic Model for Small Arrays on Cylinders of Large Radius

The analysis of finite arrays of waveguide elements on dielectric clad cylinders of large radius can be rather easily derived from the theory of this section. However, since the mutual admittances between elements in a finite cylindrical array are expressed as series of integrals of the type in Equations (1) - (12) [16], the effort required to numerically evaluate the driving point admittance of the array elements is much greater than in the case of the infinite periodic structure, even if asymptotic expansions of Hankel functions are used in the computations.

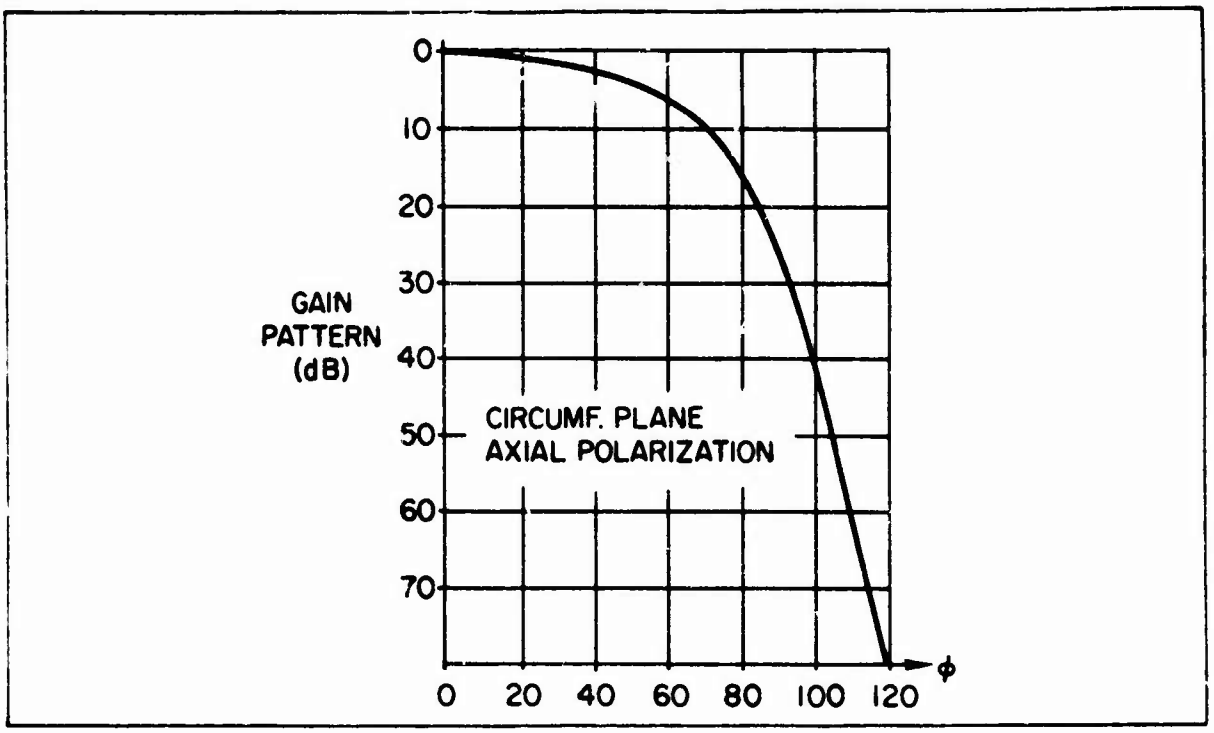

Figure 11 - Isolated Element Pattern

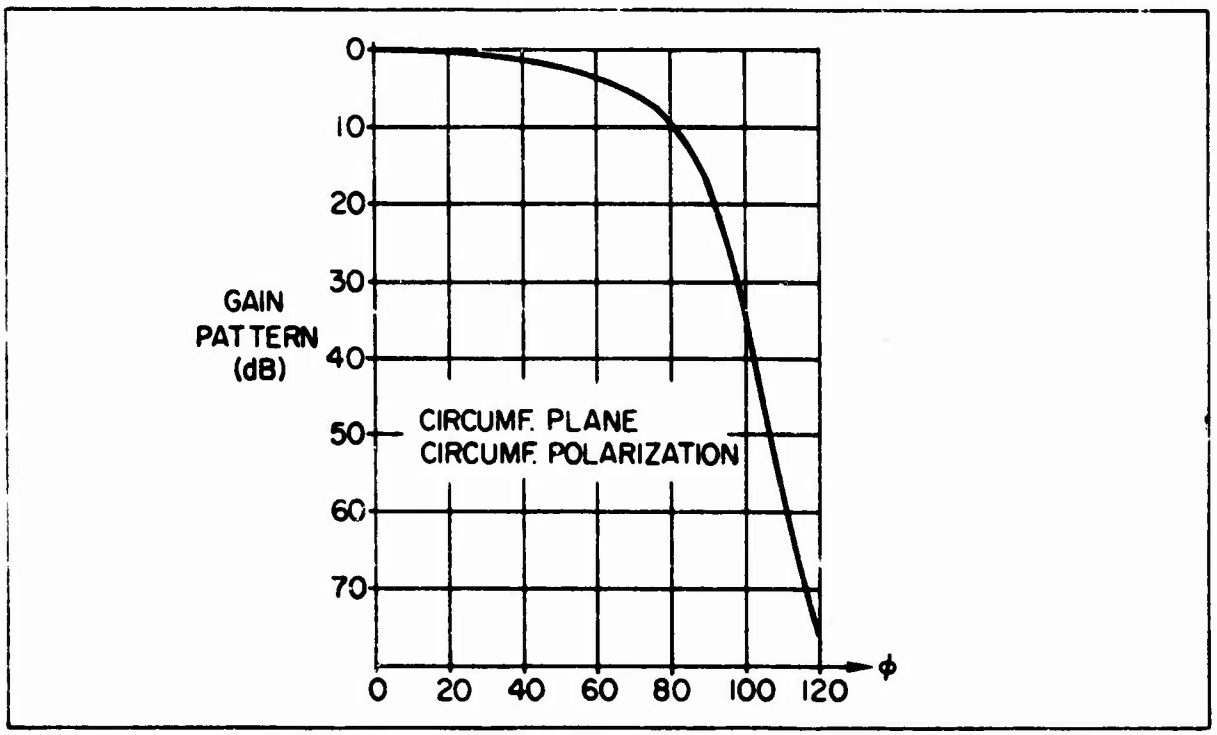

Figure 12 - Isolated Element Pattern

In this condition it is convenient to use an asymptotic model for finite arrays on cylinders of large radius. The numerical results of this section show that there are only small differences between the driving point admittance and the radiation pattern of an element in an infinite periodic cylindrical array of large radius covered by dielectric and the corresponding planar case. The close similarity of the results obtained by using the planar and the cylindrical array models suggests that a planar array model can be employed with excellent approximation in predicting the coverage performance of a finite array extending only over a limited circumferential and axial sector of a large cylinder. The aperture of the arrays considered in this study (aperture gain 20-30 dBi) extends only a few degrees (2 to 10) over the circumferential direction of a cylinder with 100λ radius. In these conditions the mutual coupling between elements, which determines the aperture driving point admittance, practically takes place in a planar environment, so a planar array model should give an excellent approximation.

In predicting element pattern performance the planar model gives consistently lower levels of endfire radiation in the circumferential plane than the cylindrical model, while no difference is present in the axial plane. So if hemispheric scan coverage from a finite array on a large cylinder is predicted by using a planar model the array is bound to exhibit even better coverage performance than predicted, at least in the circumferential plane. On the basis of these considerations and the numerical results previously shown, the coverage of finite arrays covered by a dielectric sheet on cylinders of large radius has been analyzed by using a planar array model. The analysis of finite planar arrays is presented in the next section.

3. FINITE ARRAYS IN AN INFINITE GROUND PLANE COVERED BY A DIELECTRIC

3.1 General Remarks

The analysis of finite arrays in an infinite ground plane has been performed by various authors. The element pattern due to the limited extent of the array dimensions has been clearly illustrated for arrays of parallel plate waveguides [17-18]. More recently the mutual coupling between elements in finite arrays of circular waveguides has been presented and compared with the infinite array case [19-20].

The basic approach to the analysis of finite arrays of waveguides in an infinite ground plane consists in formulating an integral equation in the unknown amplitude of the magnetic field at each aperture. The integral equation can be solved by straight forward application of Galerkin's method. This procedure leads to a system of equations of the order M x N, where N is the number of array elements and M is the number of feedguide modes used to enforce the continuity of electric and magnetic fields at the aperture discontinuity. As the number of array elements and of waveguide modes used in field matching increases, one is faced with the inversion of large matrices. This operation is computer time consuming and poses serious limitations on the number of elements in the arrays which can be analyzed.

The approach taken here for the analysis of finite arrays of waveguide elements in an infinite ground plane covered by a dielectric sheet is based on the formulation of an integral equation in the unknown magnetic fields at the element apertures. However, no inversion of large matrices is performed in evaluating the mutual coupling between elements.

The matrix inversion operation is avoided by exploiting the symmetries in the array geometry in constructing the array scattering matrix. Only the mutual coupling coefficients for a selected number of array elements is evaluated. This requires the solution of a system of equations, an operation which can be performed by a computer at a much higher speed than matrix inversion.

3.2 Network Model of Finite Arrays

In this subsection some general properties of finite arrays of waveguide apertures in an infinite ground plane, which may be covered by an infinite sheet of dielectric, will be discussed. The array apertures are of arbitrary shape and are fed by uniform waveguides of the same cross section. The array lattice can be arbitrarily defined and need not be regular.

It is convenient to represent the array-free space interface by a multiport network [21], as shown in Figure 13a. Each element consists of an M port unit (M is the number of waveguide modes used in enforcing the continuity of the tangential fields at the array-free-space interface); therefore an array of N waveguide elements can be represented by an M x N port network. Only "free" excitations of this M x N port network will be considered, that is sets of waves incident to the element inputs ports. Let the excitations of the array be represented by N x M dimensional column vector $\underline{a}$. The set of reflected waves at all ports is similarily represented by a N x M dimensional vector $\underline{b}$. The incident and reflected waves are related by the scattering matrix $\underline{\underline{S}}$ of the network:

$$\underline{b} = \underline{\underline{S}}\,\underline{a} \tag{31}$$

The scattering matrix $\underline{\underline{S}}$ completely characterizes the network. Any particular property of $\underline{\underline{S}}$ should be used in the analysis of the array and vice versa. This approach has been followed in the theory of planar and cylindrical infinite periodic arrays, where the symmetry of the structures can be exploited for an immediate evaluation of the eigenvectors and the diagonalization of $\underline{\underline{S}}$ (the eigenexcitation method [1-15]).

In the case of an arbitrary finite array the scattering matrix $\underline{\underline{S}}$ does not present any particular property that can immediately lead to its diagonalization. In other words, for finite arrays there is no simple way to determine the eigenexcitations of the structure, which are those sets of incident waves exciting the same transverse electric field distribution at all array apertures except for a progressive phase term. It has been shown [17] that for "large" arrays of regular lattice it is possible to approximate the finite array eigenexcitations through a perturbation of the eigenexcitations

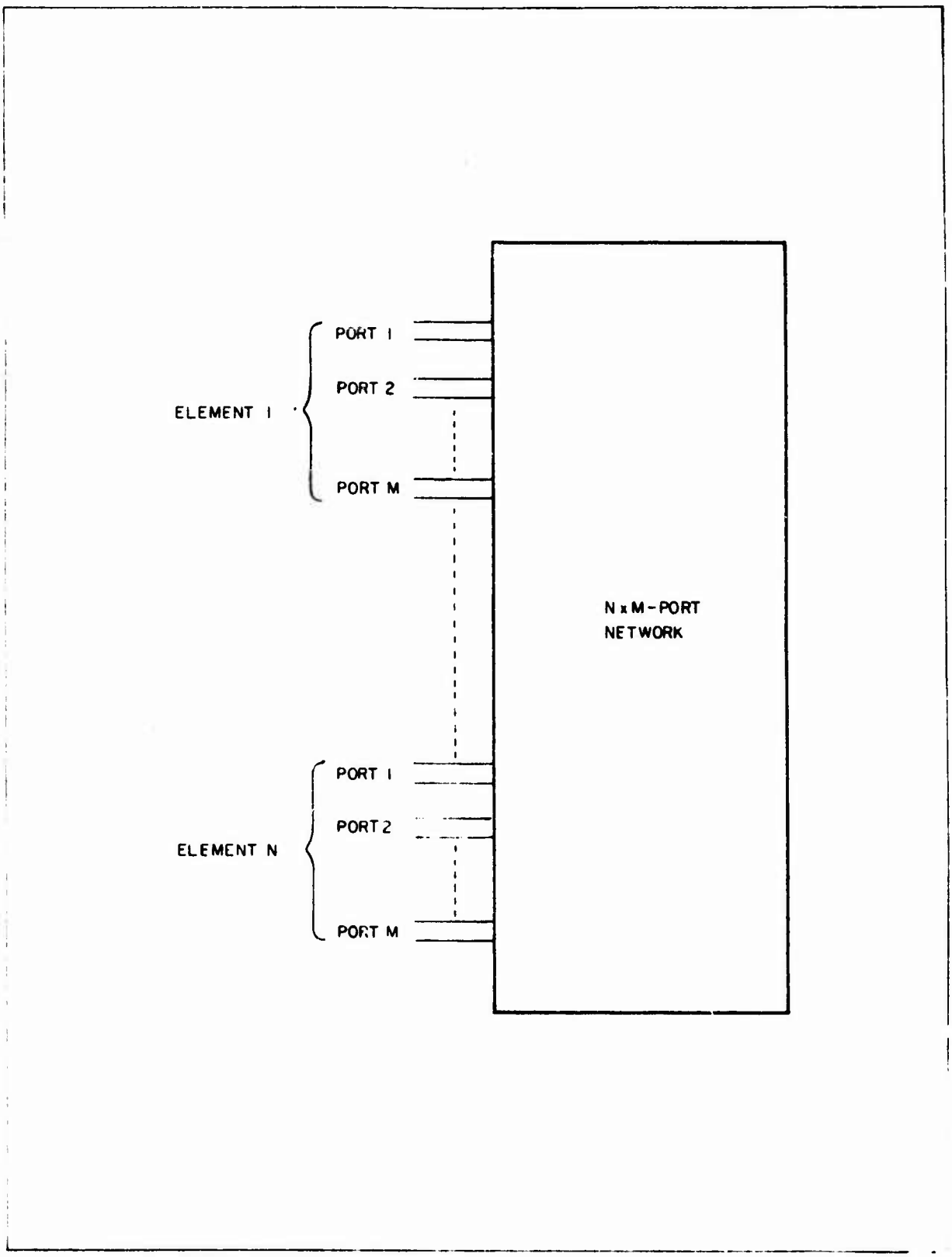

Figure 13a - Network Representation of Array-Free Space Interface

of the infinite periodic structure. This procedure cannot be applied to arrays of arbitrary lattice because the perturbation method does not converge to the solution. The only way to determine the eigenexcitations of an arbitrary finite array is to actually solve (by numerical methods) the characteristic equation of the scattering matrix. This approach presents substantial computational difficulties as the number of array elements increased, more over the eigenexcitations may not be orthogonal.

There is a convenient method to determine the scattering matrix of a finite array. It is well known [22] that the scattering matrix of a network can be obtained from the admittance matrix $\underline{\underline{Y}}$ relating port voltages to port currents. The following matrix relationship holds:

$$\underline{\underline{S}} = (Y_g \underline{\underline{U}} - \underline{\underline{Y}})\ (Y_g \underline{\underline{U}} + \underline{\underline{Y}})^{-1} \tag{32}$$

where $\underline{\underline{U}}$ is a unit matrix of the same order as $\underline{\underline{Y}}$. The elements of the $\underline{\underline{Y}}$ matrix can be grouped in submatrices relative to the ports of each array element in the following fashion:

$$\underline{\underline{Y}} = \begin{bmatrix} \underline{\underline{Y}}_{11} & \underline{\underline{Y}}_{12} \cdots \underline{\underline{Y}}_{1N} \\ \underline{\underline{Y}}_{21} & \underline{\underline{Y}}_{22} \cdots \underline{\underline{Y}}_{2N} \\ \vdots & \vdots \quad \vdots \\ \underline{\underline{Y}}_{N1} & \underline{\underline{Y}}_{N2} \cdots \underline{\underline{Y}}_{NN} \end{bmatrix}$$

where $\underline{\underline{Y}}_{pq}$ are square matrices of the M order. $\underline{\underline{Y}}_{pq}$ represents the mutual admittance between the M ports of element p with the M ports of element q. The elements of Y_{pq} can be determined only by solving the boundary condition problem at the array aperture. This will be done in the next section. For the moment suppose that the $\underline{\underline{Y}}$ matrix is known, then the operations in Equation (32) can be performed. The inversion of the augmented matrix $\underline{\underline{Y}}$ would produce more information about the network than is needed to

determine the radiation properties of the array. For this purpose, only the columns of $\underline{\underline{S}}$ relative to the actively excited ports are required; the other columns of $\underline{\underline{S}}$, corresponding to passively excited ports, do not need to be determined. This fact can be exploited to reduce the computations required in the analysis of a small array. Equation (32) can be viewed as a system of equations in the unknown columns $\underline{X}$ of $\underline{\underline{S}}$ by writing:

$$(Y_g \underline{\underline{U}} + \underline{\underline{Y}}) \underline{X} = \underline{E} \tag{33}$$

where $\underline{E}$ is a column of $\underline{\underline{Y}}_g \underline{\underline{U}} - \underline{\underline{Y}}$.

The system of equations (33) can be repeatedly solved only for those excitations (columns of $Y_g \underline{\underline{U}} - \underline{\underline{Y}}$) corresponding to the actively excited ports of the network. In these conditions only N columns of the N x M order $\underline{\underline{S}}$ matrix are obtained, forming a matrix $\underline{\underline{S}}^N$. However, the rectangular $\underline{\underline{S}}^N$ matrix is sufficient to characterize the radiation property of the array, since the product between $\underline{\underline{S}}^N$ and an N dimensional excitation column vector $\underline{a}^N$, whose components are the incident waves at the active ports, gives the reflection coefficients at the active ports and the excitation of higher order waveguide modes. This procedure involves much less computations than the inversion of the matrix $(Y_g \underline{\underline{U}} + \underline{\underline{Y}})$ and substantial computer time is saved for a given array size. Moreover, any symmetry in the array structure, for example quadrantal symmetry, can be easily exploited in reducing the number of excitations for which systems of Equation (33) is solved. This approach is rigorously valid only for open ended uniform waveguides and is not correct if a matching network is present in the element feedguides. An extension of this approach to the case of radiating elements backed by a matching network will be discussed in a latter section.

3.3 Boundary Condition Problem for Finite Arrays in an Infinite Ground Plane Covered by Dielectric

The array geometry is conveniently established by the means of a set of vectors $\underline{\underline{s}}_n$, representing the position of the elements as shown in Figure 13b. The N array elements are arbitrary apertures fed by

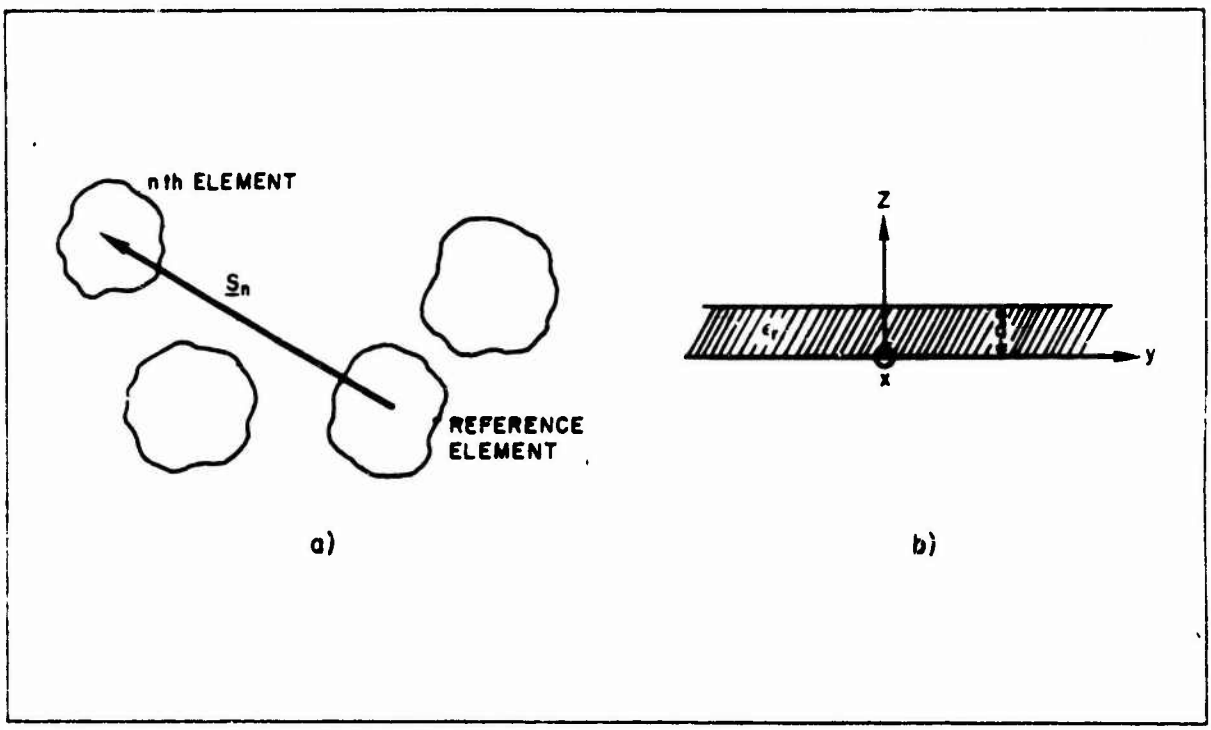

Figure 13b - Array and Dielectric Geometry

waveguides of the same cross section. Only one mode is assumed to be propagating in the waveguide elements. The transverse modal function for the propagating mode in the nth feedguide is denoted by $e^n{}_1(\underline{s})$, the higher order modes $e^n{}_m(\underline{s})$ are ordered by increasing cutoff frequency. The dielectric layer covering the array has a thickness d, a relative dielectric constant ϵ_r, propagation constant k_d and a characteristic impedance η_d. Assume that the mode $e^n{}_1(\underline{s})$ is actively excited in some array elements. Then the tangential electric field at the array apertures can be expressed as a superposition of waveguide modes:

$$\underline{E}_t^-(\underline{s}) = \sum_{n=1}^{N} \sum_{m=1}^{M} \left(\delta^n{}_{1,m} + \Gamma^n{}_m \right) \underline{e}^n m (\underline{s} - \underline{s}_n) \tag{34}$$

where $\delta^n{}_{1,m}$ is equal zero in the passively excited elements, while for the actively excited elements

$$\delta^{n}_{1,m} = \begin{cases} 1 \text{ for } m = 1 \\ 0 \text{ for } m \neq 1 \end{cases}$$

In Equation (34) Γ^{n}_{m} represents the amplitude of the modes passively excited at the aperture of the nth element. If the nth element is actively excited, Γ^{n}_{1} represents the active reflection coefficient of the $e^{n}_{1}(\underline{s})$ mode.

The external tangential electric field can be represented as a superposition of TM and TE waves [18]:

$$\underline{E}^{+}_{t} = \frac{1}{2\pi} \iint_{-\infty}^{+\infty} [\, \underline{\mathcal{E}}_{\rho}(\underline{u}) + \underline{\mathcal{E}}_{\psi}(\underline{u}) \,] \, e^{-j\underline{u}\underline{s}} \, d\underline{u} \tag{35}$$

Enforcing the continuity between Equation (35) and Equation (34) the following relations are obtained:

$$\mathcal{E}_{\rho}(\underline{u}) = \sum_{n=1}^{N} \sum_{m=1}^{M} (\delta^{n}_{1,m} + \Gamma^{n}_{m}) \, \mathcal{E}^{n}_{\rho m}(\underline{u}) \, e^{j\underline{u}\underline{s}_{n}} \tag{35a}$$

$$\mathcal{E}_{\psi}(\underline{u}) = \sum_{n=1}^{N} \sum_{m=1}^{M} (\delta^{n}_{1,m} + \Gamma^{n}_{m}) \, \mathcal{E}^{n}_{\psi m}(\underline{u}) \, e^{j\underline{u}\underline{s}_{n}} \tag{35b}$$

In Equations (35a) and (35b) $\mathcal{E}^{n}_{\rho m}(\underline{u})$ and $\mathcal{E}^{n}_{\psi m}(\underline{u})$ are the components of the Fourier Transform of the mth waveguide mode defined as [23]:

$$\underline{\mathcal{E}}^{n}_{m}(\underline{u}) = \frac{1}{2\pi} \iint_{A_n} \underline{e}^{n}_{m}(\underline{s}) \, e^{j\underline{u}\underline{s}} \, d\underline{s}$$

where the integral is extended over the nth aperture.

The magnetic field at the waveguide apertures is given by:

$$\underline{H}^{-}_{t}(\underline{s}) = \hat{z} \times \sum_{n=1}^{N} \sum_{m=1}^{M} \left(\delta^{n}_{1,m} - \Gamma^{n}_{m} \right) Y^{n}_{m} \, \underline{e}^{n}_{m}(\underline{s} - \underline{s}_{n}) \tag{36}$$

In Equation (36) $\delta^{n}_{l,m}$ and Γ^{n}_{m} have the same definition as in Equation (34), Y^{n}_{m} is the characteristic waveguide admittance of the mth mode in the nth feedguide and $\hat{\underline{z}}$ is a unit vector in the direction of the external normal to the array. The external Magnetic field is expressed by a superposition of TE and TM waves:

$$\underline{H}^{+}_{t}(\underline{s}) = \frac{1}{2\pi}\iint_{-\infty}^{+\infty}\left[\hat{\rho}\mathcal{E}_{\psi}(\underline{u})\,\frac{w_d}{k_d\eta_d}\,F^{TE}(|u|) + \hat{\psi}\mathcal{E}_{\rho}(\underline{u})\,\frac{k_d}{w_d\eta_d}\,F^{TM}(|u|)\right] e^{-j\,\underline{u}\,\underline{s}}\,d\underline{u} \tag{37}$$

In Equation (37)

$$w_d = \sqrt{k_d^2 - |\underline{u}|^2}$$

for

$$|\underline{u}|^2 \leq k_d^2$$

and

$$w_d = -j\sqrt{|\underline{u}|^2 - k_d^2}$$

for

$$|\underline{u}|^2 \geq k_d^2.$$

$F^{TE}(|u|)$ and $F^{TM}(|u|)$ are defined as:

$$F^{TE}(|u|) = -\frac{Y^{TE}(|u|)\cos w_d d + j\,Y_d^{TE}(|u|)\sin w_d d}{Y_d^{TE}(|\underline{u}|)\cos w_d d + j\,Y^{TE}(|\underline{u}|)\sin w_d d} \tag{38}$$

$$F^{TM}(|u|) = \frac{Y^{TM}(|u|)\cos w_d d + j\, Y_d^{TM}(|u|)\sin w_d d}{Y_d^{TM}(|u|)\cos w_d d + j\, Y^{TM}(|u|)\sin w_d d} \tag{39}$$

where $Y_d^{TE}(|u|)$, $Y^{TE}(|u|)$, $Y_d^{TM}(|u|)$ and $Y^{TM}(|u|)$ are given in [7]. The quality between Equations (36) and (37) can be enforced by a straightforward application of Galerkin's method. By requiring that the difference between Equation (36) and Equation (37) has zero projection on the subspace spanned by $z \times e_n^k (\underline{s} - \underline{s}_k)$, the following systems of equations is obtained (Appendix C):

$$\left(\delta^k_{l,h} - \Gamma^k_h\right) Y^k_h = \sum_{n=1}^{N} \sum_{m=1}^{M} Y^{nk}_{mh} \left(\delta^k_{l,h} + \Gamma^n_m\right) \tag{40}$$

$$(k = 1, \ldots N;\ h = 1, \ldots M)$$

In Equation (40) Y^{nk}_{mh} expresses the mutual admittance between the mth mode of the nth element and the hth mode of the kth element. The expression of Y^{nk}_{mh} is given in Appendix C. It is easy to recognize that the system of Equation (40) can be cast in the form of Equations (32) or (33).

3.4 Arrays of Uniform Circular Apertures

In the preceding sections a general theory for arbitrary finite array of open ended feedguides covered by dielectric has been developed. It has been shown that for uniform waveguides there is no need to determine the complete scattering matrix for the array in order to evaluate its radiation properties. Let us now take into consideration arrays of apertures that can provide hemispheric scan coverage. For this particular application a circularly polarized element is required; so circular or square apertures are a natural choice. In the following we will deal with circular feedguide arrays. However, with minor changes the same considerations apply to arrays of square feedguides. In practi-

an array of circular waveguide apertures will be rather poorly matched to free space. The dielectric sheet covering the array can provide some matching, but, in general, a matching network will be required in each feedguide to avoid large reflections at the array aperture. We assume that the same network is present in all elements. In these conditions the procedure to obtain the array scattering matrix presented in the previous sections ceases to be valid, because higher order modes may be incident at the aperture. We will show now that the procedure remains perfectly valid if applied to an admittance matrix properly augumented to take into account the presence of a lossless matching network.

Let us call $\underline{e}_1(\underline{s})$ and $\underline{e}_2(\underline{s})$ the two orthogonal propagating TE_{11} modes. All higher order modes $e_m(\underline{s})$ are below cut off. M - 2 higher order modes are used to match the tangential electric and magnetic field at the array aperture. On the basis of considerations of the preceding sections, if no matching network is present, the aperture discontinuity can be represented as a N x M port network characterized by the admittance matrix $\underline{\underline{Y}}$ relating aperture currents and voltages for each mode as given by Equation (40):

$$\underline{I} = \underline{\underline{Y}}\,\underline{V} \tag{41}$$

If a lossless matching network is introduced in the element feedguides, the new aperture modal voltages must be determined to evaluate the array radiation. In addition the reflection coefficient in the generator lines must be determined for the actively excited modes. The matching network, which is the same for all TE_{11} mode ports, can be represented in terms of a shunt susceptance and an ideal transformer. For the higher order modes we suppose that the matching network provides a reactive termination, which can be represented by a lumped susceptance as seen at the element aperture. The equivalent network of the array aperture and the matching network in the elements is shown in Figure 14 where the admittance of the generator lines for the TE_{11} modes is called Y_g and port 1 of element i is actively excited. The reflection coefficient at port 1 of element i is called V^i_{g1}.

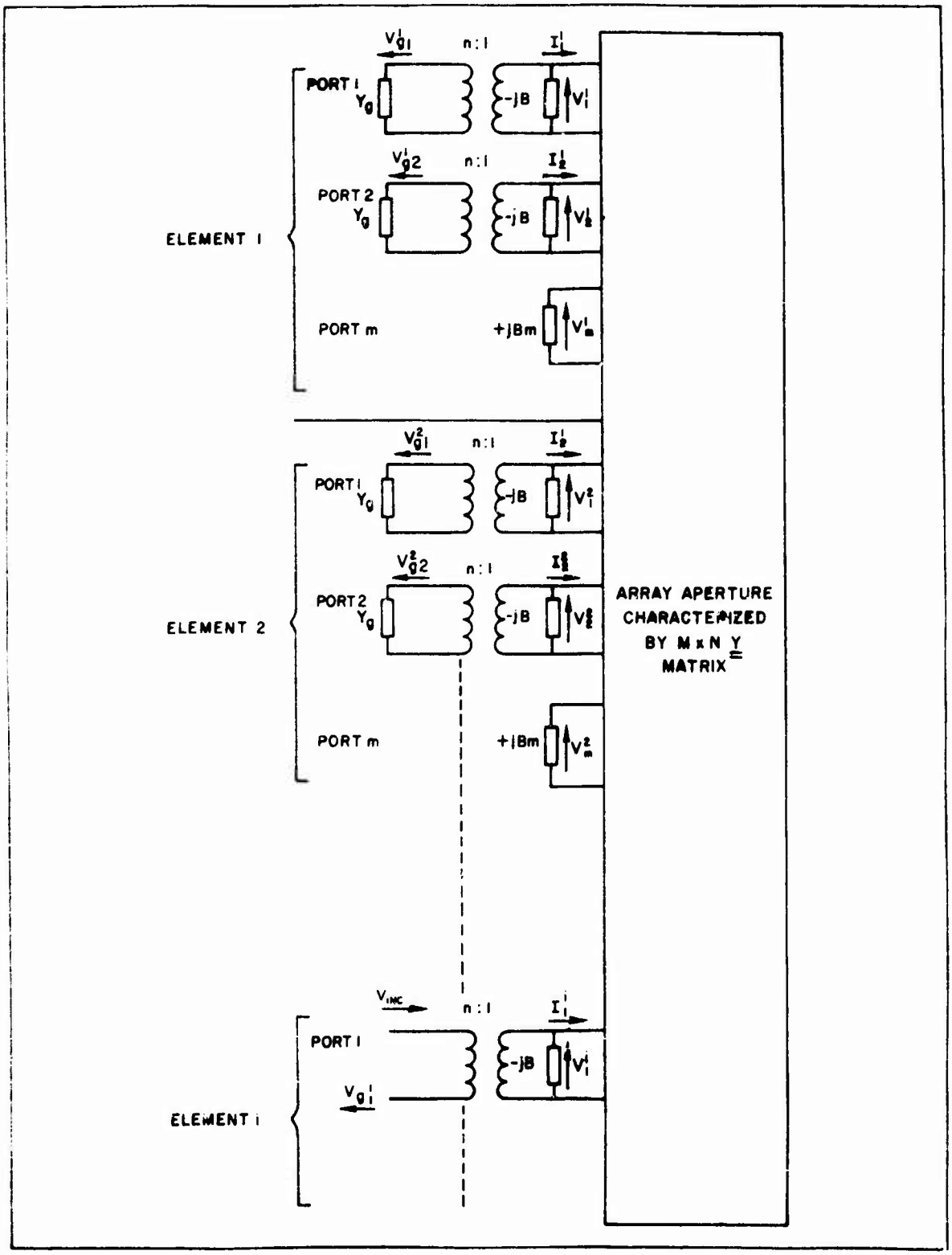

Figure 14 - Finite Array Equivalent Network

A relation identical to Equation (41) is still valid for aperture currents and voltage. Let us express the aperture voltages in terms of the voltages in the generator lines for the TE_{11} ports.

Writing Equation (41) more explicity we have:

$$\begin{pmatrix} \underline{I}_1 \\ \underline{I}_2 \\ \cdot \\ \cdot \\ \cdot \\ \cdot \\ \underline{I}_N \end{pmatrix} = \begin{pmatrix} \underline{\underline{Y}}_{11} & \underline{\underline{Y}}_{12} & \cdots\cdots & \underline{\underline{Y}}_{1N} \\ \underline{\underline{Y}}_{21} & \underline{\underline{Y}}_{22} & \cdots\cdots & \underline{\underline{Y}}_{2N} \\ & & & \\ & & & \\ \underline{\underline{Y}}_{N1} & \underline{\underline{Y}}_{N2} & \cdots\cdots & \underline{\underline{Y}}_{NN} \end{pmatrix} \begin{pmatrix} \underline{V}_1 \\ \underline{V}_2 \\ \cdot \\ \cdot \\ \cdot \\ \cdot \\ \underline{V}_N \end{pmatrix} \tag{42}$$

where

$$\underline{V}_k = \begin{pmatrix} V_1^k \\ V_2^k \\ \cdot \\ \cdot \\ \cdot \\ V_M^k \end{pmatrix} \quad \text{and} \quad \underline{I}_k = \begin{pmatrix} I_1^k \\ I_2^k \\ \cdot \\ \cdot \\ \cdot \\ I_M^k \end{pmatrix}$$

At the actively excited TE_{11} port we have:

$$V_1^i = \frac{1 + V_{g1}^i}{n} V_{inc}; \; I_1^i = \frac{1}{n}\Big[\left(1 - V_{g1}^i\right) n^2 Y_g + jB \left(1 + V_{g1}^i\right)\Big] V_{inc} \tag{43}$$

For the passively excited TE_{11} ports the following relations hold:

$$V_r^k = \frac{V_{gr}^k}{n} \quad (r = 1, 2); \; I_r^k = -\frac{1}{n} \left(n^2 Y_g - jB\right) V_{gr}^k \tag{44}$$

For all other ports we simply have:

$$I_m^k = -jB_m V_m^k \tag{45}$$

Let us call $n^2 Y_g = G$, then, by inserting relations (43) - (45) in (42), the following set of equations is obtained:

$$\underline{\underline{E}} = (\underline{\underline{Y}} + \underline{\underline{Y}}_T)\,\underline{\underline{\Gamma}} \tag{46}$$

In Equation (46) E is a N x M dimensional column vector representing the excitation. The components of $\underline{\underline{E}}$ are obtained by multiplying the $(M \times i + 1)$th column of the matrix $\underline{\underline{Y}}$ by $-\frac{V_{inc}}{n}$ except for the $(M \times i + 1)$th component which is given by:

$$\frac{V_{inc}}{n} \left[G + jB - Y_{11}^{ii}\right]$$

The N x M dimensional vector $\underline{\underline{\Gamma}}$ of Equation (46) represents the array "response" to the excitation of port 1 of element i. The components of $\underline{\underline{\Gamma}}$ are the total aperture voltages of the below cut-off modes (V_m^k), the aperture passive excitation of TE_{11} ports (V_{gr}^k/n) and, for the active port, a voltage (V_{g1}^i/n) which is directly related to the active reflection coefficient in the generator line. The matrix $\underline{\underline{Y}}_T$ in Equation (46) is a diagonal matrix formed by the admittances terminating the ports ($G - jB$ or jB_m).

The systems of Equation (46) can be repeatedly solved for all the TE_{11} ports of the network, thus constructing a rectangular matrix $\underline{\underline{S}}$ of M x N rows and 2N columns. The product between $\underline{\underline{S}}$ and a 2N dimensional column vector, representing the excitation of the TE_{11} ports, gives the "response" of the array to a general excitation. The advantage of this procedure consists in the fact that any array symmetry can be easily exploited in reducing the number of excitations in Equation (46). The substantial savings in terms of computer time as compared to the inversion of $(\underline{\underline{Y}} + \underline{\underline{Y}}_T)$ will be illustrated in a later section.

3.5 Radiation of Finite Arrays of Circular Waveguides in Infinite Ground Plane Covered by Dielectric

The TE and TM components of the electric field from a finite array in an infinite ground plane can be found by applying simple transmission line considerations to Equation (35). It can be simply shown [24] that for any point $z \geqslant d$ (d = thickness of dielectric layer) the TE and TM components of the electric field are given by:

$$\vec{E}(x, y, z) = \frac{1}{2\pi} \iint_{-\infty}^{+\infty} \left[\underline{\mathcal{E}}_\rho(\underline{u}) \frac{Y_d^{TM}(|\underline{u}|)}{Y_d^{TM}(|u|)\cos w_d d + jY_d^{TM}(|u|)\sin w_d d} \right.$$

$$\left. + \underline{\mathcal{E}}_\psi(\underline{u}) \frac{Y_d^{TE}(|\underline{u}|)}{Y_d^{TE}(|\underline{u}|)\cos w_d d + jY_d^{TE}(|\underline{u}|)\sin w_d d} \right] \cdot \quad (47)$$

$$e^{-jw(z-d)} e^{-j\underline{u}\cdot\underline{x}} du$$

All notations in Equation (47) are as established in previous sections. The integrals in Equation (47) can be evaluated asymptotically for far field computation. To this purpose, it is convenient to introduce the following change of variables:

$$u = t\cos\mu \qquad x = r\sin\theta\cos\phi$$

$$v = t\sin\mu \qquad y = r\sin\theta\sin\phi$$

$$w = \sqrt{k^2 - t^2} \qquad z - d = r\cos\theta$$

then Equation (47) becomes:

$$\vec{E}(r,\theta,\phi) = \frac{1}{2\pi}\int_0^{2\pi}\int_0^{\infty}[\underline{\mathcal{E}}_{\rho}(t,\mu)\,P^{TM}(t) + \underline{\mathcal{E}}_{\psi}(t,\mu)\,P^{TE}(t)]\cdot \tag{48}$$

$$e^{-jr\cos\theta\sqrt{k^2 - t^2}}\, e^{-jtr\sin\theta\cos(\phi-\mu)}\, t\,dt\,d\mu$$

where $P^{TM}(t)$ and $P^{TE}(t)$ are defined by comparison with Equation (47). The asymptotic evaluation of Equation (48) does not present any particular difficulty as well known methods are available in the literature [25-26]. In Appendix D the the asymptotic evaluation of Equation (48) is treated with some detail for the fundamental TE_{11} mode. The same procedure can be applied to higher order modes with analogous results. For the far TM component of the field of the TE_{11} mode of a single slot we have:

$$\lim_{r\to\infty} E_{\rho}(r,\theta,\phi) = \frac{A}{2}\frac{e^{-jkr}}{r}\sin\phi\; k\cos\theta\,\frac{J_1(ak\sin\theta)}{k\sin\theta}\,P^{TM}(k\sin\theta) \tag{48 a}$$

and for the TE component:

$$\lim_{r\to\infty} E_{\psi}(r,\theta,\phi) = \frac{A}{2}\frac{e^{-jkr}}{r}\cos\phi\cos\theta\,\frac{ka\,J_1'(ak\sin\theta)}{1 - \left(\frac{k\,a\sin\theta}{x'_{11}}\right)^2}\,P^{TE}(k\sin\theta) \tag{48 b}$$

For the definition of A, a, k, J_1 and J_1' see appendix D.

There is, in addition, the contribution from the poles of $P^{TE}(t)$ and $P^{TM}(t)$. If we suppose that only a $P^{TM}(t)$ pole exists for the given value of d and ϵ_r of the dielectric covering the array, the residue contribution is given by:

$$\text{Res} = -j\pi A \sin\phi\, J_1(at_p) \sqrt{\frac{2j}{\pi r t_p \sin\theta}}\, \frac{NP^{TM}(tp)}{\frac{d}{dt} DP^{TM}(t)\Big|_{t=t_p}} \cdot e^{-jr\left(t_p \sin\theta - j\cos\theta \sqrt{t_p^2 - k^2}\right)} \tag{49}$$

where t_p is the pole of $P^{TM}(t)$, $NP^{TM}(t)$ and $DP^{TM}(t)$ stand for numerator and denominator of $P^{TM}(t)$, respectively. It is worth noticing that Equation (49) does not contribute to the radiated far field of the slot.

It is convenient to express the radiated far electric field in terms of the θ and ϕ components of the reference (r, θ, ϕ) used is the integral (48). The θ and ϕ components of the far field are simply related to E_ρ and E_ψ:

$$E_\theta(r, \theta, \phi) = E_\rho(r, \theta, \phi)/\cos\theta$$

$$E_\phi(r, \theta, \phi) = E_\psi(r, \theta, \phi)$$

Let us call $\vec{P}_1(\theta, \phi)$ the pattern relative to the TE_{11} mode considered

$$\vec{P}_1(\theta, \phi) = \frac{e^{-jkr}}{r} \left[\hat{\theta} E_\theta(r, \theta, \phi) + \hat{\varphi} E_\phi(r, \theta, \phi)\right]$$

The patterns $\vec{P}_i(\theta, \phi)$ relative to other modes can be obtained in an analogous manner. Then the array pattern is given simply by:

$$\vec{P}(\theta, \phi) = \sum_{m=1}^{M} \left(\sum_{n=1}^{N} V^n{}_m e^{j\underline{u}\,\underline{s}_n} \right) \vec{P}_m(\theta, \phi) \tag{50}$$

where V^n_m is the total voltage of the mode m on the nth aperture. Equation (50) is obtained by simple manipulation of Equation (48), considering the definition given for $\mathcal{E}_\rho$ and $\mathcal{E}_\psi$ in Equations (35a) and (35b).

3.6 Gain of Finite Arrays

The realized gain of small arrays must be evaluated by the means of the elementary definition of gain, since it is not possible to determine the element area gain as in infinite periodic array theory [27].

The realized gain of an array in the direction (θ_o, ϕ_o) of the spherical coordinate reference used to evaluate the far field (Equation (48)) is given by:

$$G(\theta_o, \phi_o) = \frac{\text{Power Density at } (\theta_o, \phi_o)}{\text{Maximum Power Density Available Isotropically}} \tag{51}$$

As the far field intensity $\vec{E}(\theta_o, \phi_o)$ in the direction (ϑ_o, ϕ_o) can be evaluated, Equation (51) can be written as:

$$G(\theta_o, \phi_o) = \frac{\left|\vec{E}(\theta_o, \phi_o)\right|^2/\eta}{P_{MAX}/4\pi r^2} \tag{52}$$

Where η is the free space impedance and P_{MAX} is the maximum power available in the generator lines. By recalling the definition of Equation (50), we have that:

$$r^2\left|\vec{E}(\theta_o, \varphi_o)\right|^2 = \left|\sum_{m=1}^{M}\left(\sum_{n=1}^{N} V^n_m e^{j\underline{u}_o \underline{s}_n}\right)\vec{P}_m(\theta_o, \phi_o)\right|^2 \tag{53}$$

The maximum power available, if N_e elements are actively excited, is given by:

$$P_{MAX} = Y_g \sum_{i=1}^{N_e} |V_{gi}|^2 \tag{54}$$

Where Y_g is the characteristic admittance of the propagating feedguide mode and V_{gi} is the feedguide modal voltage incident from the generators (Figure 14).

Inserting Equations (53) and (54) in Equation (52), the gain equation for finite arrays is given by:

$$G(\theta_o, \phi_o) = \frac{4\pi \left| \sum_{m=1}^{M} \left(\sum_{n=1}^{N} V_m^n \, e^{j \underline{u}_o \underline{s}_n} \right) \vec{P}_m(\theta_o, \phi_o) \right|^2}{Y_g \sum_{i=1}^{Ne} |V_{gi}|^2} \qquad (55)$$

It is important to note that the aperture field matching using Galerkin's method, performed to determine the amplitudes of the array element modal voltages, conserves power, as can be easily checked from Equations (36) and (37). Thus gain expression (55) automatically takes into account any reflection losses.

Equations (50) and (55) can be used to determine the array radiation properties for any arbitrary excitation. In particular they can be used to evaluate the gain and the pattern of an element in the array environment.

3.7 Element Pattern and Gain in a Finite Array of Apertures in an Infinite Ground Plane Covered by Dielectric

The planar model developed in the previous sections has been applied to the evaluation of the radiation properties of an array of 61 circular waveguide elements. The array geometry is shown in Figure 15. The waveguide elements of radius $a = 0.203\lambda$ are loaded with a material of relative dielectric constant $\epsilon_r = 2.54$. Only the two fundamental TE_{11} modes are propagating, all other modes are well below cut-off. The frequency of operation of the antenna is 10 GHz. The array area gain is about 23 dBi, and its angular extension over a cylinder of 100λ is 2.5 deg.

Several thickness and relative dielectric constant values have been considered for the sheet covering the array. The results presented here refer to a thickness d = 0.075 in. and a relative dielectric constant $\epsilon_r = 4$.

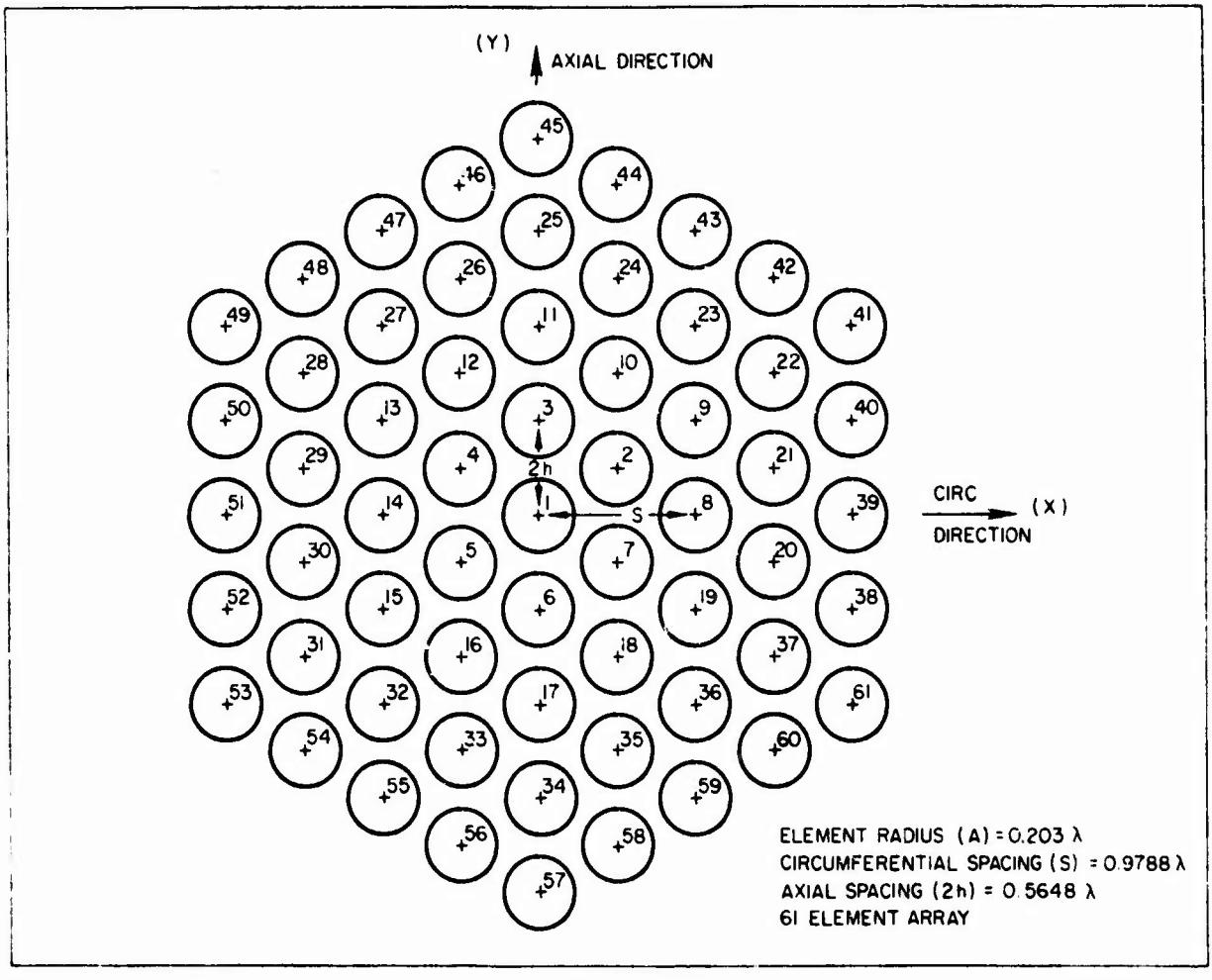

Figure 15 - Array Geometry

This particular choice of d and ϵ_r provides excellent endfire coverage, as will be shown in the following subsections, and an acceptable broadside match for all array elements (typical reflection coefficient $\Gamma \simeq 0.3$ so that no matching network is required in the waveguide elements).

Only the two fundamental TE_{11} modes have been used in enforcing the continuity of the tangential fields at the array aperture. This approximation gives good results in the prediction of element and array patterns [15]. With this two-mode model the mutuals at the aperture plane are expressed by a matrix $\underline{\underline{Y}}$ of dimension 122 x 122. The scattering matrix $\underline{\underline{S}}$ for the array can be computed either by inverting the $\underline{\underline{Y}}$ matrix as in Equation (32) or by

solving a system of equations as in Equation (33). The matrix inversion operation in this case requires ≃48 sec on a UNIVAC 1108 computer, while the repeated solution of the system of Equation (33) requires only 17 sec, a reduction of 3:1 in computer time. The advantage of using the repeated solution of Equation (33) versus the inversion of the matrix $\underline{\underline{Y}}$ becomes more substantial as the number of aperture modes used in field matching is increased. While the computer time required to invert a matrix roughly increase with the cubic power of the dimension of the matrix, the computer time necessary to repeatedly solve Equation (33) increases with the square of the order of the matrix. If four waveguide modes are used in field matching at the array aperture, the time required to invert $\underline{\underline{Y}}$ is about 6.5 min, while the repeated solution of Equation (33) requires slightly over 1 min of computer time with a time reduction of about 6:1.

A substantial amount of computation has been performed to evaluate the radiation characteristics of the array in Figure 15. Only the most illustrative results will be reported here for brevity.

Figure 16 shows the scattering coefficients in the axial direction when the center element (element No. 1) is excited with unit voltage with the TE_{11} modes axially polarized. As it can be seen, the fall off of the coupling coefficients versus distance from the active element is not as rapid as in planar arrays without a dielectric cover. This phenomenon can be clearly seen by comparing the results of Figure 16 with those in Figure 17, where the coupling coefficients are plotted for same array with no dielectric sheet. The slower fall off of the coupling coefficients in the dielectric covered array is due to the fact that the dielectric sheet supports a much stronger wave over the aperture of the antenna than in the case of no dielectric. This wave is partially reflected at the array boundary discontinuity, causing ripples in the coupling coefficient values. The reflection at the array boundary of a wave propagating over the antenna surface is clearly shown in Figure 18 where the axial coupling coefficients are shown for element 17 excited with unit voltage at the TE_{11} axially polarized port. Figure 19 plots the scattering coefficients of the elements on a cardinal plane of the array for element 31 excited with axial polarization. In this case a substantial coupling with the cross polarized TE_{11} port is present.

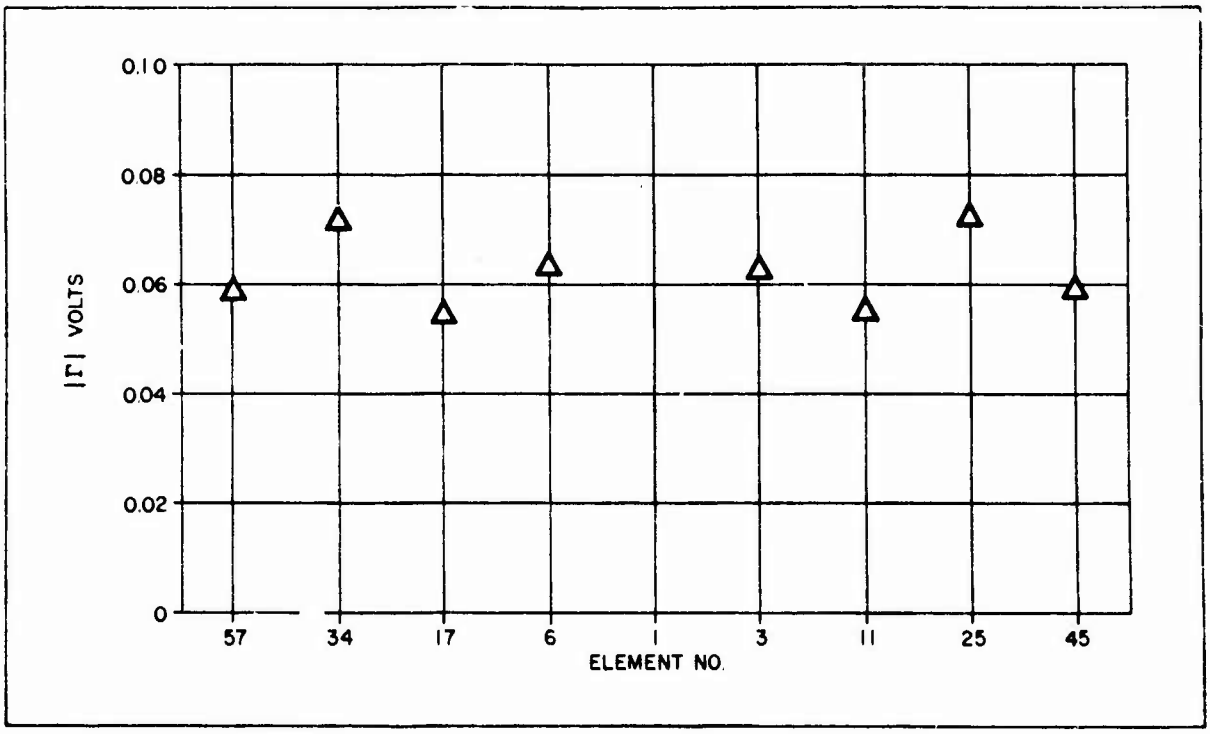

Figure 16 - Scattering Coefficients - Element 1 Actively Excited

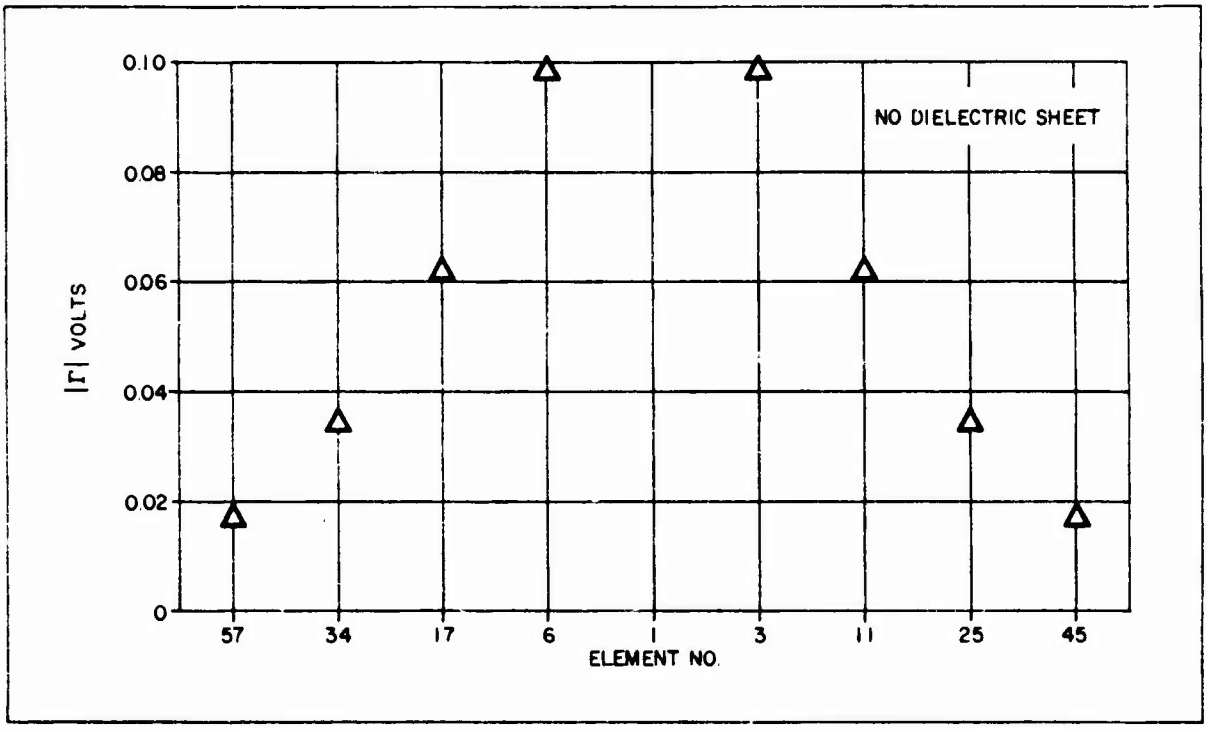

Figure 17 - Scattering Coefficients - Element 1 Actively Excited

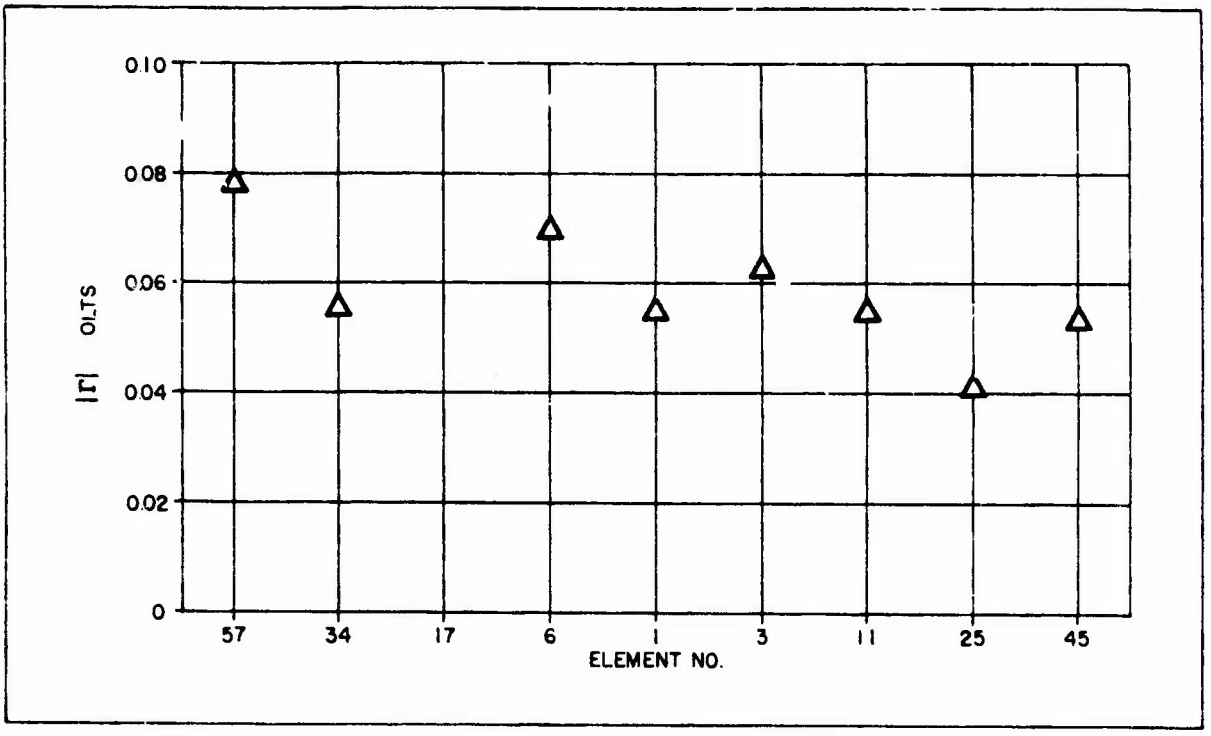

Figure 18 - Scattering Coefficients - Element 17 Actively Excited

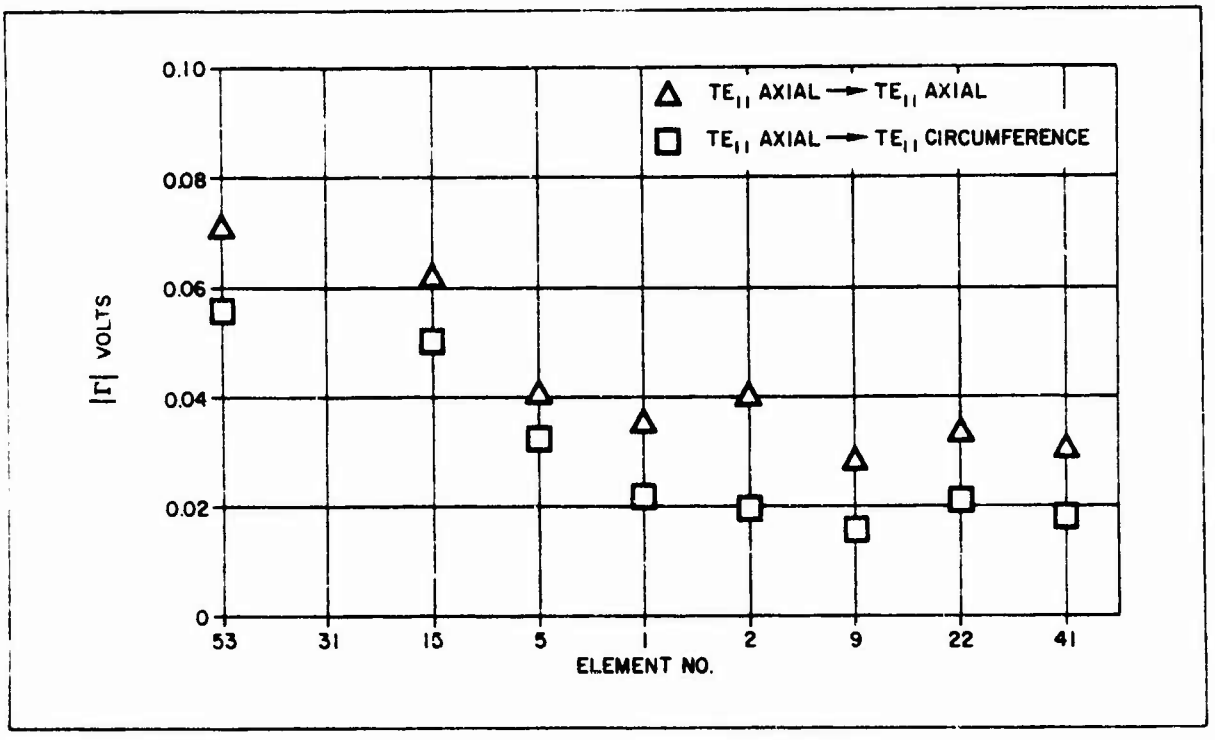

Figure 19 - Scattering Coefficients - Element 31 Actively Excited

Interesting results are shown by the element patterns in the array environment. Figure 20 plots the circumferential plane pattern of the center element excited with the TE_{11} mode axially polarized. In Figure 20 is also shown the pattern of the same element in an infinite planar array environment. The same element in the finite array has slightly higher gain (≈ 0.5 dB) than in the infinite array. No substantial difference is present in the two patterns. The infinite array pattern has a wider beamwidth.

Figure 21 shows the axial plane pattern for axial polarization actively excited in element 1 along with the corresponding infinite planar array case. In this plane the finite size of the array produces substantial pattern oscillations and the departure between finite and infinite array case is much more marked than in the circumferential plane. It is worth noticing that in the finite array pattern of Figure 21 no endfire radiation is present. This is due to the fact that the energy propagating along the surface of the array is trapped in a bound wave and does not contribute to the far field of the antenna.

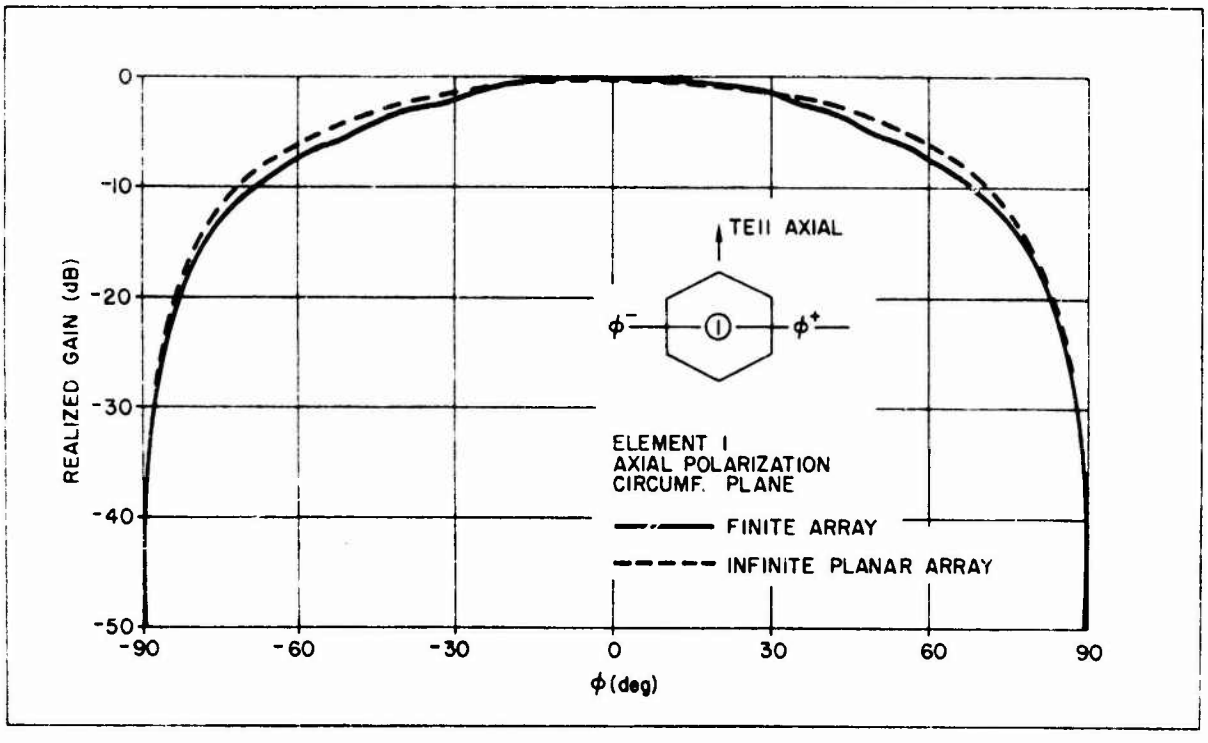

Figure 20 - Array Element Pattern

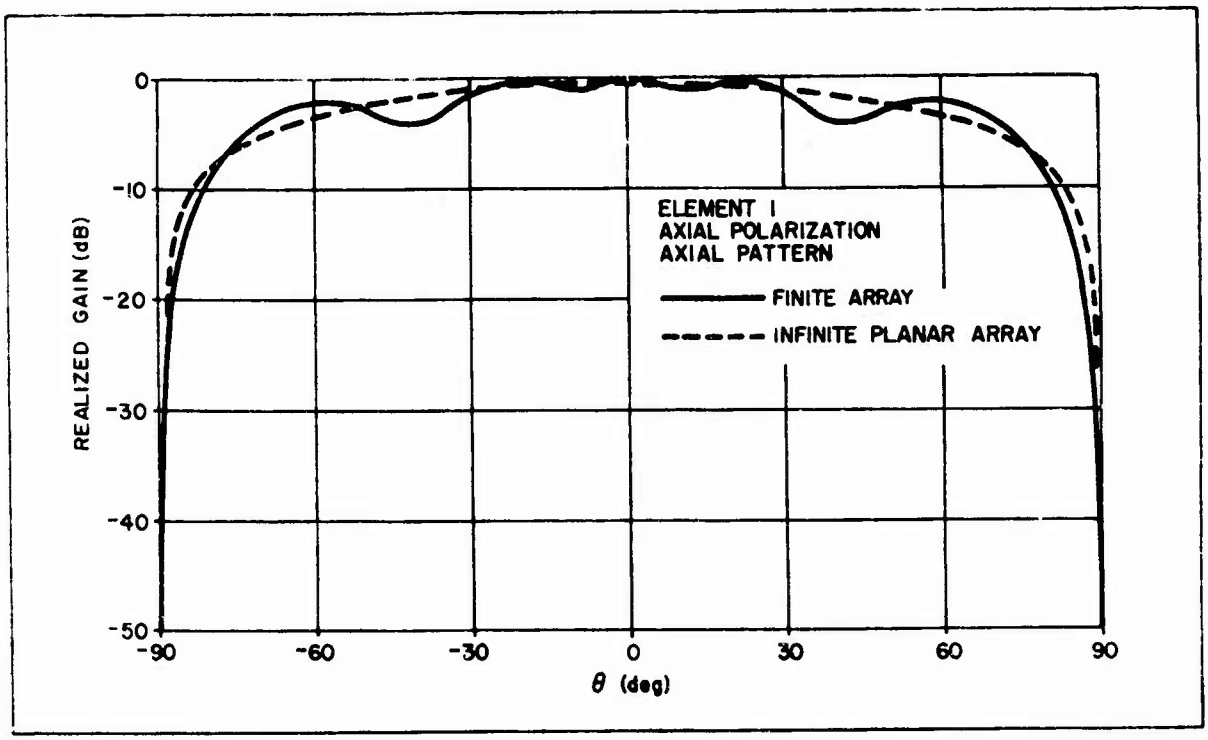

Figure 21 - Array Element Pattern

Radiation pattern ripples, due to the finite size of the array, are much more marked for edge elements, as visible from Figure 22, where is shown the axial plane pattern of element 57 excited with axial polarization. Pattern ripples have about 5 dB amplitude and the element gain at broadside is about 2.5 dB lower than the gain of the same element in an infinite array. It is worth noticing that the finite array pattern shows more radiation than the infinite array model on the side of the edge ($\theta < -70$ deg), while on the side of the array the opposite is detected for $70 \text{ deg} \leq \theta < 90$ deg. Somewhat analogous behavior is exhibited by the pattern of edge element 49 in the axial plane, shown in Figure 23. Element pattern ripples are present in the circumferential plane patterns of element 57 and 49 excited with axial polarization, as shown in Figures 24 and 25, respectively.

The array element pattern oscillation, as shown in the previous figures, can produce substantial variation in the broadside gain of the array elements. In Figure 26 are shown the broadside gains of the slots positioned on the axial and circumferential plane with the gain of the same slots in an infinite array environment. The TE_{11} mode axially polarized is actively excited

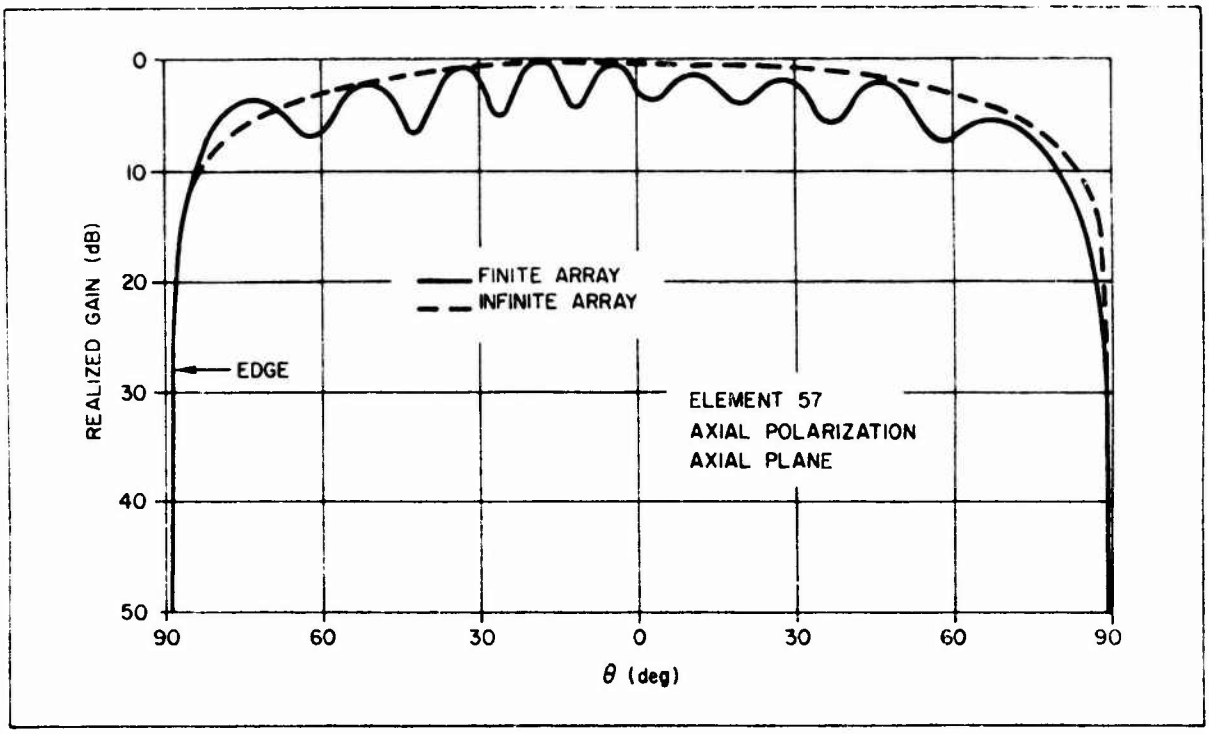

Figure 22 - Array Element Pattern

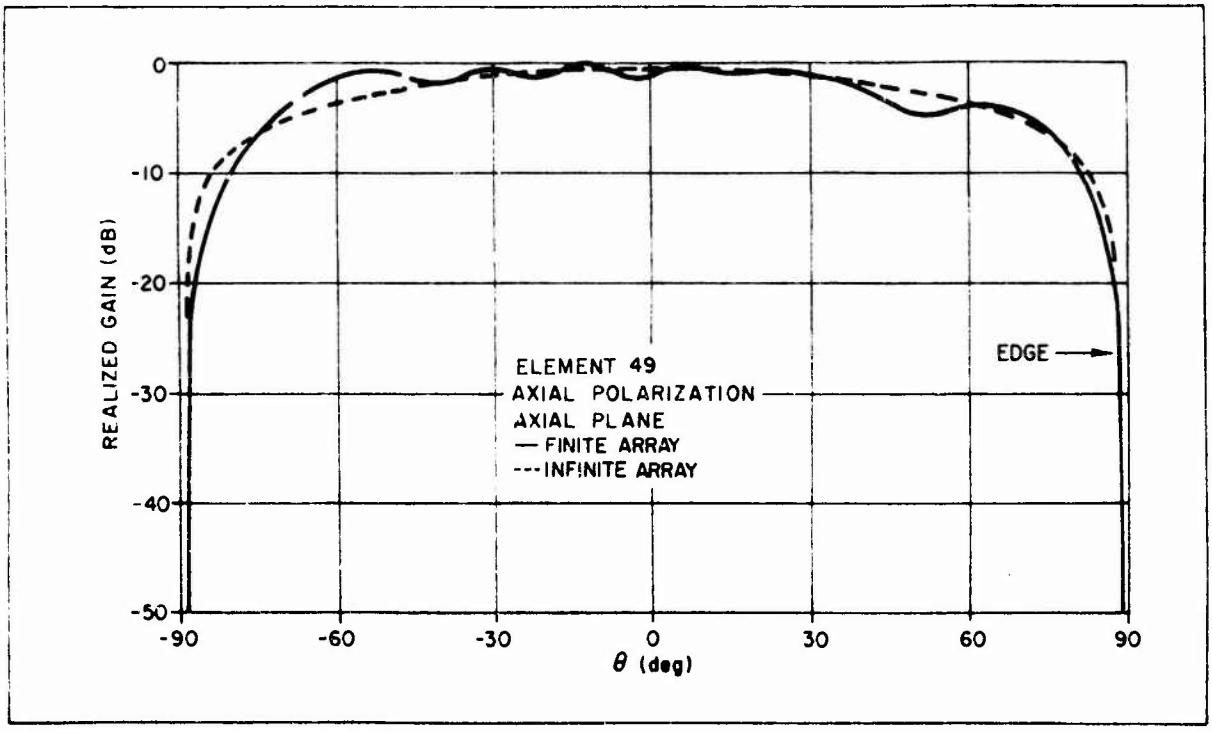

Figure 23 - Array Element Pattern

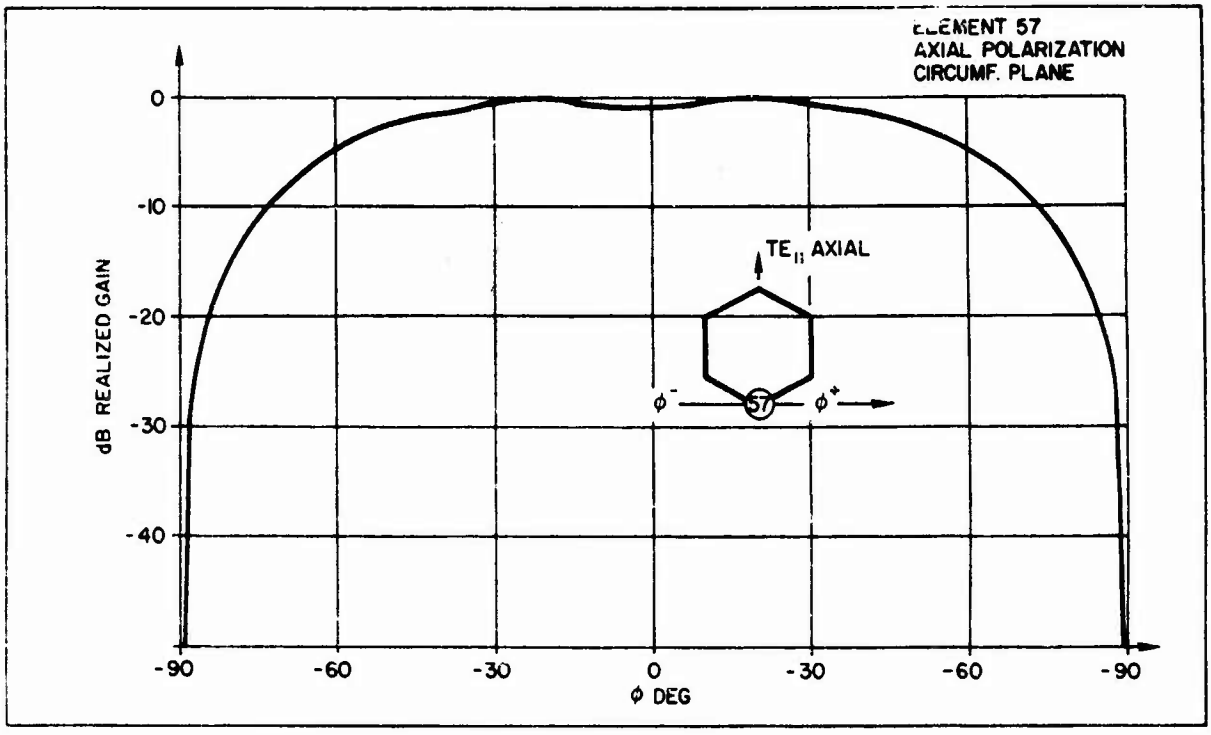

Figure 24 - Array Element Pattern

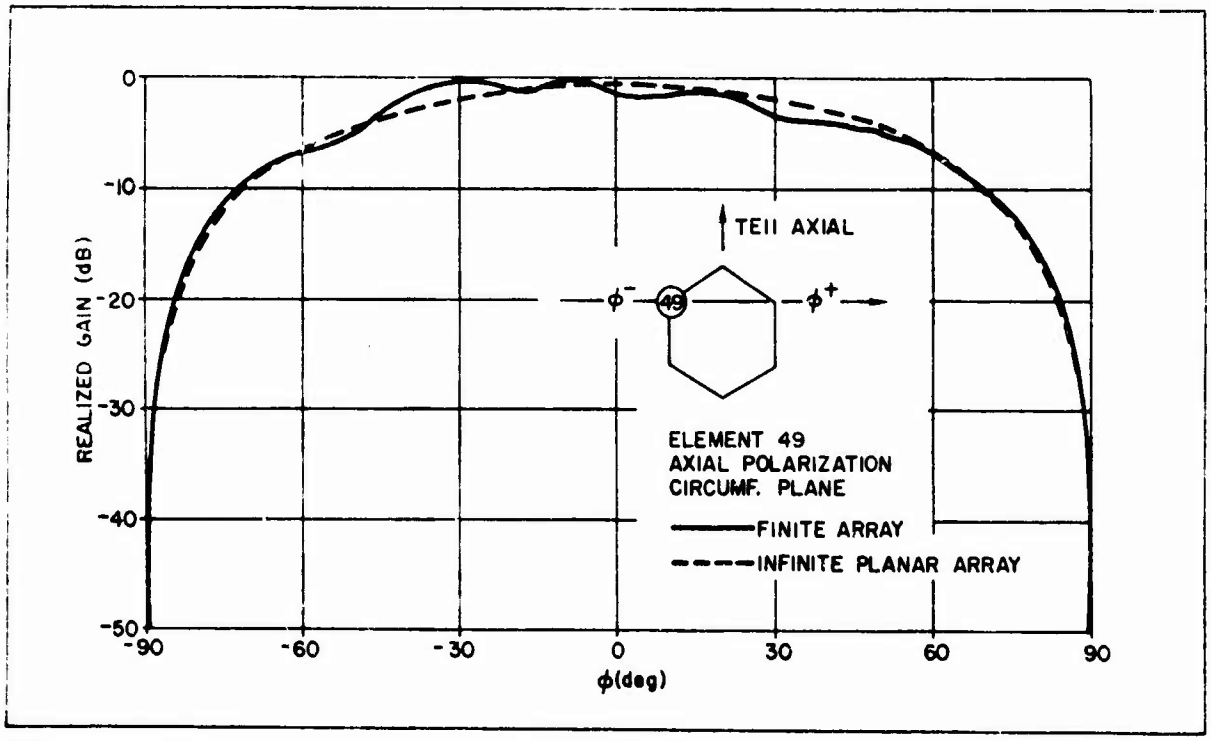

Figure 25 - Array Element Pattern

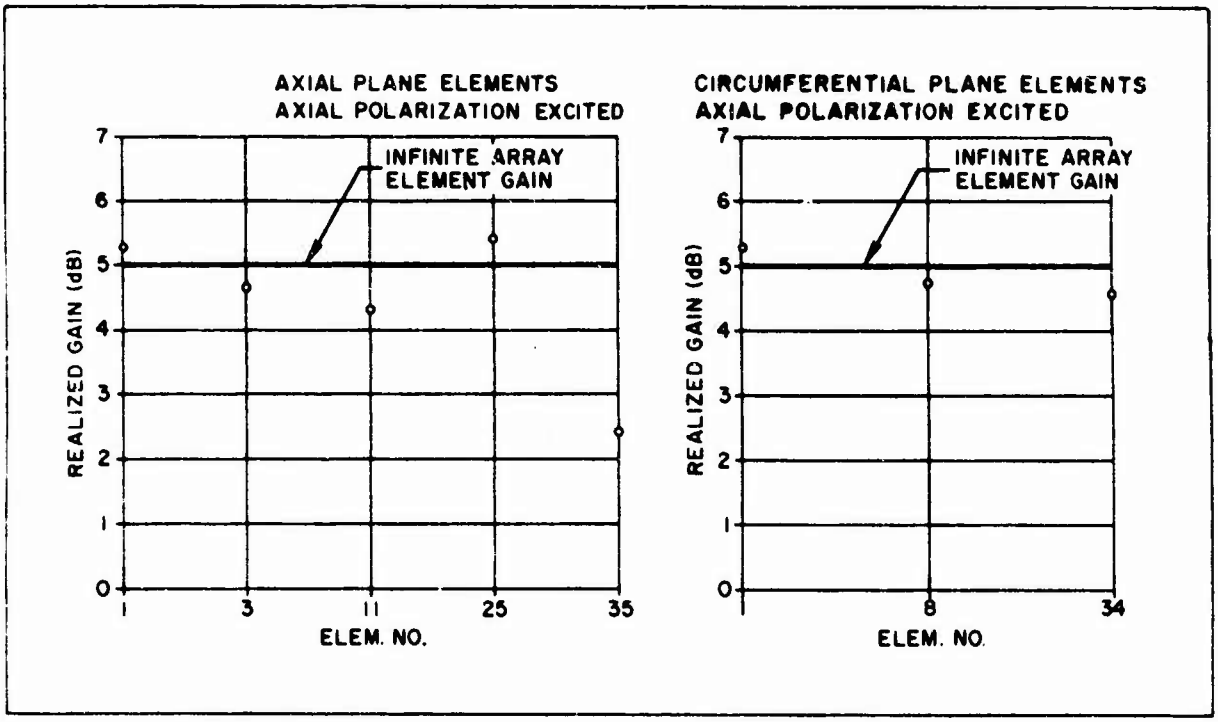

Figure 26 - Element Broadside Gain

in the elements. As it can be seen some elements have gain higher than the infinite array, but in most elements the gain is lower and in some instances substantially lower. The net effect is that the array has a lower gain than expected by assuming each element having an equivalent area gain equal to the infinite array cell area.

The behavior of the elements is not substantially different when excited with circumferential polarization. The results given so far are representative for both polarizations.

Although this array cannot provide hemispheric coverage, its gain performance versus scan angle has been evaluated. Figure 27 shows the gain fall off versus scan angle of the array beam for axial plane scan with axial polarization actively driven with uniform excitation at the array elements. It is worth noticing in Figure 27 that for a steering command to scan at θ_s = 90 deg the peak of the antenna is at $\theta \approx 68$ deg and a scan loss of 4 dB is present. In these conditions at θ = 80 deg the coverage is about

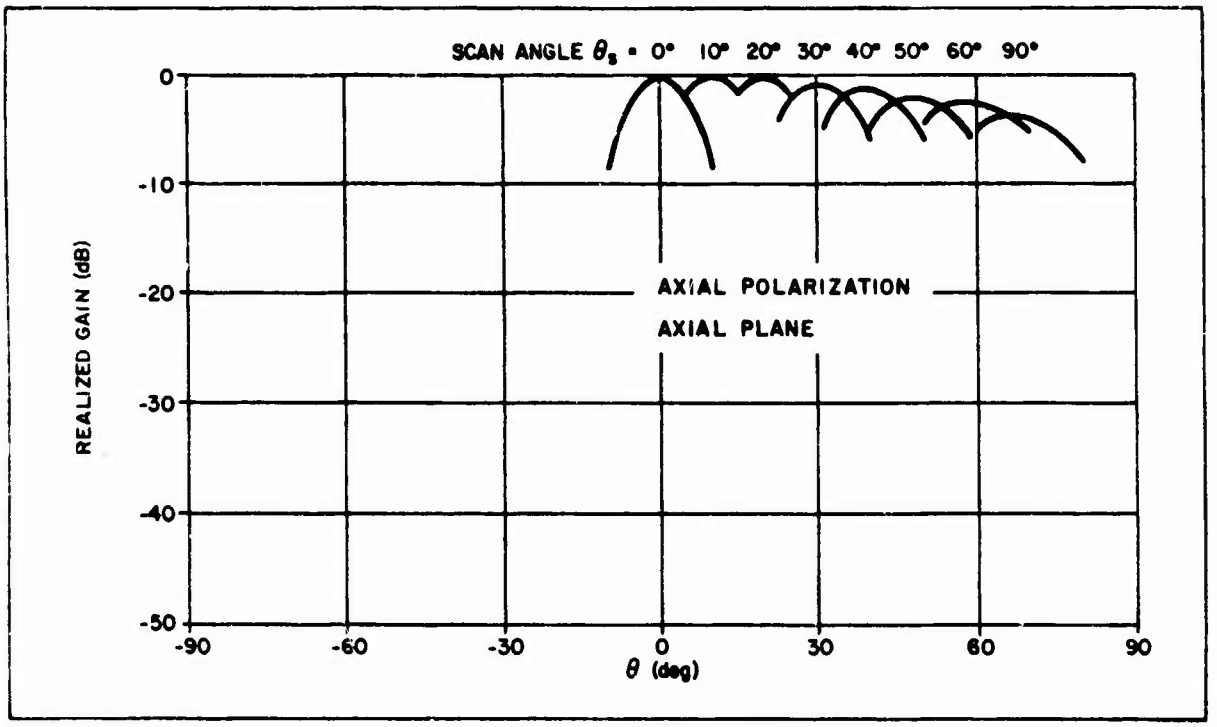

Figure 27 - Array Coverage

8 dB down from broadside. As expected, in the circumferential plane, the gain fall off with scan for axial polarization is even more severe than in the axial plane as shown in Figure 28.

In order to achieve hemispheric scan coverage the radiation in the endfire direction must be enhanced by letting the energy trapped in the dielectric radiate in free space. This can be done by terminating the dielectric sheet covering the array at some distance from the array edge. The radiation properties of dielectric edges will be considered in the next section.

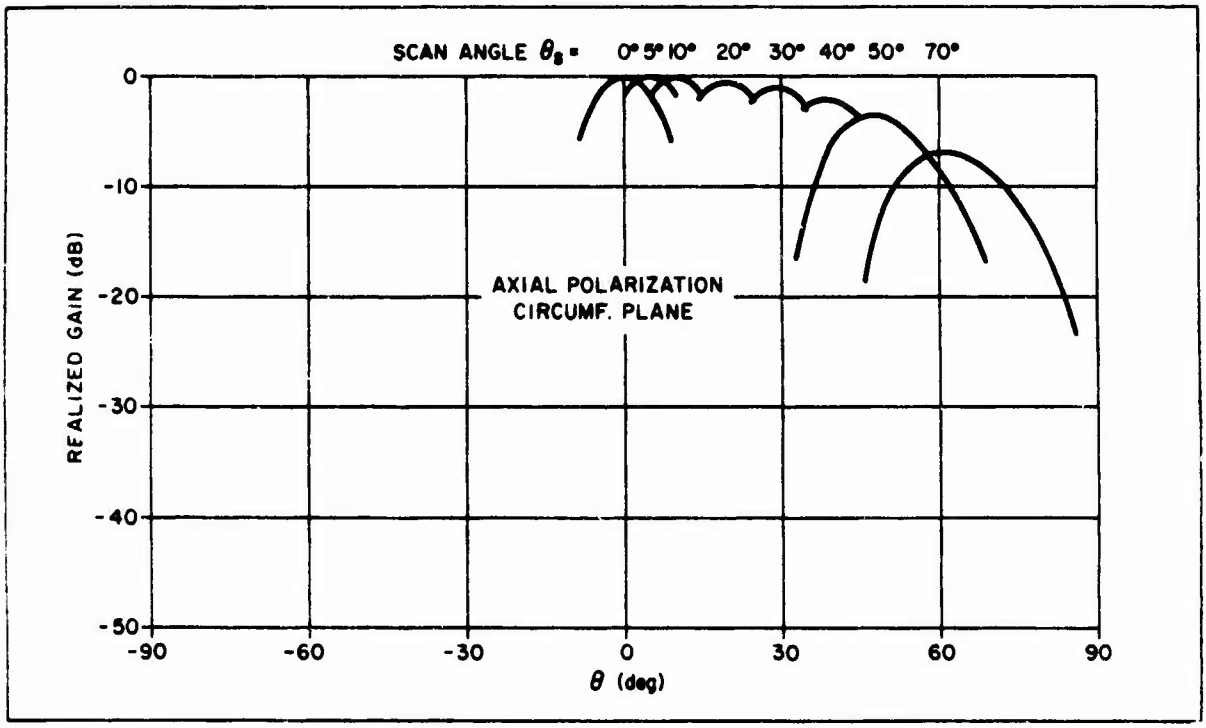

Figure 28 - Array Coverage

4. FINITE ARRAYS OF WAVEGUIDE APERTURES COVERED BY A FINITE DIELECTRIC SHEET

4.1 Radiation Patterns from a Surface Wave Excited Dielectric Wedge

The radiation properties of an E-mode excited, three-dimensional dielectric wedge can be determined from the consideration of the simpler two-dimensional, E-mode excited, wedged dielectric slab. The semi-infinite, wedge terminated, dielectric slab is shown in Figure 29. The slab has width d, relative dielectric constant ϵ_r, taper angle α, and is excited at $z = -\infty$ with the dominant E-mode surface wave ($\vec{H} = \vec{y}_o H_y$).

Although the reflection coefficient of the wedge interface ($z=0$) does not alter radiation patterns, a well matched free space transition is essential in obtaining substantial endfire radiation from a dielectric slab covered array. To facilitate the calculation of the reflection coefficient, Γ, of the tapered wedge, the continuous taper is approximated by infinite stepped sections of length dz, with a corresponding differential impedance. Making use of available analysis for tapered waveguide transitions [28], one finds the reflection coefficient at $z=0$ to be given by:

$$\Gamma_{in} = \frac{1}{2} \int_0^{\ell} e^{-2j\beta(z)\, z} \frac{d}{dz} [\ln \bar{Z}(z)]\, dz \qquad (56)$$

where $\beta(z)$ is the surface wavenumber computed by assuming that the local wave number in a section of the dielectric wedge is equal to that of an infinite slab of the same thickness. In Equation (56) $\bar{Z}(z) = \beta(z) / \beta(o)$.

The computed reflection coefficient magnitude versus taper length for an $\epsilon_r = 4$, $d = 0.075\lambda$ thick dielectric slab is plotted in Figure 30. The fall off and periodicity is similar to other taper matching transitions described in [28]. For a taper length greater than 0.8λ the reflection coefficient remains less than 0.02, which provides a near perfect free

space launching of the surface wave. For zero taper length the reflection coefficient via Equation (56) is 0.185, which in this limit checks with the simple calculation of $\left|\Gamma\right| = \left|\frac{k - \beta(o)}{k + \beta(o)}\right| \approx 0.185$ $(k = 2\pi/\lambda)$.

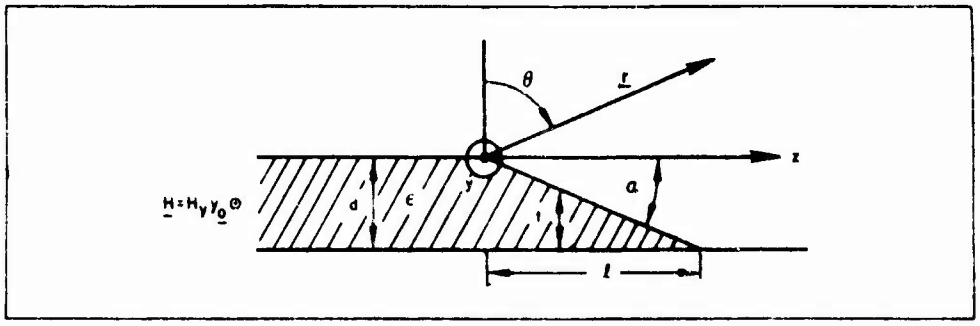

Figure 29 - Wedge Geometry

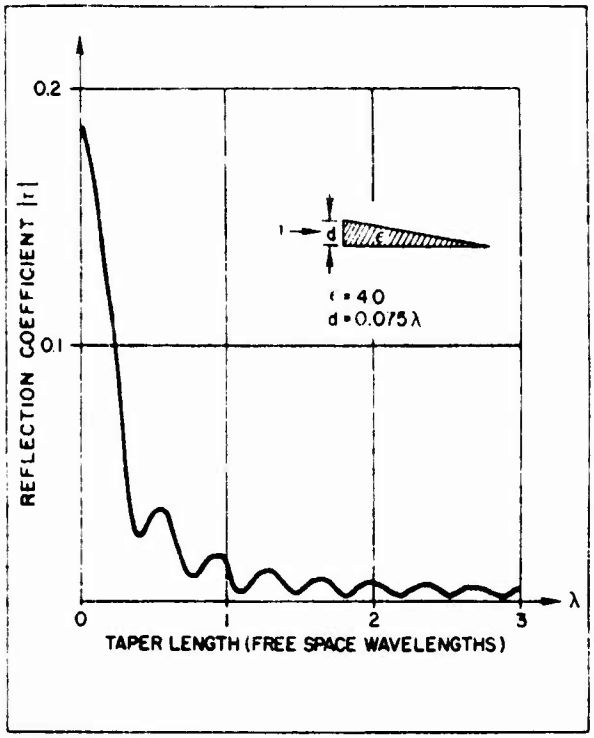

Figure 30 - Wedge Reflection Coefficient

The surface wave propagation constant distribution along the taper, $\beta(t)$, (implying $\beta(z)$ directly, which is used in Equation (56)) is plotted in Figure 31 for an $\epsilon_r = 4$ dielectric slab. The solutions for $\beta(t)$ are found from the well-known transcendental equation:

$$\epsilon_r \sqrt{\beta^2 - k^2} = \sqrt{\epsilon_r k^2 - \beta^2} \tan \sqrt{\epsilon_r k^2 - \beta} t \qquad (57)$$

The surface wave propagation constant gives the near field phase distribution used in calculating patterns. This assumed local phase behavior is compared with results obtained using a quasi-optics approach [29-30] in Figure 32, for an $\epsilon_r = 2$ and $d = 0.375\lambda$ wedge. The good agreement in the near field propagation constant distribution establishes confidence in the pattern calculations.

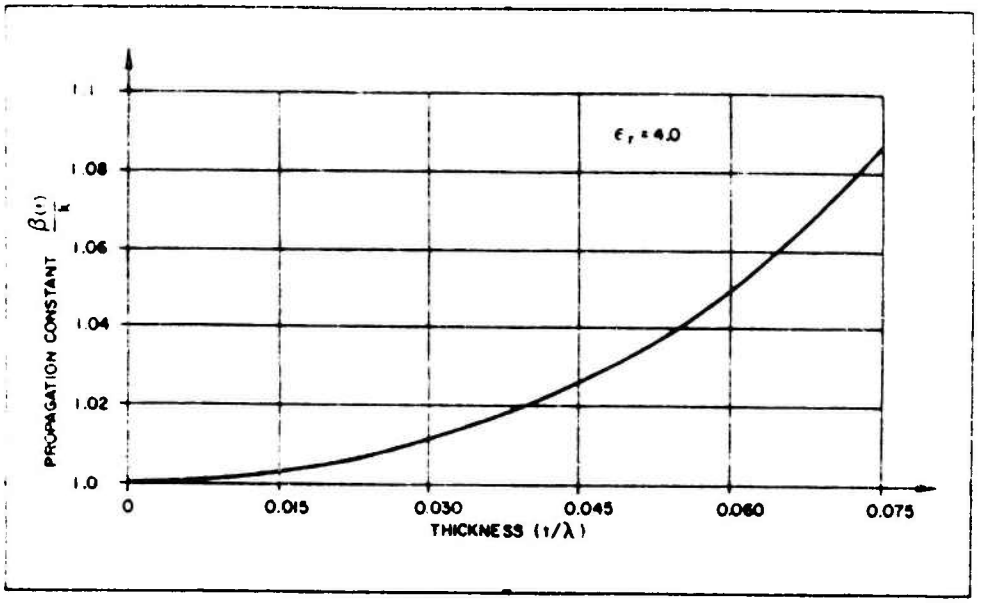

Figure 31 - Wedge Near Field Propagation Constant

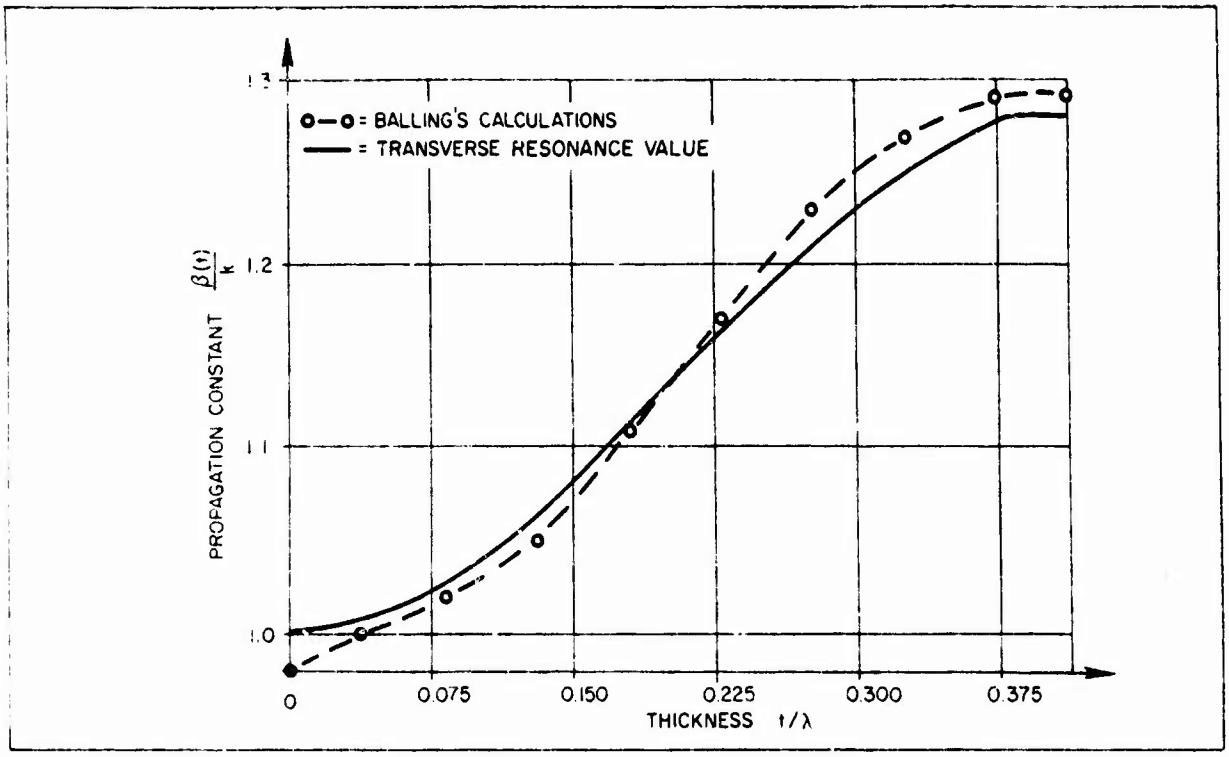

Figure 32 - Wedge Near Field Propagation Constant

Two methods to determine the near field amplitude distribution were tried. One approach relied on conservation of power flow in the z direction and the simultaneous matching of boundary conditions assuming the existence of only the surface wave mode. A second approach assumed infinitesimal discontinuities radiating locally from Y oriented line sources. The change in impedance levels implied a radiation conductance (to maintain perfect match) associated with each dz increment. Both these methods appear to be poor approximations in predicting field amplitude behavior at the tip discontinuity. Depending on geometry, both methods showed similar trends of either an increased near field amplitude at the initial taper transition or a fall off. However, the typical amplitude function was relatively constant. Balling's [29-30] results for near field amplitude also showed a relatively constant amplitude, but comparisons with either of the simpler methods were poor.

The quasioptics calculations were not pursued because of the complexity in programming and excessive cost of computations. Moreover, patterns

calculated using different amplitude functions produced very little change within the main beam and only slight variations in sidelobe levels.

Because of the uncertainty of the amplitude function, in particular, what appeared to be a variation about some nominal constant value, a uniform amplitude distribution was selected for computations.

From power conservation considerations the magnetic field amplitude |B|, normalized to the square root of the incident power, is

$$\frac{|B|}{\sqrt{P_2}} = \left[\frac{2 k \zeta h p}{\beta(o) \left(p \left[h d + \frac{\sin 2hd}{2} \right] + h \cos^2 hd \right)} \right]^{\frac{1}{2}} \tag{58}$$

where

$$h = \sqrt{\epsilon_r k^2 - \beta^2}$$

$$p = \sqrt{\beta^2 - k^2}$$

and

ζ = free space admittance.

The far magnetic field pattern computed in a standard manner is given by:

$$\underline{H}(\theta) = \hat{y} \; 2 \sqrt{\frac{j}{8\pi k}} \int_d^o |B| \cos ht \left[\beta(t) \sin \alpha + \right. \tag{59}$$

$$\left. - j p \cos \alpha \right] e^{-j \frac{d-t}{\sin \alpha} \left[\beta(t) \cos \alpha + k \sin (\theta + \alpha) \right]} dt$$

Patterns computed via Equation (59) are presented in Figure 33 for $\epsilon_r = 4$, $d = 0.075\lambda$ wedge with taper length, ℓ, as a parameter. Depending on the extent of coverage required off the endfire direction a suitable taper length can be chosen.

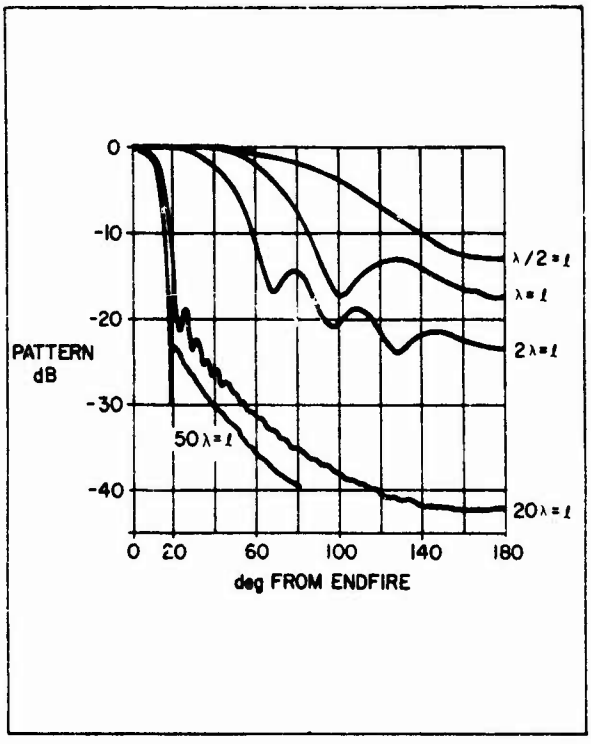

Figure 33 - Dielectric Wedge Pattern

4.2 Approximate Model for the Radiation from Surface Wave Excited Three-Dimensional Dielectric Wedges

The radiation from a three-dimensional dielectric wedge can now be approximately evaluated. We suppose that the dielectric sheet covering the array is disc shaped. This disc has a uniform thickness d over a radius r, then the thickness of this disc is tapered to zero over a length ℓ. The uniform thickness section of the disc extends beyond the array boundary, as shown in Figure 34.

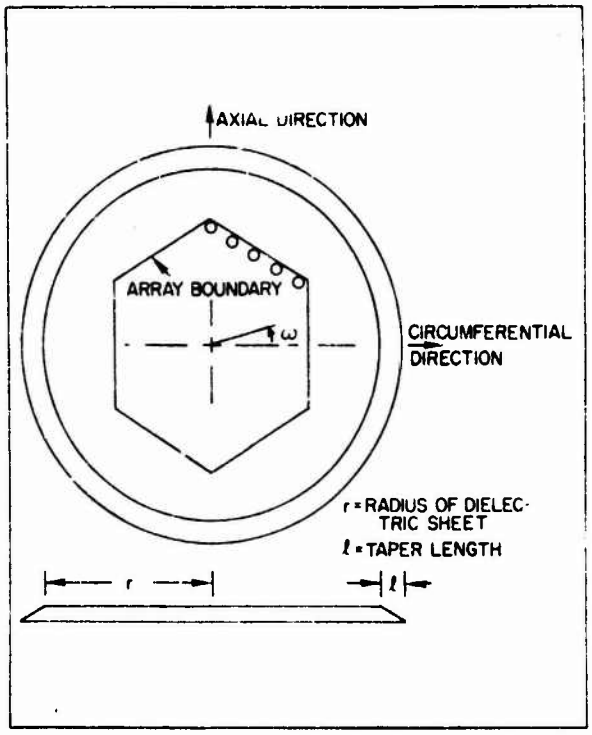

Figure 34 - Dielectric Geometry

The following approximations are made in evaluating the radiation from the dielectric taper:

1) Only one bounded wave is incident at the dielectric wedge. This bounded wave is given by Equation (49) for $\theta = \pi/2$.
2) The distance of each point of the wedge from the array elements is big enough so that Equation (49) can be applied.
3) An infinitesimal arc $rd\omega$ of the dielectric wedge at the point $r\omega$ radiates as if it were part of an infinite linear dielectric wedge tangential to the dielectric disc at the point $r\omega$ so that Equation (59) can be used in the evaluation of the pattern.

With these approximations, the radiation pattern from the three-dimensional disc wedge can be written as:

$$\hat{\theta} P(\theta,\phi) = \eta F(\theta)\hat{\theta} \int_{\phi-\pi/2}^{\phi+\pi/2} \cos(\omega-\phi)\, S(\omega)\, e^{jkr\cos(\omega-\phi)\sin\theta}\, rd\omega \quad (60)$$

In Equation (60) η is free space impedance, $F(\theta)$ is the far magnetic field pattern (obtained through Equation (59)) of the infinitesimal arc $rd\omega$ for unit magnetic field excitation and $S(\omega)$ is the wedge excitation at the point ω. The excitation $S(\omega)$ is given by:

$$S(\omega) = \sum_{i=1}^{N} (H_{1i} \sin\omega + H_{2i} \cos\omega) \frac{e^{-jt_p r_i}}{\sqrt{r_i}}$$

where r_i represents the distance between the ith element and the point $r\omega$ on the wedge. H_{1i} and H_{2i} represent the amplitudes of the magnetic field incident to the wedge, respectively due to the TE_{11} mode axially polarized and the TE_{11} circumferentially polarized excited at each array element aperture. The relation between H_{1i} and H_{2i} and the modal aperture voltages is simply given by:

$$H_{1,2i} = -j\pi J_1(at_p)\sqrt{\frac{2j}{\pi t_p}} \frac{NP^{TM}(t_p)}{\frac{d}{dt} DP^{TM}(t)\Big|_{t=tp}} \cdot$$

$$V_{1,2i} \frac{Kd}{\eta_d w_d} \frac{\cos w_d d}{j \sin w_d d}$$

where the notations are as in Equation (49).

4.3 Radiation of a Finite Array Covered by a Finite Size Dielectric Sheet

We can now evaluate the radiation from the 61-element array previously considered, when the dielectric sheet is terminated at a certain distance from the antenna edge.

With reference to Figure 34, several radii, r, and taper length ℓ have been taken into consideration. For brevity, only the most representative results, relative to the case d = 0.075 in., $\epsilon_r = 4$, $r = 3\lambda$ and $\ell = 3\lambda$, will be presented here.

Figure 35 shows the element pattern in the array environment of element 1 (Figure 15) in the axial plane for axial polarization actively excited. The pattern of the same element is superimposed in the case of no wedge. Comparing the two patterns it can be seen that interference exists between the space wave emanating from the excited element and the radiation from the dielectric wedge. This interference causes the element pattern to have ripples and rather deep notches. It should be noticed, however, that, because of the

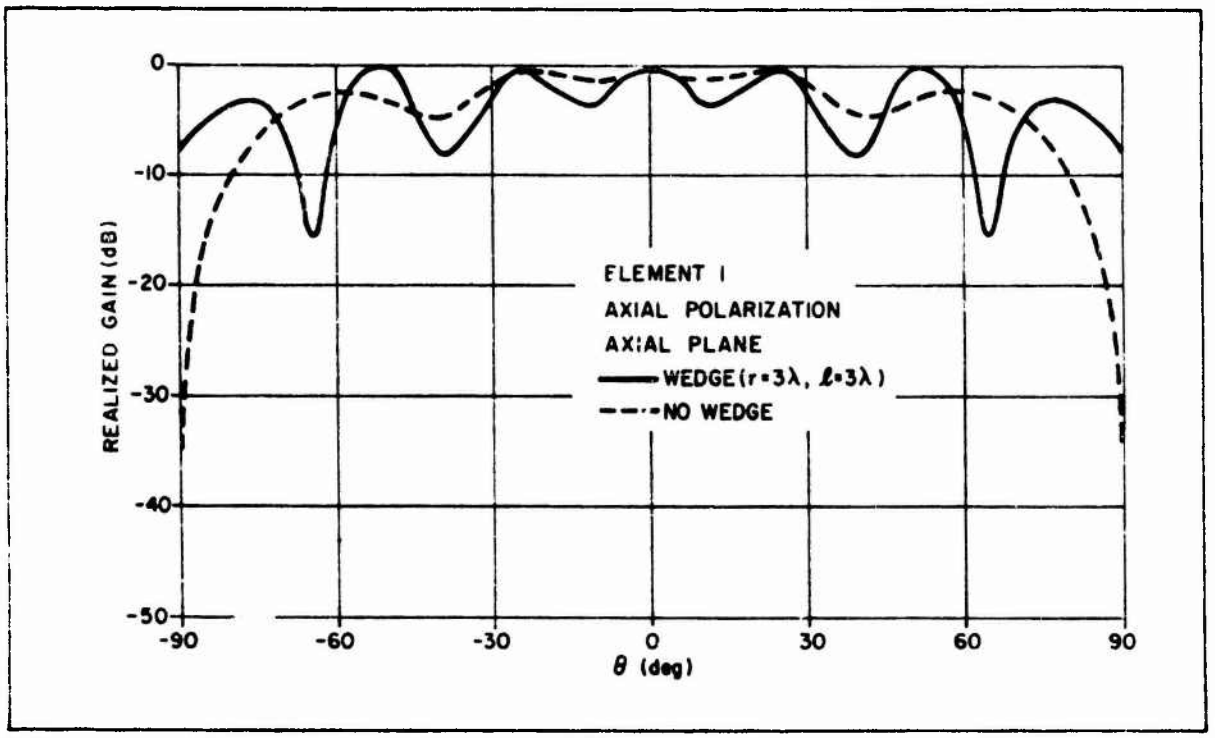

Figure 35 - Element Pattern in an Array Environment

dielectric wedge, the element pattern shows a substantial radiation in the endfire direction, as necessary to achieve hemispheric coverage. In the circumferential plane the pattern of element 1, excited with axial polarization, is not different from the one shown in Figure 20, because the symmetry of the array and the dielectric cover is such that no wedge radiation is present in this plane.

Figure 36, plotting the axial pattern for axial polarization of element 57, shows very clearly how strongly the dielectric wedge can radiate when excited by an array element close to it. In this case the peak of the wedge radiation is about 5 dB higher than the direct radiation from the array element. In the circumferential plane the contribution to the far field of element 57 is not as substantial as in the axial plane as can be seen from Figure 37; it is interesting to notice that, because of the dielectric taper radiation, this

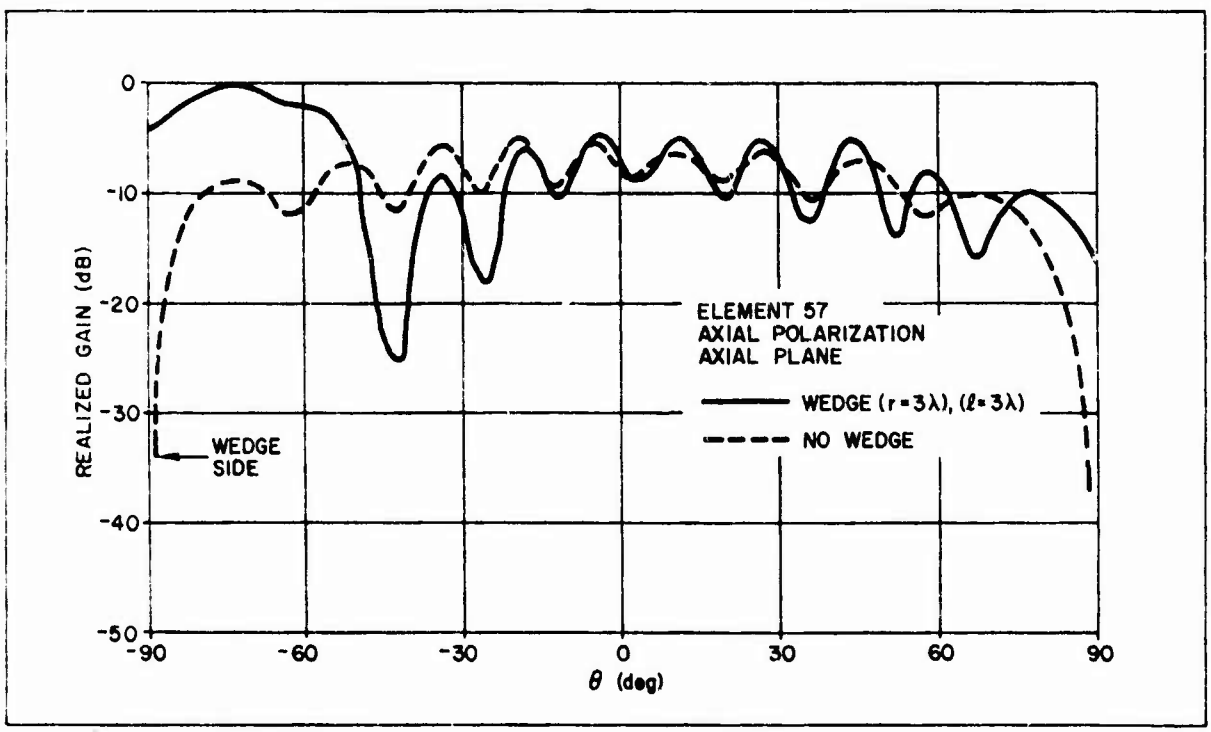

Figure 36 - Axial Pattern for Element 57

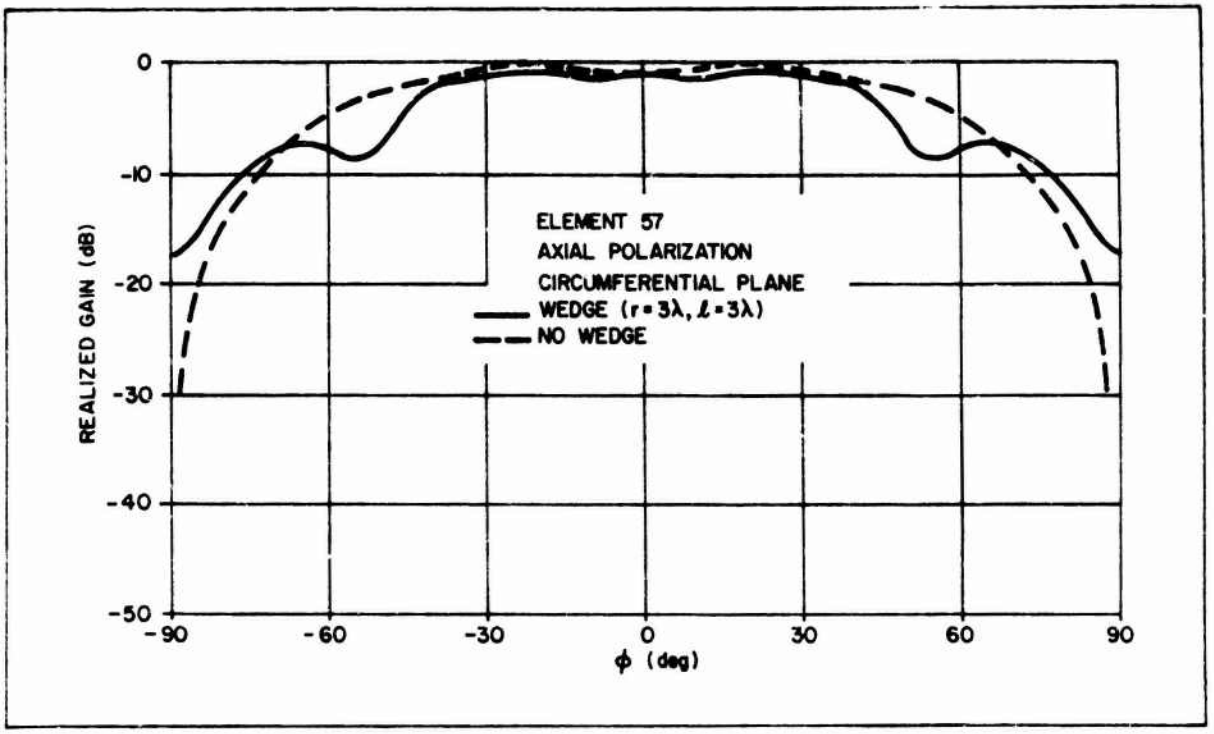

Figure 37 - Circumferential Pattern of Element 57

H-plane pattern shows a finite value of radiation in the direction $|\theta| = 90$ deg. Analogous characteristics are present in the axial and circumferential patterns of element 49 shown in Figures 38 and 39.

The coverage and pattern performance of the 61-element array of Figure 15 has been evaluated. The interference between the space wave radiated by the elements and the far field form the dielectric wedge, already pointed out in the array element patterns, is probably the most interesting feature of the array radiation.

Figure 40 shows the axial pattern of the array in the no scan condition. The array illumination is a circular Taylor distribution with $\bar{n} = 2$ and -20 dB SLL; the elements are excited with axial polarization. For this scan condition the dielectric wedge is not heavily excited and the array pattern presents the only peculiarity of having some noticeable lobes in the direction close to end-fire. As the scan angle is increased and the wedge is more excited, the array pattern undergoes substantial distortion as can be seen from Figures 41, 42 and 43. The most dramatic effect of the interference is shown in Figure 43 giving the axial pattern of the array for 90-deg scan in the axial plane.

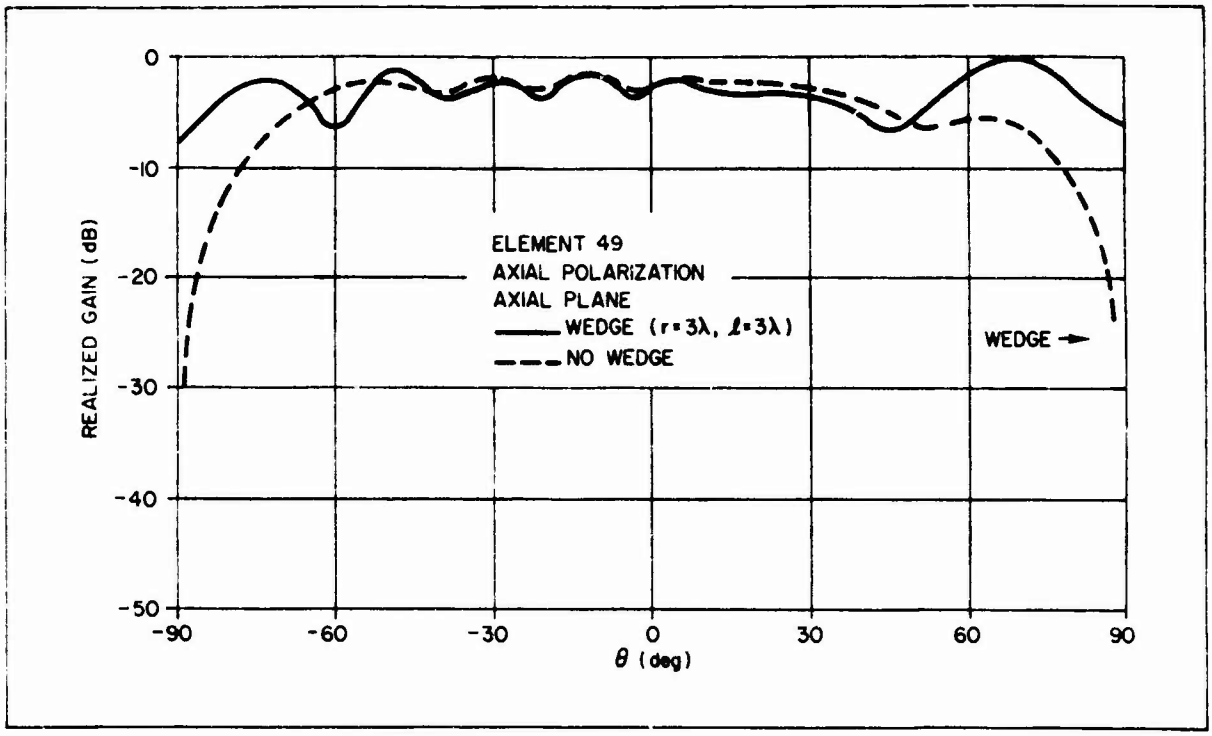

Figure 38 - Axial Pattern of Element 49

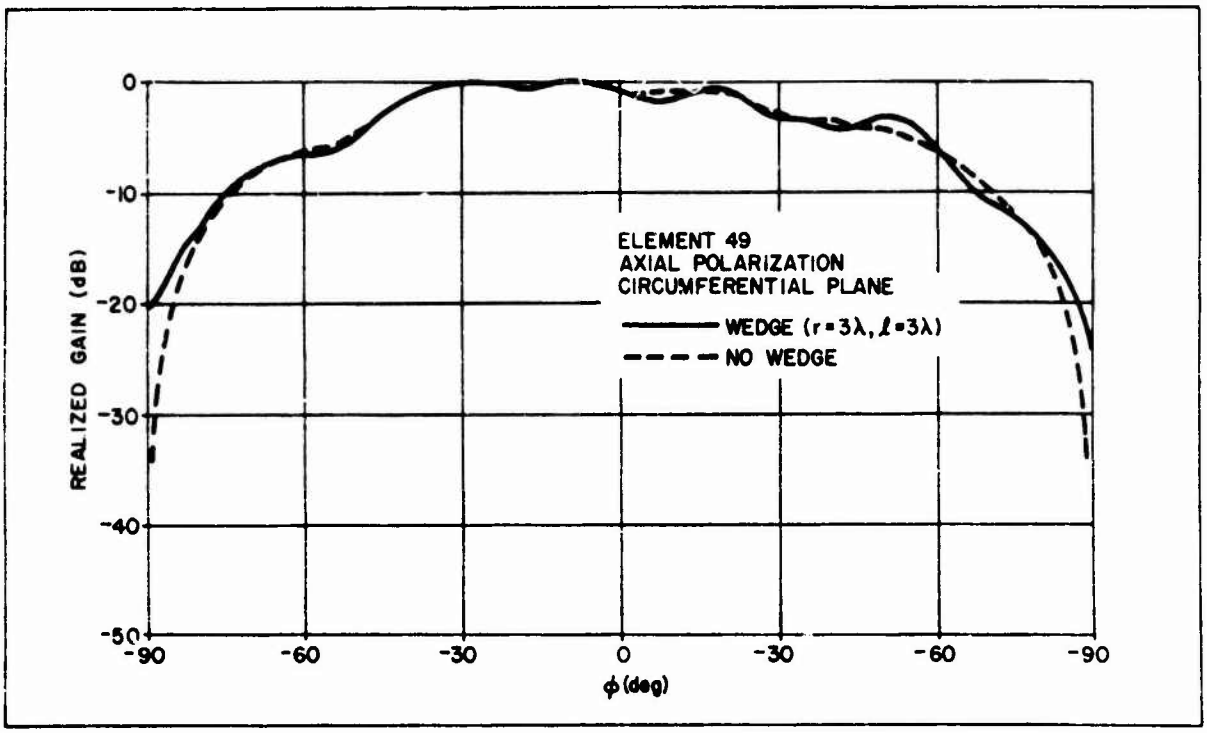

Figure 39 - Circumferential Pattern of Element 49

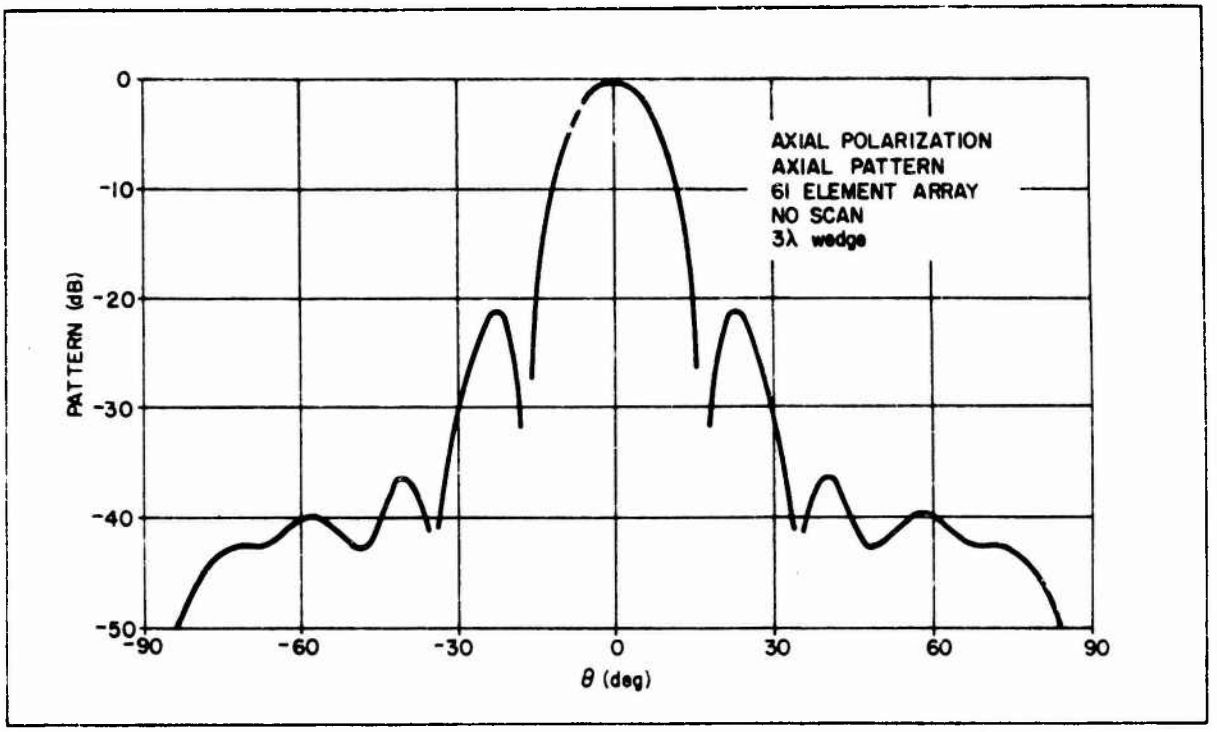

Figure 40 - Array Axial Pattern in No Scan Condition

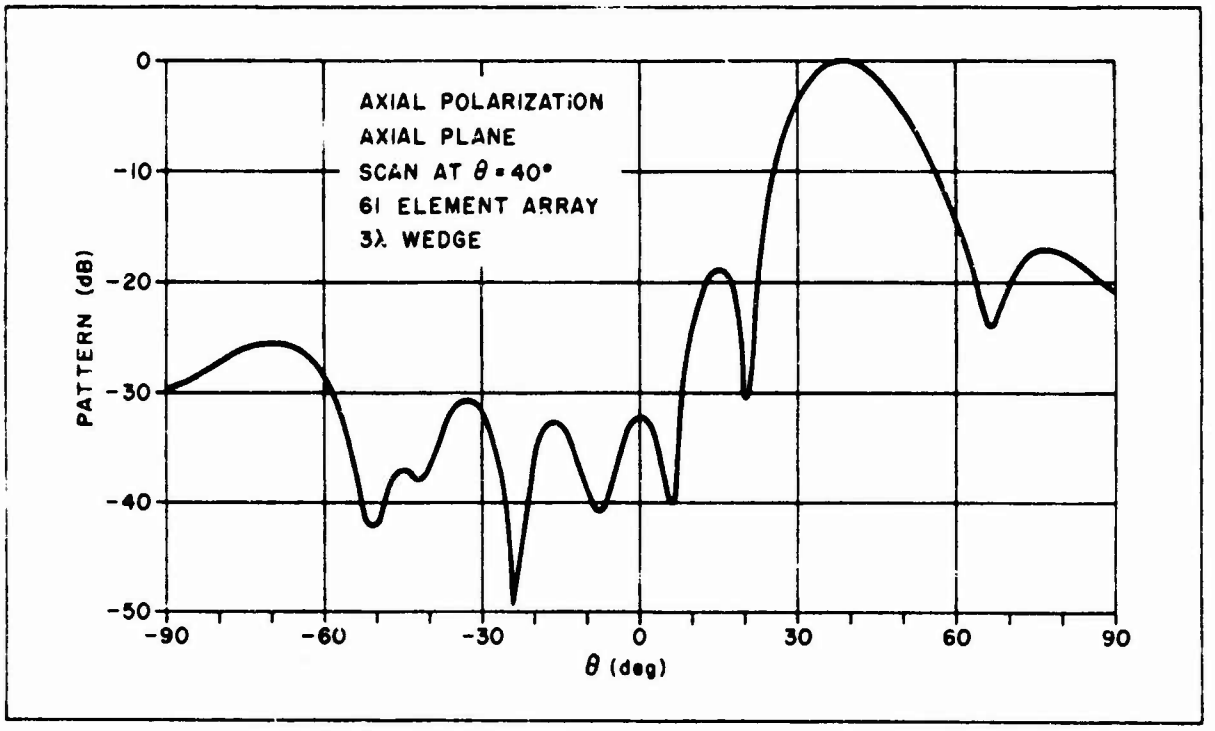

Figure 41 - Array Pattern

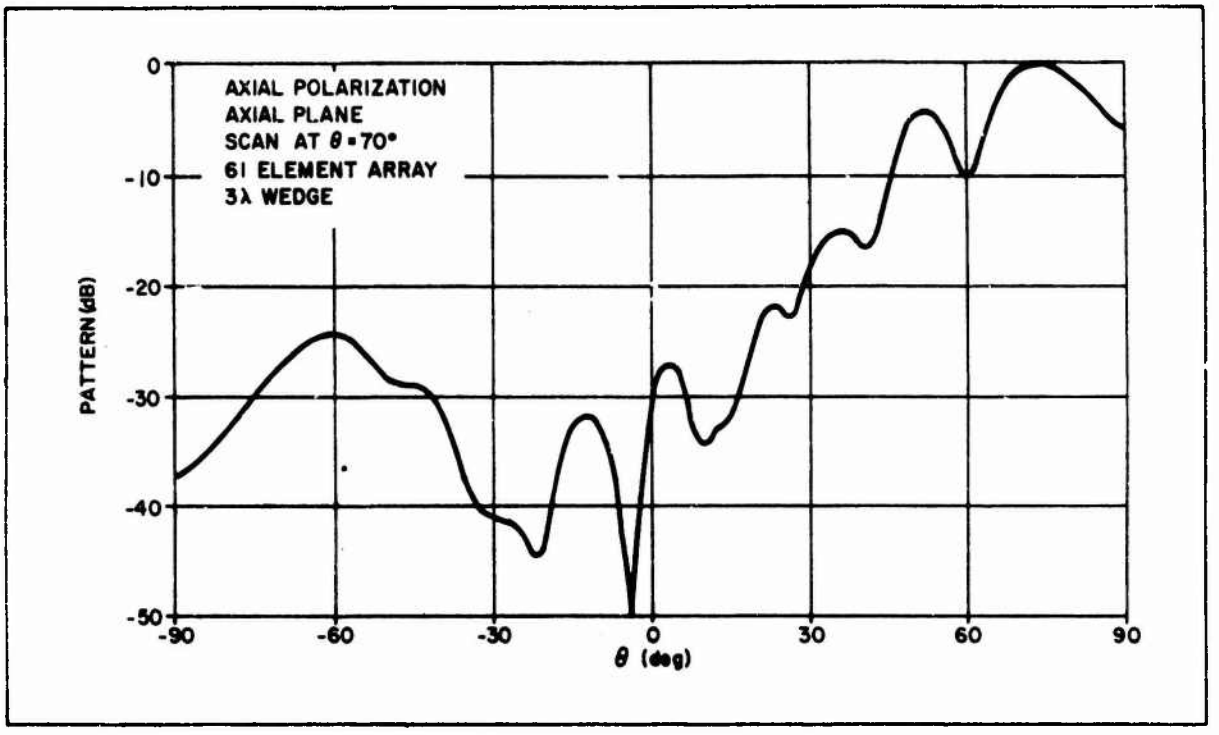

Figure 42 - Array Pattern

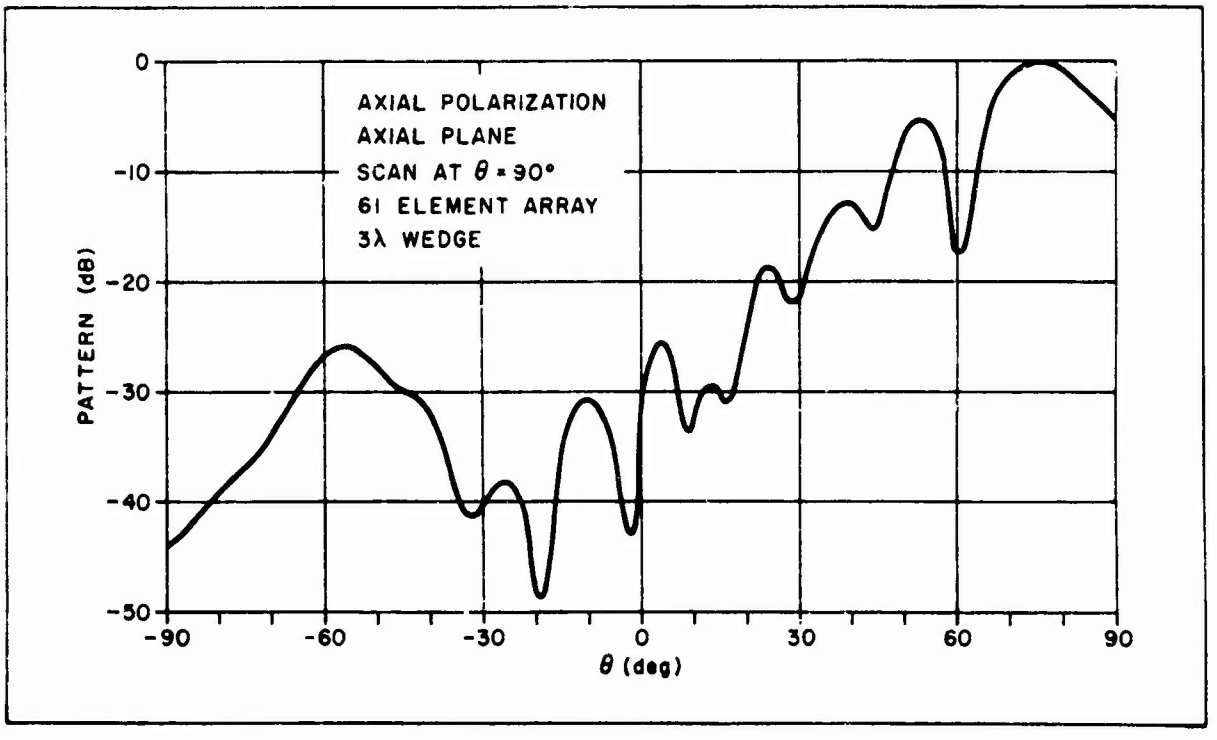

Figure 43 - Array Pattern

In this case the array main beam undergoes interference from the wedge radiation for $\theta \approx 60$ degrees showing a rather deep notch. At this angle the array space wave and the dielectric wedge contribute to the array pattern with roughly the same amplitude and opposite phase. For $\theta > 65$ deg, the array pattern is practically due only to the wedge radiation. It is worth noticing that in the region $-90 \text{ deg} \leq \theta \leq -30$ deg, a substantial radiation is present due to the dielectric wedge. The array coverage (envelope of the peaks of the beam) in two planes is shown in Figure 44, when the array is excited with the polarization in the plane of scan. The coverage performance in the two planes is substantially analogous, any difference is due to the array geometry. The antenna coverage is provided by the space wave radiated by the elements in the angular region < 50 deg. At $\approx \pm 60$ deg there is a notch in the coverage due to the interference between wedge and array element radiation, while for the angular region > 65 deg the coverage is essentially provided by the wedge radiation. The coverage in the region close to 90 deg has been

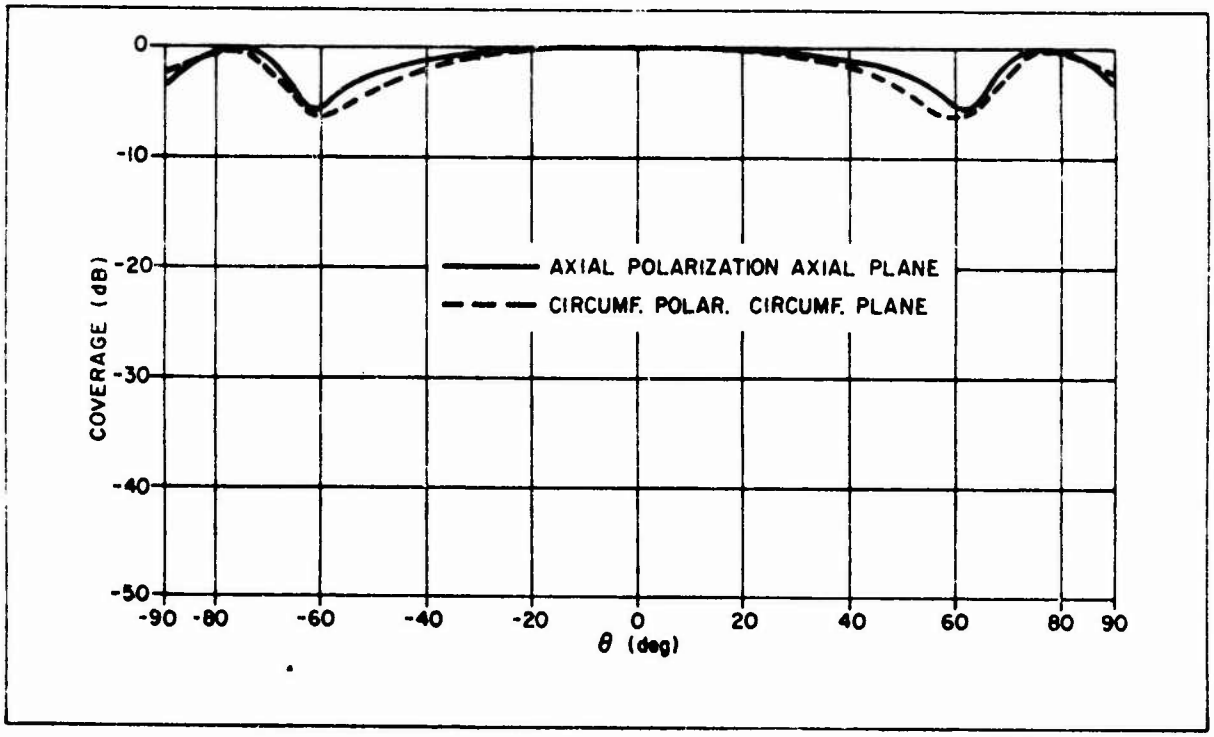

Figure 44 - Array Coverage in Two Planes

obtained by the giving the array elements phase commands which would steer the array main beam outside visible space. The maximum endfire coverage, as shown in Figure 44, has been found for a phase command $|\underline{u}_o| = \frac{2\pi}{\lambda} 1.1$. Hemispheric scan coverage from the array is obtained by exciting the antenna with circular polarization as shown in Figure 45, plotting the array coverage in the circumferential and axial plane. Comparing Figures 44 and 45, it can be seen that the notch at $\approx$ 60 deg is only partially filled by using circular polarization. Moreover, there is a 3-dB polarization loss in the endfire direction. It should be noticed, however, that the coverage in Figure 45 does not show a gain falloff greater than 6.5 dB, which is very close to the 6-dB goal of this investigation.

The influence of the length, ℓ, of the dielectric wedge (the radius r is kept constant) on the array coverage is shown in Figure 46 in the axial plane with axial polarization excited. As it can be seen, for values of ℓ smaller than 3λ it is not possible to achieve hemispheric scan coverage

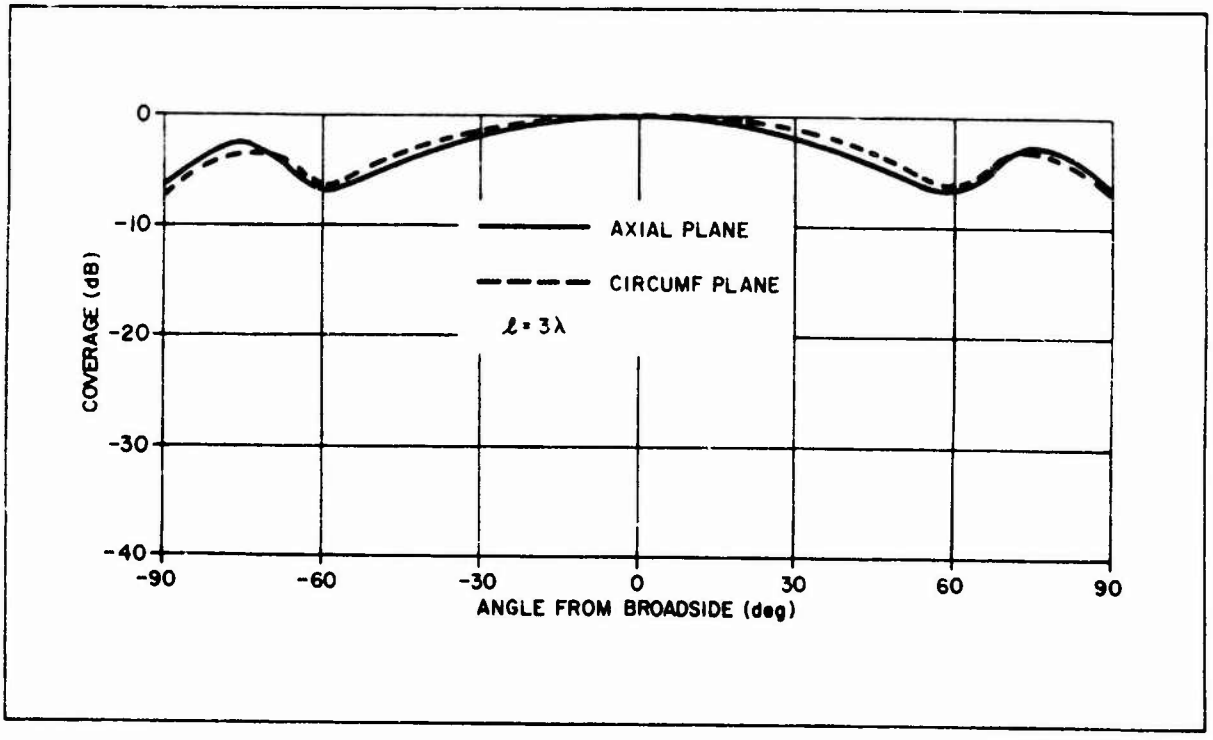

Figure 45 - Array Coverage.Circular Polarization

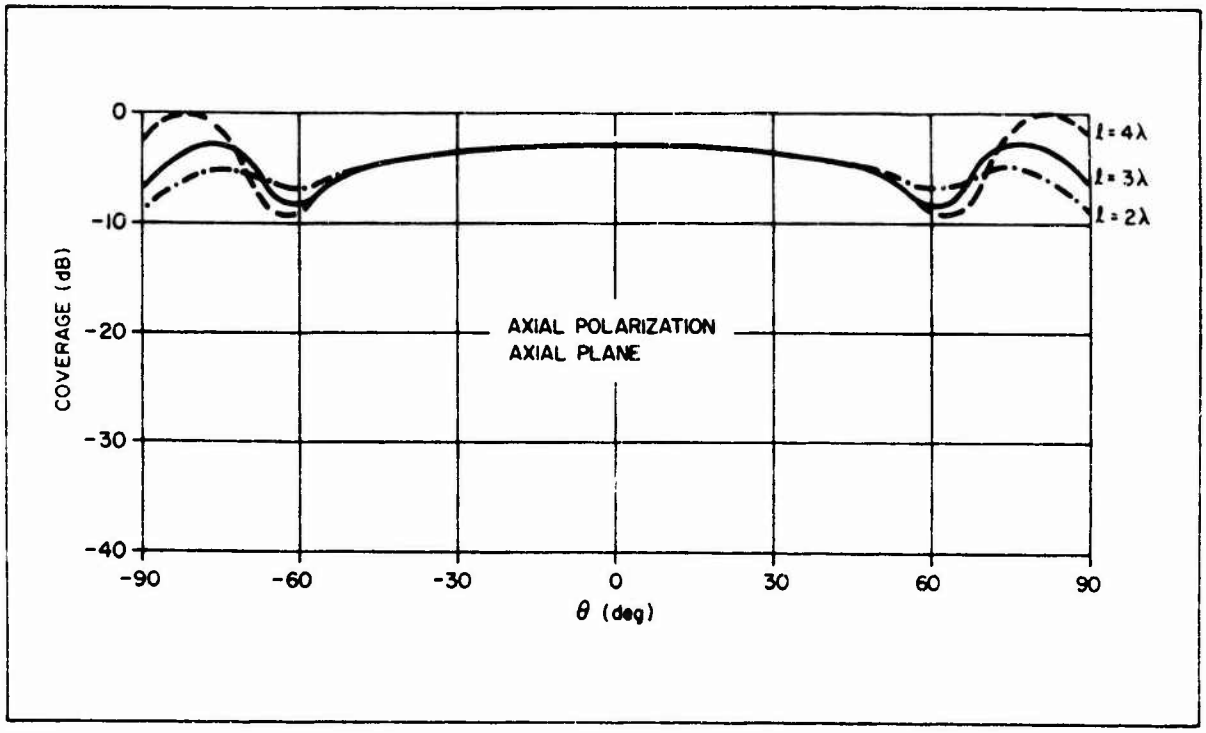

Figure 46 - Array Coverage versus Taper Length

because the gain falloff at endfire exceeds 3 dB. By increasing ℓ to 4λ it is actually possible to achieve near endfire a gain greater than at broadside. This selection of wedge length is not suitable for application because it produces excessive array pattern distortions and excessive back radiation of the type shown in Figures 42 and 43, the region -90 deg $\leq \theta \leq$ -30 deg.

Pattern distortions, due to interference, and back radiation, due to residual excitation of the wedge, constitute the main limitation for the use of dielectric wedges to achieve wide angle coverage. It is not possible to give a general rule. In each case the increase in endfire coverage must be carefully traded off against the antenna pattern distortions.

Finally, the coverage variation versus frequency has been evaluated. Figure 47 plots the axial plane coverage using circular polarization for three frequencies: center (f_o = 10 GHz), high (f_o + 5 percent f_o) and low (f_o - 5 percent f_o). The wedge length is $\ell = 3\lambda_o$. All the three curves have been normalized at their broadside gain value. There are some noticeable if not substantial variations of the array coverage versus frequency. The low

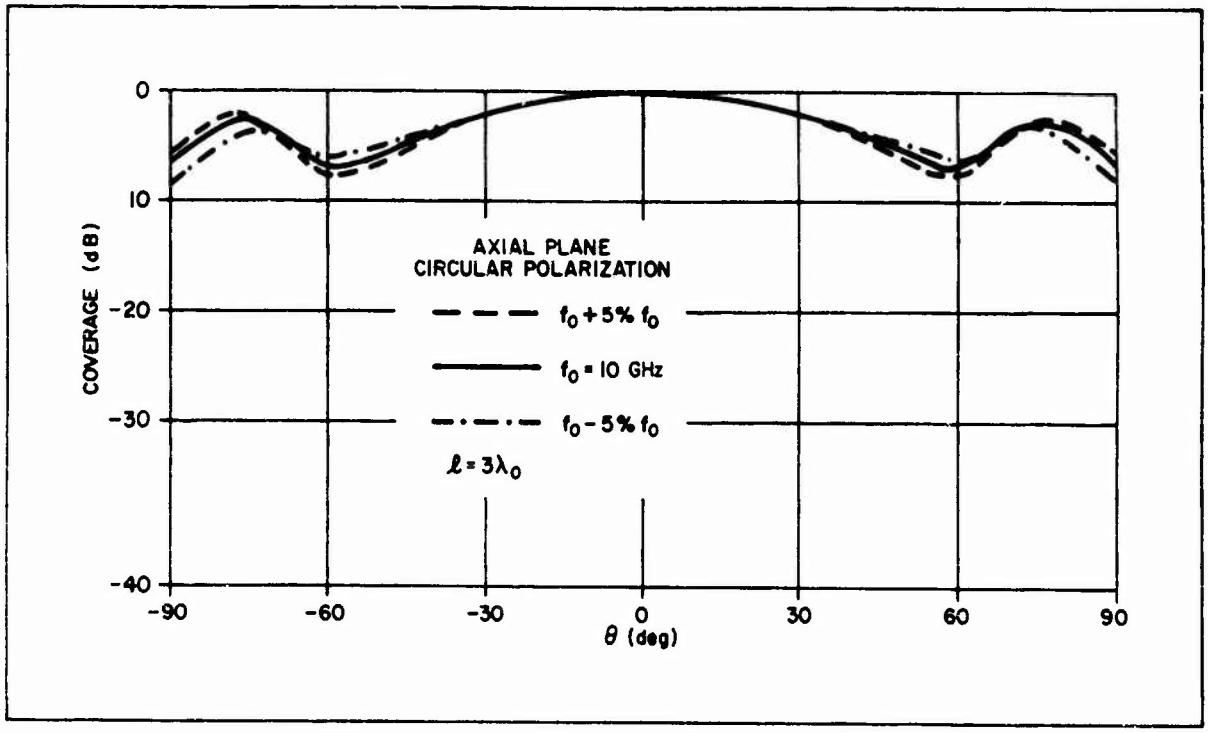

Figure 47 - Array Coverage versus Frequency

frequency curve has a notch at 62 deg from broadside, which is less deep than the one relative to the other two frequencies. The endfire coverage at low frequency is 8 dB below the broadside gain. The high frequency curve shows a notch 7.5 dB deep at ≈ 57 deg from broadside. On the other hand the high frequency endfire gain is about 5.5 dB lower than the broadside value. The circumferential coverage for circular polarization shows analogous behavior versus frequency.

From these results it appears that it is possible to realize hemispheric scan coverage with an 8-dB maximum oscillation over a 10-percent frequency band. A hemispheric coverage with ≈ 6-dB maximum oscillation is realizable only on a narrower band.

5. CONCLUSIONS

In this study program the coverage obtainable by a small array covered by a finite dielectric layer over a cylinder of large radius has been investigated. The goal of the investigation was to achieve hemispheric scan coverage (6 dB maximum antenna gain falloff or oscillation over the hemisphere). The studies have shown that the radiation from a small array over a dielectric-clad cylinder of large radius can be approximated with good accuracy by a planar array model. An accurate method of analysis of finite arrays over an infinite ground plane covered by dielectric was established to evaluate the coverage obtainable from these structures. The advantage of this method over others previously available consists in the fact that no matrix inversion is required to evaluate the electric field distribution at the array element apertures, so relatively large arrays can be analyzed without significant numerical effort.

The analysis has shown that hemispheric scan coverage is not achievable by these structure, because the energy leaving the array in directions close to endfire is trapped in the infinite dielectric sheet and does not contribute to radiation. This trapped energy must be radiated in free space by terminating the dielectric sheet in order to obtain endfire coverage.

An approximate model of the radiation from three-demensional dielectric wedges was generated, so that the coverage of finite arrays covered by finite size dielectric sheets could be analyzed. This approximate model shows that for an array of ≈23 dB aperture gain a substantial endfire coverage can be obtained at the expense of array pattern distortions in directions close to endfire. Computations have shown that hemispheric scan coverage can be obtained with 6.5 dB maximum gain oscillation over the hemisphere. The hemispheric coverage can be achieved over a relatively narrow band. If a 10-percent bandwidth is required, the coverage obtainable from a 23-dB aperture gain array presents maximum oscillations of 8 dB.

The models generated during this study effort are somewhat pessimistic in predicting the coverage of finite arrays covered by a finite dielectric sheet over a

large cylinder because of the approximations introduced in the analysis. The planar array used in modelling the cylindrical arrays predicts slightly lower endfire radiation in the circumferential plane than a rigorous cylindrical model, as shown by the analysis of infinite periodic arrays performed in Section 2. A better than predicted endfire coverage in the circumferential plane can be expected for these structures. Another approximation has been introduced in the analysis of the radiation from wedges by assuming that only the energy relative to a surface wave is incident at the dielectric discontinuity. This is correct only in a first approximation. A more accurate model would show that a spectrum of waves is incident at the dielectric discontinuity, with the effect of enhancing the endfire radiation of the dielectric wedge. Little investigation has been performed in this area and substantial studies are still necessary to accurately predict radiation from three-dimensional dielectric wedges.

With these approximations the analysis performed for a 23-dB aperture gain array predicts that hemispheric scan coverage is possible with a 6.5-dB maximum gain oscillation. This value is close enough to the goal set for this investigation that a 6-dB maximum oscillation can be expected in practice by a 23-dB aperture gain array covered by a dielectric sheet of finite demension over a large cylindrical structure.

APPENDIX A
CONTINUITY OF TANGENTIAL FIELDS AT CYLINDRICAL DIELECTRIC INTERFACES

The continuity of the H_z and E_z components of the field is very simply enforced and yields expressions (13) - (14) for the amplitudes of the transmitted waves.

The enforcement of the continuity of H_ϕ and E_ϕ shows the coupling between LSE and LSM modes and will be discussed in some detail.

Let us call:

$$c_{11}(nw) = \frac{nw}{b}\left(\frac{1}{k_\rho^2} - \frac{1}{k_{\rho\epsilon}^2}\right)$$

$$c_{12}(n, w) = j\left[\frac{H_n'^{(1)}(bk_{\rho\epsilon})}{H_n^{(1)}(bk_{\rho\epsilon})}\ \frac{k_\epsilon}{\eta_\epsilon k_{\rho\epsilon}} - \frac{H_n'^{(2)}(bk_\rho)}{H_n^{(2)}(bk_\rho)}\ \frac{k}{\eta k_\rho}\right]$$

$$c_{21}(n, w) = j\left[\frac{k_\epsilon}{\zeta_\epsilon k_{\rho\epsilon}}\ \frac{H_n'^{(1)}(bk_{\rho\epsilon})}{H_n^{(1)}(bk_{\rho\epsilon})} - \frac{k}{\zeta k}\ \frac{H_n'^{(2)}(bk_\rho)}{H_n^{(2)}(bk_\rho)}\right]$$

$$e_1(n, w) = j\left[\frac{H_n'^{(2)}(bk_\rho)}{H_n^{(2)}(bk_\rho)}\ \frac{k}{\eta k_\rho} - \frac{H_n'^{(2)}(bk_{\rho\epsilon})}{H_n^{(2)}(bk_{\rho\epsilon})}\ \frac{k_\epsilon}{\eta_\epsilon k_{\rho\epsilon}}\right]$$

$$e_2(n, w) \quad j\left[\frac{H_n'^{(2)}(bk_\rho)}{H_n^{(2)}(bk_\rho)}\ \frac{k}{\zeta k_\rho} - \frac{H_n'^{(2)}(bk_{\rho\epsilon})}{H_n^{(2)}(bk_{\rho\epsilon})}\ \frac{k_\epsilon}{\zeta_\epsilon k_{\rho\epsilon}}\right]$$

where

$$k_{\rho\epsilon} = \sqrt{k_\epsilon^2 - w^2} \text{ and } k_\rho = \sqrt{k^2 - w^2}$$

Then by introducing Equations (13) and (14) in Equations (2) to (6) and equating the expressions for E_ϕ and H_ϕ in the dielectric and in free space at r = b, the following equations are obtained:

$$c_{11}(n,w)B(n,w) + c_{12}(n,w)D(n,w) = -\frac{H_n^{(2)}(bk_{\rho\epsilon})}{H_n^{(1)}(bk_{\rho\epsilon})} c_{11}(n,w)A(n,w) + \frac{H_n^{(2)}(bk_{\rho\epsilon})}{H_n^{(1)}(bk_{\rho\epsilon})} e_1(n,w)\,C(n,w) \tag{A-1}$$

$$-c_{21}(n,w)B(n,w) + c_{11}(n,w)D(n,w) = -\frac{H_n^{(2)}(bk_{\rho\epsilon})}{H_n^{(1)}(bk_{\rho\epsilon})} e_2(n,w)A(n,w) - \frac{H_n^{(2)}(bk_{\rho\epsilon})}{H_n^{(1)}(bk_{\rho\epsilon})} c_{11}(n,w)C(n,w) \tag{A-2}$$

It is interesting to note in Equations (A-1 and A-2) that both reflected waves B(n, w) and D(n, w) depend on A(n, w) and C(n, w) simultaneously so that there is cross coupling between LSE and LSM modes.

By calling $\Delta(n,w) = c_{11}^2(n,w) - c_{12}(n,w)\,c_{21}(n,w)$, the following expressions are obtained for the amplitudes of the reflected waves:

$$B(n,w) = \frac{H_n^{(2)}(bk_{\rho\epsilon})}{H_n^{(1)}(bk_{\rho})} \frac{e_2(n,w)\,c_{12}(n,w) - c_{11}^2(n,w)}{\Delta(n,w)} A(n,w) + \frac{H_n^{(2)}(bk_{\rho\epsilon})}{H_n^{(1)}(bk_{\rho\epsilon})} c_{11}(n,w) \frac{e_1(n,w) + c_{12}(n,w)}{\Delta(n,w)} C(n,w) \tag{A-3}$$

$$D(n,w) = -\frac{H_n^{(2)}(bk_{\rho\epsilon})}{H_n^{(1)}(bk_{\rho\epsilon})} c_{11}(n,w) \frac{c_{21}(n,w) + e_2(n,w)}{\Delta(n,w)} A(n,w) + \frac{H_n^{(2)}(bk_{\rho\epsilon})}{H_n^{(1)}(bk_{\rho\epsilon})} \frac{e_1(n,w)\,c_{21}(n,w) - c_{11}^2(n,w)}{\Delta(n,w)} C(n,w) \tag{A-4}$$

The expressions for $\Gamma^{E}(n,w)$, $\Gamma^{H}(n,w)$, $\Gamma^{EH}(n,w)$ and $\Gamma^{HE}(n,w)$ are immediately established by comparing Equations (A-3) and (A-4) with Equations (15) and (16).

From Equations (A-3) and (A-4) it can be seen that the cross coupling coefficients between LSE and LSM modes are due to the curvature of the dielectric interface, since both $\Gamma^{EH}(n,w)$ and $\Gamma^{HE}(n,w)$ depend on $c_{11}(n,w)$, which in turn, is inversely proportional to the radius of curvature of the dielectric interface. As b increases, the value of $\Gamma^{HE}(n,w)$ and $\Gamma^{EH}(n,w)$ decrease as $1/b$. For b sufficiently large ($b \geq 100\lambda$) the contributions of $\Gamma^{EH}(n,w)$ and $\Gamma^{HE}(n,w)$ to the reflected field can be neglected for a large number of cylindrical harmonics.

If the radius of curvature b of the dielectric interface goes to infinity, the cross coupling coefficients $\Gamma^{EH}(n,w)$ and $\Gamma^{HE}(n,w)$ tend to zero, while

$$\lim_{b\to\infty} \Gamma^{E}(n,w) \approx \lim_{b\to\infty} \frac{H_n^{(2)}(bk_{\rho\epsilon})}{H_n^{(1)}(bk_{\rho\epsilon})} \frac{e_2(n,w)}{c_{21}(n,w)} \tag{A-5}$$

$$\lim_{b\to\infty} \Gamma^{H}(n,w) \approx \lim_{b\to\infty} \frac{H_n^{(2)}(bk_{\rho\epsilon})}{H_n^{(1)}(bk_{\rho\epsilon})} \frac{e_1(n,w)}{c_{12}(n,w)} \tag{A-6}$$

It can be simply verified that the limiting values of Equations (A-5) and (A-6) are the well known reflection coefficients for a plane dielectric interface except for a phase term due to the selection of the origin of the cylindrical coordinates.

APPENDIX B

CONTINUITY OF TANGENTIAL ELECTRIC AND MAGNETIC FIELD AT ARRAY APERTURE

To enforce the continuity of the electric field at the array aperture it is convenient to operate on the E_z and E_ϕ components separately.

Enforcing the equality between Equations (17) and (10) for each cylindrical harmonic, the following equation is established for E_z:

$$\frac{1}{2\pi} \sum_{m=0}^{N-1} \sum_{r+-\infty}^{+\infty} e^{-j\frac{2\pi}{N}(i-n)m} e^{-j(i-n)\frac{r}{2}\frac{2\pi}{N}} e^{-jrj(w_o-w)}$$

$$\left\{ \frac{1}{a} \sum_{s=1}^{Q} \left[\delta_{1s} + \Gamma_s(\underline{u}_o) \right] \mathcal{E}_{zs}\left(\frac{n}{a}, w\right) \right\} = A(n, w) \left[H_n^{(2)}(ak_{\rho\epsilon}) \right. \tag{B-1}$$

$$\left. + \Gamma^E(n, w) H_n^{(1)}(ak_{\rho\epsilon}) \right] + \Gamma^{HE}(n, w) C(n, w) H_n^{(1)}(ak_{\rho\epsilon})$$

In Equation (B-1) the summation in m is different from zero if and only if the cylindrical harmonic index is n = i+pN (p is any integer) and in such case the summation is equal to N. By using the expansion of a periodic delta function [11] Equation (B-1) finally becomes [1]:

$$\frac{1}{2\pi} \sum_{p=-\infty}^{+\infty} \frac{2\pi N}{b} \left\{ \frac{1}{a} \sum_{s=1}^{Q} \left[\delta_{is} + \Gamma_s(\underline{u}_o) \right] \mathcal{E}_{zs}\left(\frac{i+pN}{a}, w\right) \right\} \delta(w - w_{opq})$$

$$= A(i + pN, w) \left[H_{i+pN}^{(2)}(ak_{\rho\epsilon}) + \Gamma^E(i + pN, w) H_{i+pN}^{(1)}(ak_{\rho\epsilon}) \right] \tag{B-2}$$

$$+ \Gamma^{HE}(i + pN, w) C(i + pN, w) H_{i+pN}^{(1)}(ak_{\rho\epsilon})$$

where

$w_{opq} = w_o + q\frac{2\pi}{h} + p\frac{\pi}{h}$, and $\delta(w - w_{opq})$ is Dirac's delta function.

By enforcing the equality of E_ϕ in a completely analogous fashion, the following equation is obtained:

$$\frac{1}{2\pi}\sum_{q=-\infty}^{+\infty}\frac{2\pi N}{h}\left\{\frac{1}{a}\sum_{s=1}^{\Omega}\left[\delta_{1s} + \Gamma_s(\underline{u}_o)\right]\left[\mathcal{E}_{\phi s}(\frac{i+pN}{u}, w) + \frac{1}{a}\frac{(i+pN)w}{k_\epsilon^2 - w^2}\mathcal{E}_{zs}(\frac{i+pN}{u}, w)\right]\delta(w - w_{opq}) = j\frac{k_\epsilon}{\eta_\epsilon\sqrt{k_\epsilon^2 - w^2}}\right. \tag{B-3}$$

$$\left\{C(\frac{i+pN}{a}, w)\left[H'^{(2)}_{i+pN}(ak_{\rho\epsilon}) + \Gamma^{H}_{(i+pN, w)}H'^{(1)}_{i+pN}(ak_{\rho\epsilon})\right]\right.$$

$$\left.\left. + \Gamma^{EH}_{(i+pN, w)}A_{(i+pN, w)}H^{(1)}_{i+pN}(ak_{\rho\epsilon})\right\}\right\}$$

The solution of the system of Equations (B-2) and (B-3) yields expressions (18) and (19) of Section 4, with the following definitions of R^E, R^{HE}, R^{EH}, and R^H:

$$R^E(i + pN, w) = \frac{H'^{(2)}_{i+pN}(ak_{\rho\epsilon}) + \Gamma^{H}_{(i+pN, w)}H'^{(1)}_{i+pN}(ak_{\rho\epsilon})}{\Delta^1(i + pN, w)}$$

$$R^{HE}(i+pN, w) = j\frac{\Gamma^{HE}_{(i+bN, w)}H^{(1)}_{i+pN}(ak_{\rho\epsilon})}{\Delta^1(i + pN, w)}\frac{\eta_\epsilon k_{\rho\epsilon}}{k_\epsilon}$$

$$R^H(i + pN, w) = -j\frac{\eta_\epsilon k_{\rho\epsilon}}{k_\epsilon}\frac{H^{(2)}_{i+pN}(ak_{\rho\epsilon}) + \Gamma^{E}_{(i+pN, w)}H^{(1)}_{i+pN}(ak_{\rho\epsilon})}{\Delta^1(i + pN, w)}$$

$$R^{EH}(i+pN, w) = -\frac{\Gamma^{EH}_{(i+pN, w)}H'^{(1)}_{i+pN}(ak_{\rho\epsilon})}{\Delta^1(i + pN, w)}$$

where

$$\Delta^1 (i + pN, w) = \left[H^{(2)}_{i+pN} (ak_{\rho\epsilon}) + \Gamma^{E}_{(i+pN, w)} H^{(1)}_{i+pN} (ak_{\rho\epsilon}) \right]$$

$$\left[H'^{(2)}_{i+pN} (ak_{\rho\epsilon}) + \Gamma^{H}_{(i+pN, w)} H'^{(1)}_{i+pN} (ak_{\rho\epsilon}) \right] +$$

$$-H^{(1)}_{i+pN} (ak_{\rho\epsilon}) \Gamma^{HE}_{(i+pN, w)} H'^{(1)}_{i+pN} (ak_{\rho\epsilon}) \Gamma^{EH}_{i+pN, w)}$$

is the determinant of the coefficients of the system of Equations (B-2) and (B-3).

The expreesion of the external magnetic field can be obtained by introducing Equations (18) and (19) for A(i+pN, w) and C(i+pN, w) in Equations (7), (9), and (12) of Section 2. Some straightforward algebra is involved and Equation (20a) is obtained for the external magnetic field, with the following definitions of $a(\underline{u}_{opq})$, $b(\underline{u}_{opq})$, $c(\underline{u}_{opq})$, and $d(\underline{u}_{opq})$.

$$a(\underline{u}_{opq}) = \left[H^{(2)}_{i+pN} (ak_{pq}) + \Gamma^{H}_{(i+pN, w_{opq})} H^{(1)}_{i+pN} (ak_{pq}) \right] R^{H} (i+pN, w_{opq}) \qquad \text{(B-4)}$$

$$+ \Gamma^{EH}_{(i+pN, w_{opq})} H^{(1)}_{i+pN} (ak_{pq}) R^{HE} (i+pN, w_{opq})$$

$$b(\underline{u}_{opq}) = \left[H^{(2)}_{i+pN} (ak_{pq}) + \Gamma^{H}_{(i+pN, w_{opq})} H^{(1)}_{(ak_{pq})} \right]$$

$$\left[\frac{1}{a} \frac{(i+pN)w_{opq}}{k^2_{\epsilon} - w^2_{poq}} R^{H} (i+pN, w_{opq}) + R^{EH} (i+pN, w_{opq}) \right] \qquad \text{(B-5)}$$

$$+ \Gamma^{EH} (i+pN, w_{opq}) H^{(1)}_{i+pN} (ak_{pq}) \left[R^{E} (i+pN, w_{opq}) \right.$$

$$\left. + \frac{1}{a} \frac{(i+pN)w_{opq}}{k^2_{\epsilon} - w^2_{opq}} R^{HE} (i+pN, w_{opq}) \right]$$

$$c(\underline{u}_{opq}) = j \left\{ \frac{k_\epsilon}{\zeta_\epsilon} \frac{1}{\sqrt{k_\epsilon^2 - w_{opq}^2}} R^{HE}(i + pN, w_{opq}) \right.$$

$$\left[H'^{(2)}_{i+pN}(ak_{pq}) + \Gamma^{E}(i + pN, w_{opq}) H'^{(1)}_{i+pN}(ak_{pq}) \right]$$

$$+ \Gamma^{HE}(i + pN, w_{opq}) H'^{(1)}_{i+pN}(ak_{pq}) R^{H}(i + pN, w_{opq})$$

$$+ R^{HE}(i + pN, w_{opq}) \Gamma^{EH}(i + pN, w_{opq}) H'^{(1)}_{i+pN}(ak_{pq})$$

$$+ \frac{1}{a} \frac{(i + pN)w_{opq}}{k_\epsilon^2 - w_{opq}^2} R^{M}(i + pN, w_{opq}) \left[H^{(2)}_{i+pN}(ak_{pq}) \right.$$

$$\left. \left. + \Gamma^{H}(i+pN, w_{opq}) H^{(1)}_{i+pN}(ak_{pq}) \right] \right\} \qquad \text{(B-6)}$$

$$d(\underline{u}_{opq}) = j \left\{ \frac{k_\epsilon}{\zeta_\epsilon} \frac{1}{\sqrt{k^2 - w_{opq}^2}} \left[R^{E}(i + pN, w_{opq}) \right. \right.$$

$$\left. + \frac{1}{a} \frac{(i + pN)w_{opq}}{k_\epsilon^2 - w_{opq}^2} R^{HE}(i + pN, w_{opq}) \right] \left[H'^{(2)}_{i+pN}(ak_{pq}) \right.$$

$$\left. + \Gamma^{E}(i + pN, k_{opq}) H'^{(1)}_{i+pN}(ak_{pq}) \right] + \left[R^{HE}(i + pN, w_{opq}) \right.$$

$$\left. + \frac{1}{a} \frac{(i + pN)w_{opq}}{k_\epsilon^2 - w_{opq}^2} R^{H}(i + pN, w_{opq}) \right] \Gamma^{HE}(i + pN, w_{opq}) H'^{(1)}_{i+pN}(ak_{pq})$$

$$+ \left[R^{E}(i+pN, w_{opq}) + \frac{1}{a} \frac{(i+pN)w_{opq}}{k_\epsilon^2 - w_{opq}^2} R^{HE}(i+pN, w_{opq}) \right]$$

$$\Gamma^{EH}(i + pN,\ w_{opq})\, H^{(1)}_{i+pN}(ak_{pq}) + \frac{1}{a}\,\frac{(i + pN)w_{pq}}{k_\epsilon^2 - w_{opq}^2}$$

$$\left[\frac{1}{a}\,\frac{(i+pN)w_{opq}}{k_\epsilon^2 - w_{opq}^2}\, R^{H}(i + pN,\ w_{opq}) + R^{EH}(i + pN,\ w_{opq})\right]$$

$$\left[H^{(2)}_{i+pN}(ak_{pq}) + \Gamma^{H}(i + pN,\ w_{opq})\, H^{(1)}_{i+pN}(ak_{pq})\right]\Bigg\} \qquad \text{(B-7)}$$

In Equations (B-4) - (B-7), $k_{pq} = \sqrt{k_\epsilon^2 - w_{opq}^2}$. It is worth noticing that for $(b-a) \longrightarrow 0$ or for $\epsilon \longrightarrow \epsilon_o$ the expressions (B-4) - (B-7) tend to the equations given in a previous report [1] for the tangential magnetic field on an infinite cylindrical array with no dielectric cover.

The continuity of the tangential magnetic field at the array element aperture can be enforced by applying Galerkin's method, whereby the difference between $\underline{H}_t^-(\underline{s})$ and $H_t^+(s)$ is forced to have zero projection on the modal functions $\hat{\rho}_o \times \underline{e}_k(s)$. By scalar multiplication of the difference between Equations (20) and (20a) and the magnetic field modal functions $\hat{\rho}_o \times \underline{e}_k(s)$, the following Q equations are obtained [1]:

$$Y_k\left[\delta_{1k} - \Gamma_k(\underline{u}_o)\right] = \sum_{q=-\infty}^{\infty}\sum_{p=-\infty}^{\infty}\Big\{a(\underline{u}_{opq})\,\bar{\mathcal{E}}_\phi(\underline{u}_{opq})\,\mathcal{E}^*_{k\phi}(\underline{u}_{opq}) +$$

$$b(\underline{u}_{opq})\,\bar{\mathcal{E}}_z(\underline{u}_{opq})\,\mathcal{E}^*_{k\phi}(\underline{u}_{opq}) + c(\underline{u}_{opq})\,\bar{\mathcal{E}}_\phi(\underline{u}_{opq})\,\mathcal{E}^*_{kz}(\underline{u}_{opq}) + \qquad \text{(B-8)}$$

$$d(\underline{u}_{opq})\,\bar{\mathcal{E}}_z(\underline{u}_{opq})\,\mathcal{E}^*_{kz}(\underline{u}_{opq})\Big\} \qquad (k = 1, \ldots, Q)$$

Where the star denotes complex conjugate. The system of Equation (B-8) can be cast in the form of Equation (21) by calling

$$L_{ks}(\underline{u}_o) = \frac{4\pi^2}{C} \sum_{q=-\infty}^{+\infty} \sum_{p=-\infty}^{+\infty} \Big\{ a(\underline{u}_{opq})\, \mathcal{E}^{*}_{k\phi}(\underline{u}_{opq})\, \mathcal{E}_{s\phi}(\underline{u}_{opq}) +$$

$$b(\underline{u}_{opq})\, \mathcal{E}^{*}_{k\phi}(\underline{u}_{opq})\, \mathcal{E}_{sz}(\underline{u}_{opq}) + c(\underline{u}_{opq})\, \mathcal{E}^{*}_{kz}(\underline{u}_{opq})\, \mathcal{E}_{s\phi}(\underline{u}_{opq}) +$$

$$d(\underline{u}_{opq})\, \mathcal{E}^{*}_{kz}(\underline{u}_{opq})\, \mathcal{E}_{sz}(\underline{u}_{opq}) \Big\}$$

where C is the elementary array cell area.

APPENDIX C
CONTINUITY OF TANGENTIAL FIELDS AT FINITE ARRAY APERTURE

By requiring that the difference between Equations (36) and (37) has zero projection on the subspace spanned by $\hat{z} \times \underline{e}^k_h (\underline{s} - \underline{s}_n)$ the following equation is obtained:

$$(\delta^k_{l,h} - \Gamma^k_h)\, Y^k_h = \frac{1}{2\pi} \iint_{A_k} \hat{z} \times \underline{e}^k_h (\underline{s} - \underline{s}_k) \cdot$$

$$\left\{ \iint_{-\infty}^{+\infty} \left[\hat{\rho} \mathcal{E}_\psi (\underline{u}) \frac{w_d}{k_d \eta_d} F^{TE}(|\underline{u}|) \right. \right. \qquad \text{(C-1)}$$

$$\left. \left. + \hat{\psi}\, \mathcal{E}_\rho (\underline{u})\, \frac{k_d}{w_d \eta_d}\, F^{TM}(|\underline{u}|) \right] e^{-j \underline{u} \underline{s}}\, d\underline{u} \right\} d A_k$$

where the first integration is extended over the kth aperture. By changing order of integration and performing the integration on A_k, Equation (C-1) becomes:

$$(\delta^k_{l,n} - \Gamma^k_h)\, Y^k_h = \iint_{-\infty}^{+\infty} \left[\mathcal{E}_\rho(\underline{u})\, \mathcal{E}^{k*}_{\rho m}(\underline{u}) \frac{k_d}{\eta_d w_d} F^{TM}(|\underline{u}|) \right. \qquad \text{(C-2)}$$

$$\left. - \mathcal{E}_\psi(\underline{u})\, \mathcal{E}^{k*}_{\psi h}(\underline{u}) \frac{w_d}{\eta_d k_d} F^{TE}(|\underline{u}|) \right] e^{-j \underline{u} \underline{s}_k}\, d\underline{u}$$

where $\mathcal{E}^k_{\rho h}{}^*$ and $\mathcal{E}^k_{\psi h}{}^*$ are the components of $\underline{\mathcal{E}}^k_h (-\underline{u})$.

Inserting in Equation (C-2) expression (35a) and (35b) for $\mathcal{E}_\rho(\underline{u})$ and $\mathcal{E}_\psi(u)$ we finally obtain:

$$(\delta^{k}_{l,h} - \Gamma^{k}_{h})\, Y^{k}_{h} = \sum_{n=1}^{N} \sum_{m=1}^{M} (\delta^{n}_{l,m} + \Gamma^{n}_{m}) \cdot$$

$$\iint_{-\infty}^{+\infty} \left[\mathcal{E}^{n}_{\rho m}(\underline{u})\, \mathcal{E}^{k^*}_{\rho h}(\underline{u}) \frac{k_d}{w_a \eta_d} F^{TM}(|\underline{u}|) \right. \qquad \text{(C-3)}$$

$$\left. - \mathcal{E}^{n}_{\psi m}(\underline{u})\, \mathcal{E}^{k^*}_{\psi h}(\underline{u}) \frac{w_d}{k_d \eta_d} F^{TE}(|\underline{u}|) \right] e^{-j\underline{u}(\underline{s}_k - \underline{s}_h)}\, d\underline{u}$$

Equation (C-3) can be written as Equation (40) by defining the mutual admittance term Y^{nk}_{mh} as:

$$Y^{nk}_{mh} = \frac{1}{\eta_d} \iint_{-\infty}^{+\infty} \left[\mathcal{E}^{n}_{\rho m}(\underline{u})\, \mathcal{E}^{k^*}_{\rho h}(\underline{u}) \frac{k_d}{w_d} F^{TM}(|\underline{u}|) \right.$$

$$\left. - \mathcal{E}^{n}_{\psi m}(\underline{u})\, \mathcal{E}^{k^*}_{\psi h}(\underline{u}) \frac{w_d}{k_d} F^{TE}(|\underline{u}|) \right] e^{-j\underline{u}(\underline{s}_k - \underline{s}_h)}\, d\underline{u}$$

From Equation (C-3) it is easy to derive the admittance expressions for an infinite periodic array of waveguide apertures. Writing (C-2) for an arbitrarily chosen reference element, we can express the vector $\underline{s}_k - \underline{s}_n$ in terms of the lattice basis vectors $\underline{s}_1$, $\underline{s}_2$ and the tangential electric field at the array aperture can be given in terms of the electric field at the reference element [23]:

$$\sum_n (\delta^n{}_{1,m} + \Gamma^n{}_m)\ \underline{\mathcal{E}}^n{}_m\ (\underline{u})\ e^{-j\underline{u}(\underline{s}_k - \underline{s}_n)} \longrightarrow \sum_{p=-\infty}^{+\infty} \sum_{q=-\infty}^{+\infty} (\delta_{1,m} + \Gamma_m)$$

$$\mathcal{E}_m\ (\underline{u})\ e^{-j\ (\underline{u} + \underline{u}_o)\ (p\ \underline{s}_1 + q\ \underline{s}_2)} \qquad \text{(C-4)}$$

Inserting Equation (C-4) in (C-3), we note that [11]:

$$\sum_{p=-\infty}^{+\infty} \sum_{q=-\infty}^{+\infty} e^{-j\ (\underline{u} + \underline{u}_o)\ (p\underline{s}_1 + q\underline{s}_2)} = \frac{4\pi^2}{C} \sum_{p=-\infty}^{+\infty} \sum_{q=-\infty}^{+\infty}$$

$$\delta(u + \underline{u}_o + p\ \underline{t}_1 + q\ \underline{t}_2)$$

where δ is Dirac's delta function, C is the lattice cell area and $\underline{t}_1$, $\underline{t}_2$ are the reciprocal vectors of $\underline{s}_1$, $\underline{s}_2$. By performing the integration, Equation (C-3) becomes:

$$(\delta_{1,n} - \Gamma_h)\ Y_h = \sum_{m=1}^{M} (\delta_{1,m} + \Gamma_m) \sum_{p=-\infty}^{+\infty} \sum_{q=-\infty}^{+\infty} \frac{4\pi^2}{c\eta_d} \cdot$$

$$\left\{ \mathcal{E}_{\rho m}\ (\underline{u})\ \mathcal{E}^*{}_{\rho h}\ (\underline{u})\ \frac{k_d}{w_d}\ F^{TM}\ (|\underline{u}|) + \right. \qquad \text{(C-5)}$$

$$\left. - \mathcal{E}_{\psi m}\ (\underline{u})\ \mathcal{E}^*{}_{\psi h}\ (\underline{u})\ \frac{w_d}{k_d}\ F^{TE}\ (|\underline{u}|) \right\}$$

$$u = u_o + p\underline{t}_1 + q\underline{t}_2$$

where the brackets indicate that the function is computed at the points $\underline{u} = \underline{u}_o + p\underline{t}_1 + q\underline{t}_2$. Equation (C-5) is immediately recognized to be the solution of the boundary condition problem for an infinite periodic array of waveguide apertures, as presented by several authors [7-12] .

APPENDIX D
ASYMPTOTIC EVALUATION OF FAR FIELD

The asymptotic evaluation of Equation (48) is treated here with some detail for the TE_{11} polarized in the y direction of Figure 48. For this mode we have (Reference 1):

$$\mathcal{E}_{\rho}\ (t, \mu) = A \frac{\sin \mu}{t} J_1 (at) \qquad \text{(D-1)}$$

$$\mathcal{E}_{\psi}\ (t, \mu) = A \frac{a \cos \mu}{1 - (\frac{at}{x'_{11}})^2} J'_1 (at) \qquad \text{(D-2)}$$

In Equations (D-1) and (D-2) "a" is the element radius, J_1 is the Bessel function of first kind and first order, J'_1 is its derivative, x'_{11} is the first root of the Equation $J'_1 (x) = O$. The amplitude constant A,

$$A = \frac{\sqrt{\frac{2}{\pi}}}{\sqrt{x_{11}^2 - 1}}$$

is obtained by normalizing the mode funtions. Inserting Equations (D-1) and (D-2) in Equation (48) and separating the TM and TE components we get:

$$E_{\rho}\ (r, \theta, \phi) = \frac{A}{2\pi} \int_0^{2\pi} \int_0^{\infty} \frac{\sin \mu}{t} J_1 (at)\ P^{TM}(t)\ e^{\exp}\ t\ dt\ d\mu \qquad \text{(D-3)}$$

where

$$\exp = -j \left[r \cos \theta \sqrt{k^2 - t^2} + tr \sin \theta \cos (\phi - \mu) \right]$$

$$E_\psi (r, \theta, \phi) = \frac{A}{2\pi} \int_0^{2\pi} \int_0^{\frac{a \cos \mu}{1-(\frac{at}{1})^2}} J_1'(at)\, P^{TE}(t)\, e^{\exp}\, t\, dt\, d\mu \qquad \text{(D-4)}$$

where

$$\exp = -j \left[r \cos \theta \sqrt{k^2 - t^2} + tr \sin \theta \cos (\phi - \mu) \right]$$

Let us deal first with the integral in Equation (D-3). By performing the integration in μ, Equation (D-3) becomes:

$$E_\rho (r, \theta, \phi) = -j A \sin \phi \int_0^\infty \frac{J_1(at)}{t} P^{TM}(t) \frac{1}{2} \left[H_1^{(2)}(tr \sin \theta) + H_1^{(1)}(tr \sin \theta) \right] e^{-j r \cos \theta \sqrt{k^2 - t^2}}\, t\, dt \qquad \text{(D-5)}$$

For large values of r we can write:

$$E_\rho (r, \theta, \phi) = -j A \sin \phi \int_0^\infty \frac{J_1(at)}{t} P^{TM}(t) \frac{j}{2} \sqrt{\frac{-2j}{\pi t r \sin \theta}}\, e^{-j (r t \sin \theta + r \cos \theta \sqrt{k^2 - t^2})}\, t\, dt +$$

$$-j A \sin \phi \int_0^\infty \times \frac{J_1(at)}{t} P^{TM}(t) \frac{(-j)}{2} \sqrt{\frac{-2j}{\pi t r \sin \theta}}\, e^{j (r t \sin \theta - r \cos \theta \sqrt{k^2 - t^2})}\, t\, dt \qquad \text{(D-6)}$$

By the changing the variable $t \rightarrow - t$ in the second integral of Equation (D-6) and summing the two integrals we finally obtain

$$\lim_{r \to \infty} E_\rho (r, \theta, \phi) = \frac{A}{2} \sin \phi \int_{-\infty}^{+\infty} \frac{J_1 (at)}{t} P^{TM} (t) \sqrt{\frac{2j}{\pi t r \sin \theta}} e^{\exp} t \, dt \qquad \text{(D-7)}$$

where

$$\exp = -j (t r \sin \theta + r \cos \theta \sqrt{k^2 - t^2})$$

With an identical procedure the integral in Equation (D-4) is reduced to

$$\lim_{r \to \infty} E_\psi (r, \theta, \phi) = \frac{A}{2} \cos \phi \int_{-\infty}^{+\infty} \frac{a J_1' (at)}{1 - (\frac{at}{1})^2} P^{TE} (t) \sqrt{\frac{2j}{\pi t r \sin \theta}} e^{\exp} t \, dt \qquad \text{(D-8)}$$

where

$$\exp = -j (t r \sin \theta + r \cos \theta \sqrt{k^2 - t^2})$$

The asymptotic evaluation of the integrals in Equations (D-7) and (D-8) does not present any difficulty as well-known methods are available (References 25 and 26) and the results given by Equations (48 a-b) and (49) are promptly established.

REFERENCES

1) Borgiotti, G.V., and Balzano, Q., "Analysis and Element Pattern Design of Periodic Arrays of Circular Apertures on Conducting Cylinders", Air Force Cambridge Research Lab., AFCRL-70-0682, Contract F19628-70-C-0226, Sci. Rep No. 1, Nov. 1970.

2) Wait, J.R., and Mientka, W.E., "Slotted Cylinder Antennas with a Dielectric Coating", Journal of Res. Nat. Bur. Stand., Vol. 58, June 1957, pp. 287-296.

3) Wait, J.R., and Conda, A.M., "Radiation from Dielectric Clad and Corrugated Cylinders", J. Res. Nat. Bur. Stand., Vol. 59, November 1957, pp. 307-316.

4) Sureau, J.C., and Hessel, A., "Resonances in Circular Arrays with Dielectric Sheet Covers", 1970, IEEE Transaction on Antennas and Propulsion, Vol. AP-21, No. 2, March 1973, pp. 159-164.

5) Sureau, J.C., Hessel, A., "Realized Gain Function for a Cylindrical Array of Open-Ended Waveguides", Phased Array Antennas, Artech House, April 1972, pp. 315-322.

6) Altshuler, H.M., and Goldstone, L.O., "On Network Representations of Certain Obstacles in Waveguide Regions", IEEE Trans. Micr. Theory and Tech., Vol. MTT-7, April 1959, pp. 213-221.

7) Borgiotti, G.V., "Modal Analysis of Periodic Planar Phased Arrays of Apertures", IEEE Proc. Vol. 56, November 1968, pp. 1881-1892.

8) Wait, J.R., "Scattering of a Plane Wave from a Circular Dielectric Cylinder at Oblique Incidence", Can. J. Phys., Vol. 33, Feb. 1955, pp. 189-195.

9) Adey, A.W., "Scattering of Electromagnetic Waves by Coaxial Cylinders", Can. J. Phys., Vol. 34, 1956, pp. 510-520.

10) Borgiotti, G.V., and Balzano, Q., "Mutal Coupling Analysis of a Conformal Array of Elements on a Cylindrical Surface", IEEE Trans. on Ant. and Prop. AP-18, January 1970, pp. 55-64.

11) Peterson, D.P., and Middleton, D., "Sampling and Reconstruction of Wave-Number Limited Functions in N-Dimensional Euclidean Space", Information and Control 5, 1962, pp. 279-323.

REFERENCES (Cont.)

12) Amitay, N., and Galindo, V., "The Analysis of Circular Waveguide Phased Arrays", Bell Syst. Tech. J. Vol. 47, November 1968, pp. 1903-1932.

13) Marcuvitz, N., "Waveguide Handbook", Section 1.7, Dover Publications, New York.

14) Lee, S.W., et. al., "Convergence of Numerical Solutions of Iris Type Discontinuity Problems", Hughes Aircraft Co., FR 70-14-594, August, 1970.

15) Balzano, Q., "Investigation of the Element Pattern in Cylindrical Phased Arrays of Circular Waveguides", Air Force Cambridge Research Lab., AFCRL-72-0232, Contract F19628-70-C-0226, Sci., Rep. No. 3, March 1972.

16) Borgiotti, G.V., and Balzano, Q., "Conformal Arrays on Surfaces with Rotational Symmetry", Phased Array Antennas, Oliver, A., and Knittel, G., Editors, Artech House, Inc., 1972, pp. 301-314.

17) Borgiotti, G.V., "Edge Effects in Finite Arrays of Uniform Slits on a Ground Plane", IEEE Trans. on Ant. and Prop., Vol. AP-19, No. 5, Sept. 1971, pp. 593-599.

18) Wu, C.P., "Analysis of Finite Parallel-Plate Waveguide Arrays", IEEE Trans. on Ant. and Prop., Vol. AP-18, No. 3, May 1970, pp. 328-334.

19) Bailey, M.C., "Mutual Coupling in a Finite Size Phased Array of Circular Waveguide Elements", 1972 G-AP International Symposium Digest, pp. 161-164.

20) Steyskal, H., "Mutual Coupling in a Finite Planar Array Antenna", Ibidem, pp. 165-168.

21) Knittel et. al., "Element Pattern Nulls in Phased Arrays and Their Relation to Guided Waves", Proc. IEEE, Vol. 56, No. 11, November 1968, pp. 1822-1836.

22) Montgomery, C.G., Dicke, R.H., Purcell, E.M., "Principles of Microwave Circuits", McGraw Hill, New York, 1948, Sect. 5-16.

23) Borgiotti, G.V., "A Novel Expres ion for the Mutual Admittance of Planar Radiating Elements", IEEE Trans. on Ant. and Prop. Vol. AP-16, May 1968, pp. 329-333.

24) Wu, C.P., "Integral Equation Solutions for the Radiation from a Waveguide Through a Dielectric Slab", IEEE Trans. on Ant. and Prop. Vol. AP-17, No. 6, November 1969, pp. 733-739.

REFERENCES (Cont.)

25) Felsen, L.B., and Marcuvitz, N., "Radiation and Scattering of Waves", Prentice-Hall, Englewood Cliffs, N.J., 1973, Sect. 4, pp. 370-441.

26) Bernard, G.D., and Ishimaru, A., "Pole Contributions to Electromagnetic Fields in the Light of a Modified Saddle Point Technique", AFCRL-63-565, Technical Rept. No. 82, October 1963.

27) Oliner, A.A., and Malech, R.G., "Pattern of an Element in a Passively Terminated Array Environment", Microwave Scanning Antennas, Vol. 3, Hansen, R.C., Editor, Academic Press, N.Y., 1966, pp. 301-308.

28) Collin, R.E., "Foundations of Microwave Engineering", McGraw-Hill, N.Y., pp. 237-238.

29) Balling, P., and Andersen, J.B., "Radiation from a Dielectric Wedge", Report D110, Lab. of Electromagnetic Theory, Technical University of Denmark, Lyngby, October 1970.

30) Balling, P., "Near Field Measurements and Calculations on the Dielectric Wedge", Report D114, Lab of Electromagnetic Theory, Technical University of Denmark, Lyngby, December 1970.

31) Lewis, L.R., "Performance of a Protruding - Dielectric Waveguide Element in a Phased Array", IEEE Trans. on Art. and Prop., Vol AP-20, Number 6, November 1972, pp. 712-722.